Supporting Information for

Tailoring Bond Topologies in Open-Shell Graphene Nanostructures

Shantanu Mishra,[†,¶] Thorsten G. Lohr,[‡,¶] Carlo A. Pignedoli,[†] Junzhi Liu,[‡] Reinhard Berger,[‡] José I. Urgel,[†] Klaus Müllen,[§] Xinliang Feng,[‡,*] Pascal Ruffieux,[†] and Roman Fasel[†,Δ,*]

[†]Empa, Swiss Federal Laboratories for Materials Science and Technology, Überlandstrasse 129, 8600 Dübendorf, Switzerland

[‡]Center for Advancing Electronics and Department of Chemistry and Food Chemistry, Technical University of Dresden, 01062 Dresden, Germany

[§]Max Planck Institute for Polymer Research, Ackermannweg 10, 55128 Mainz, Germany

[Δ]Department of Chemistry and Biochemistry, University of Bern, Freiestrasse 3, 3012 Bern, Switzerland

[¶]S.M. and T.G.L. contributed equally to this work

Table of Contents

1. Room temperature phase of 3

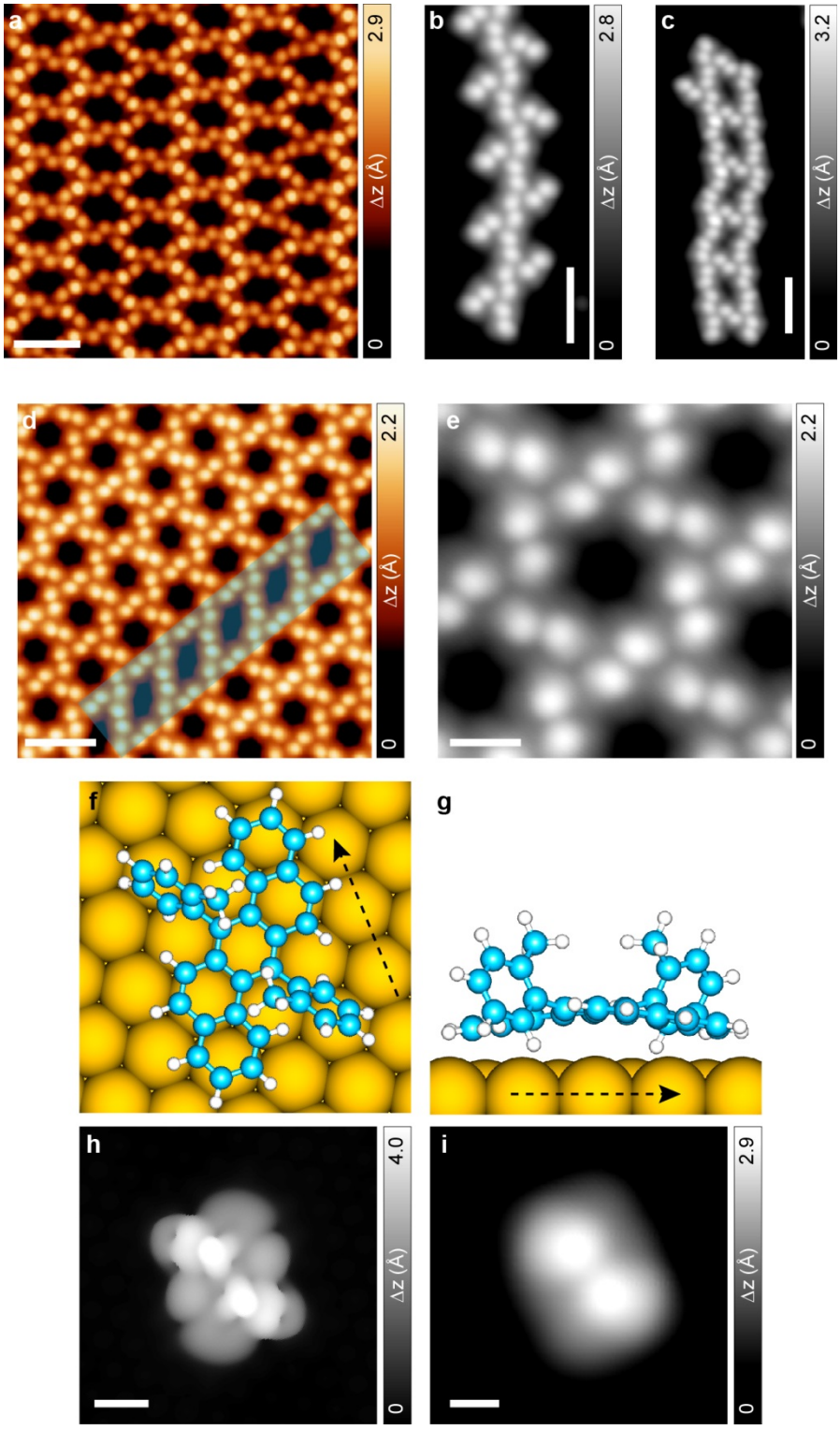

Figure S1 | Room temperature phase of 3 on Au(111). (a) High-resolution STM image of a self-assembled island (V = -200 mV, I = 100 pA). **(b)** High-resolution STM image of a self-assembled chain flanked by individual molecules on both sides (V = -1.5 V, I = 100 pA). **(c)** High-resolution STM image of a self-assembled ladder-type structure (V = -2.0 V, I = 100 pA). **(d)** Sample with a higher coverage than in (a) showing formation of a self-assembled

Kagomé lattice. The shaded part corresponds to a defect line separating two Kagomé domains (V = -100 mV, I = 100 pA). **(e)** Small-scale high-resolution STM image of the Kagomé domain (V = 50 mV, I = 70 pA). **(f), (g)** Top and side views of the DFT-optimized equilibrium geometry of **3** on Au(111). The dashed arrows along the long axis of the molecule help interpret the side view. **(h)** DFT-simulated STM image of **3** on Au(111) (V = -500 mV). **(i)** Experimental high-resolution STM image of **3** showing excellent agreement with the simulated STM image, evidencing the structural integrity of **3** on the surface (V = -1.0 V, I = 70 pA). Scale bars: (a)-(d) – 3 nm; (e) – 1 nm; (h), (i) – 0.5 nm.

2. Height-dependent UHR-STM images of 1

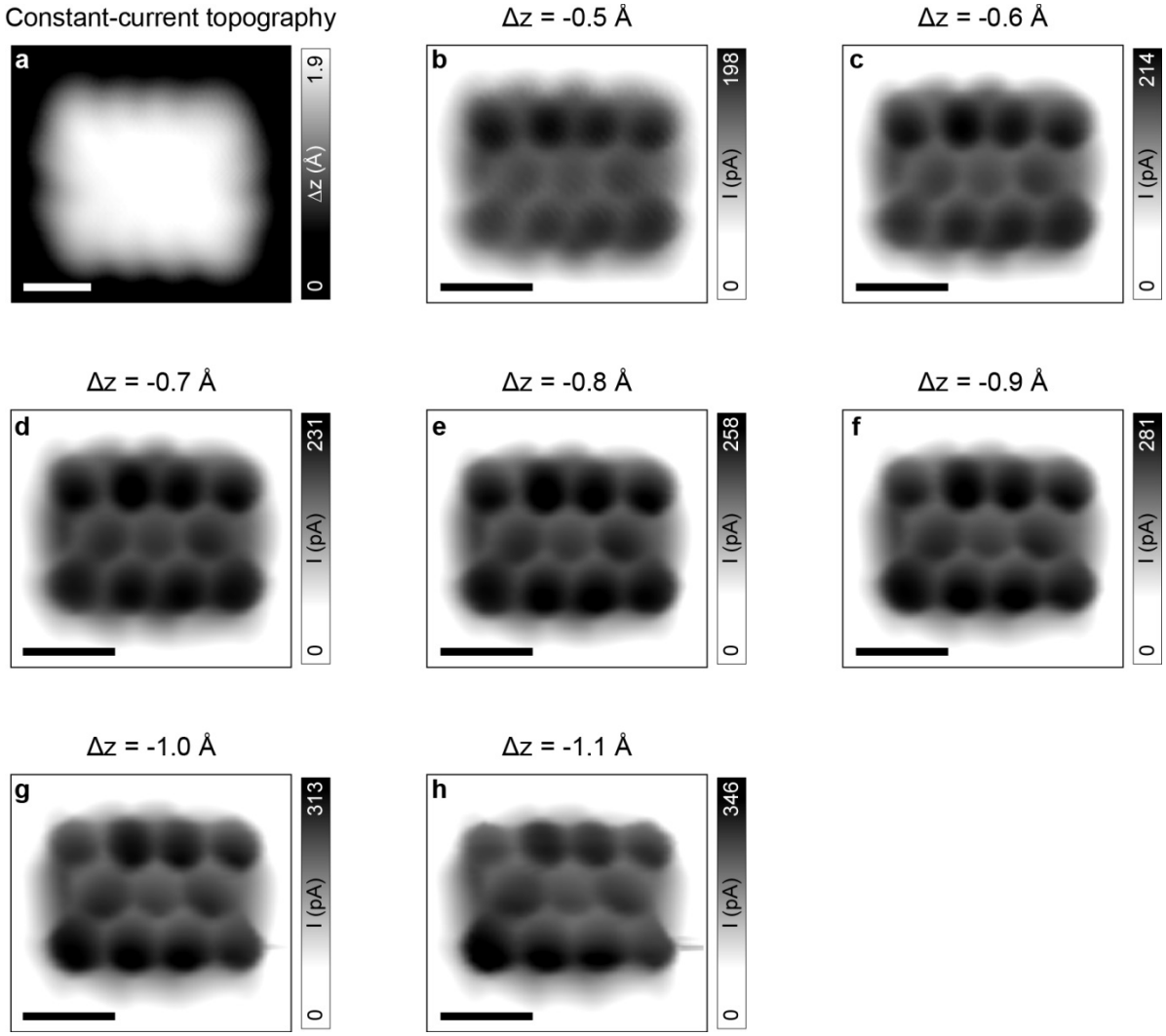

Figure S2 | UHR-STM imaging of 1 at different tip-molecule distances. (a) High-resolution STM image of **1** acquired with a CO-functionalized tip (V = -160 mV, I = 70 pA). **(b)-(h)** Corresponding UHR-STM images acquired at different tip-molecule distances. For each image, the lowering of the tip height Δz, after the feedback loop was opened, is indicated at the top. Open feedback parameters: (b) V = 5 mV, I = 50 pA; (c)-(h) V = -5 mV, I =50 pA. All scale bars: 0.5 nm.

3. Scanning tunneling spectroscopy on 1 and 2 with a metallic tip

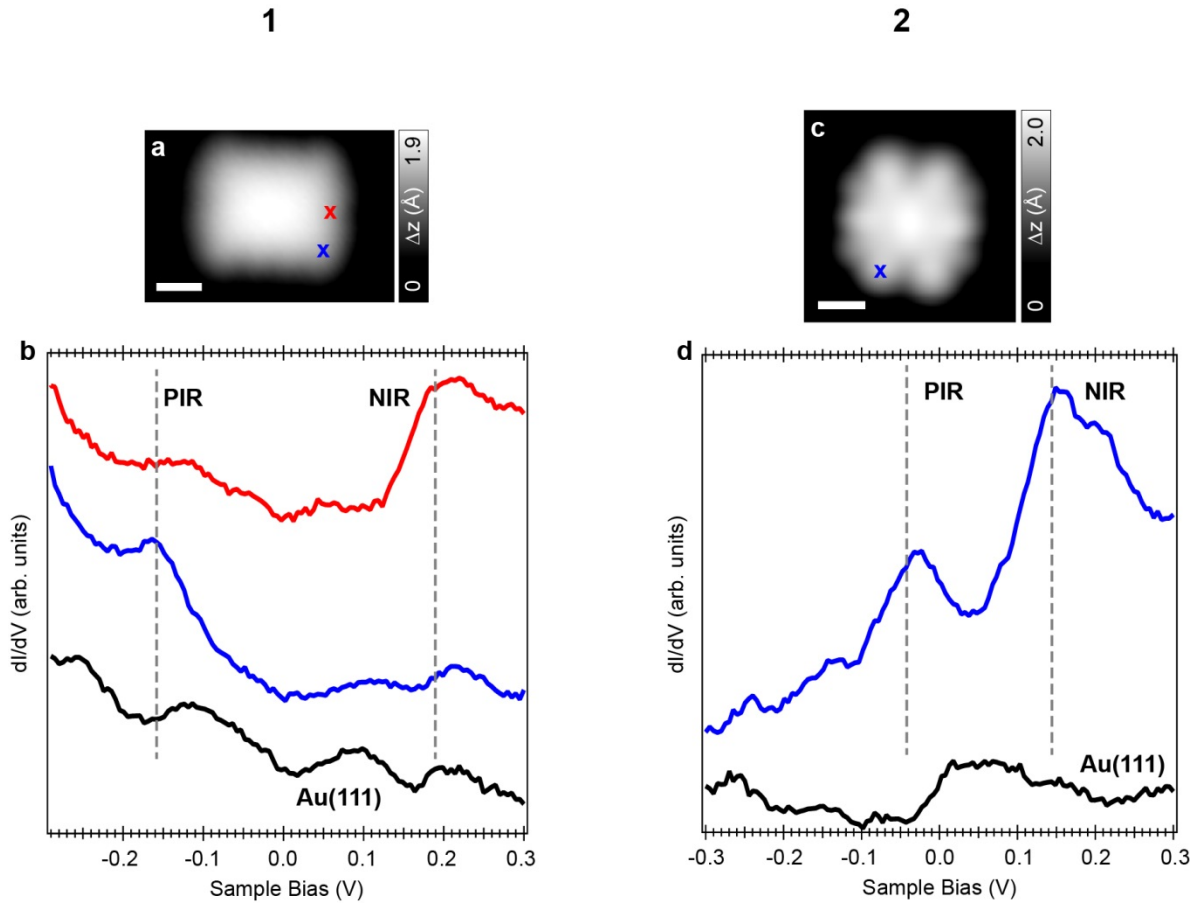

Figure S3 | d*I*/d*V* spectroscopy on 1 and 2 with a Au-terminated tip. (a), (c) High-resolution STM images of **1** ((a), V = -300 mV, I = 50 pA) and **2** ((c), V = 5 mV, I = 100 pA). **(b), (d)** dI/dV spectra on **1** (b) and **2** (d), revealing clear resolution of the PIR and the NIR at energies as those obtained with a CO-functionalized tip (dashed gray lines). The positions at which the spectra on the molecules were acquired are highlighted by blue and red crosses in (a) and (c). Open feedback parameters for the dI/dV spectra: (c) V = -300 mV, I = 150 pA; V_{rms} = 20 mV; (d) V = -300 mV, I = 250 pA; V_{rms} = 14 mV. All scale bars: 0.5 nm.

4. Comparison of constant-height and constant-current d*I*/d*V* maps of 1

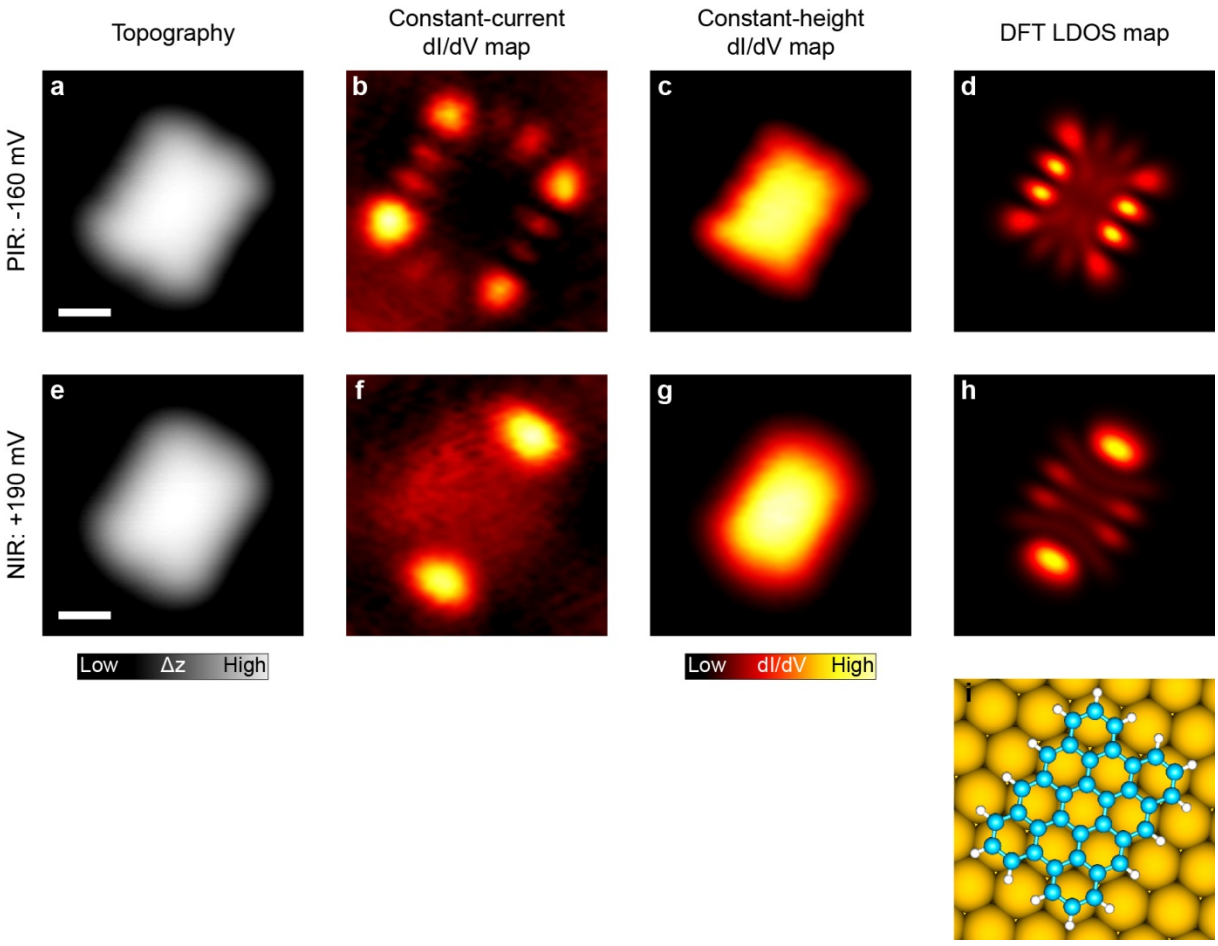

Figure S4 | Constant-current and constant-height d*I*/d*V* maps of 1. (a), (e) High-resolution STM images at the PIR (a) and the NIR (e). **(b), (f)** Simultaneously acquired constant-current d*I*/d*V* maps at the PIR (b) and the NIR (f). **(c), (g)** Constant-height d*I*/d*V* maps at the PIR (c) and the NIR (g). **(d), (h)** DFT-calculated LDOS maps at the PIR (d) and the NIR (h), evaluated at a height of 5 Å above the molecular plane. **(i)** Corresponding DFT-optimized equilibrium geometry of **1** on Au(111). Tunneling parameters for the STM images and the constant-current d*I*/d*V* maps: (a), (b) – V = -160 mV, I = 150 pA; V_{rms} = 20 mV; (e), (f) – V = 190 mV, I = 170 pA; V_{rms} = 20 mV. Open feedback parameters for the constant-height d*I*/d*V* maps: (c) – V = -160 mV, I = 160 pA; V_{rms} = 20 mV; (g) – V = 190 mV, I = 180 pA; V_{rms} = 20 mV. All scale bars: 0.5 nm.

5. DFT-calculated gas-phase molecular orbitals of 1

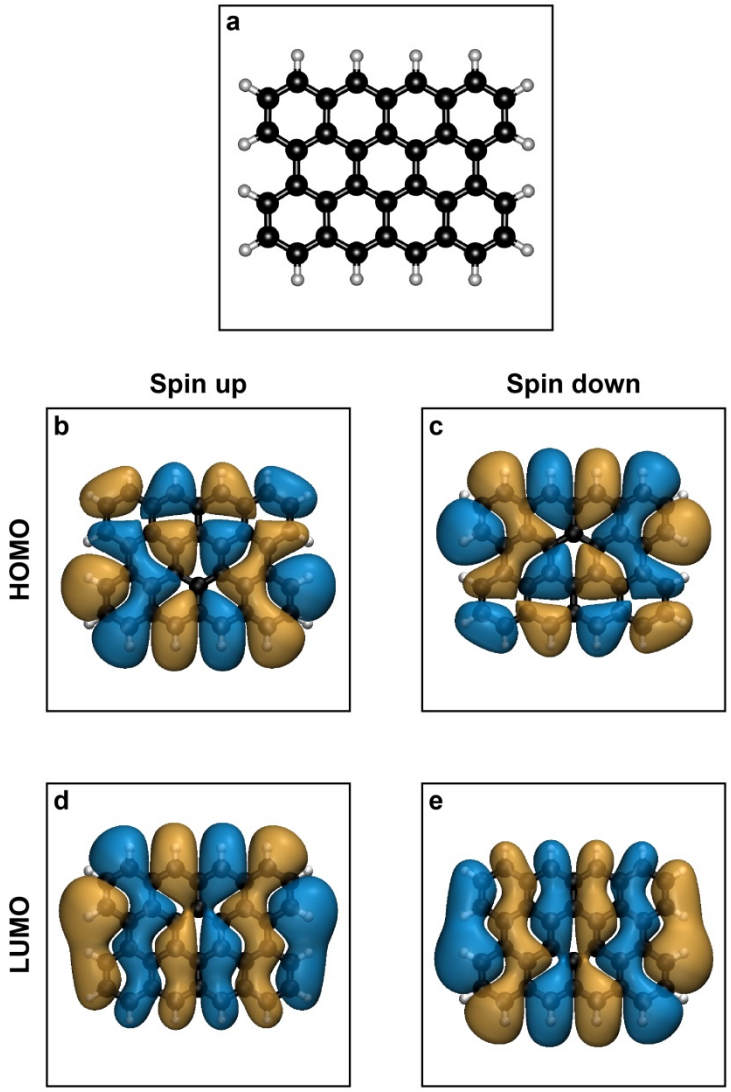

Figure S5 | Spin-polarized-DFT-calculated frontier orbitals of 1. (a) DFT-optimized equilibrium geometry of **1** in the gas-phase. **(b), (c)** Highest occupied molecular orbital (HOMO) for spin up (b) and spin down (c) channels. **(d), (e)** Lowest unoccupied molecular orbital (LUMO) for spin up (d) and spin down (e) channels. The blue and brown isosurfaces denote opposite signs of the wavefunctions.

6. Room temperature phase of 4

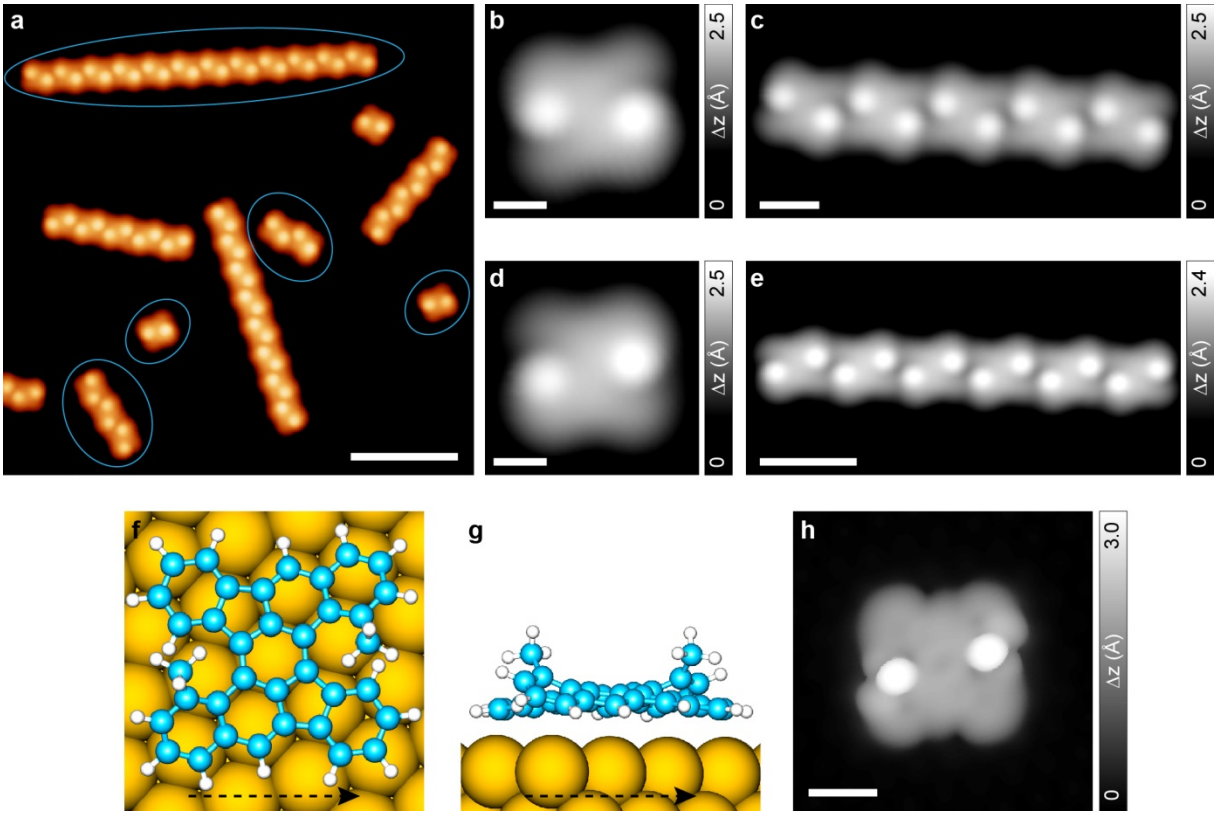

Figure S6 | Room temperature phase of 4 on Au(111). (a) High-resolution large-scale STM image showing the coexistence of self-assembled chains of varying lengths, and individual molecules. Chirality is observed in both the single molecules and the chains. Species highlighted by blue ellipses correspond to the same chirality, while unhighlighted species possess the opposite chirality. **(b), (c)** High-resolution STM image of a single molecule and a chain with the same chirality; and **(d), (e)** High-resolution STM image of a single molecule and a chain of opposite chirality than in (b), (c). **(f), (g)** Top and side views of the DFT-optimized equilibrium geometry of **4** on Au(111). **(h)** DFT-simulated STM image of **4** on Au(111) showing excellent agreement with the experimental STM image, evidencing the structural integrity of **4** on the surface (V = -500 mV). Tunneling parameters: (a) V = -1.0 V, I = 80 pA; (b)-(e) V = -20 mV, I = 100 pA. Scale bars: (a) – 5 nm; (b), (d), (h) – 0.5 nm; (c) – 1 nm; (e) – 2 nm.

7. Height-dependent UHR-STM images of 2´´

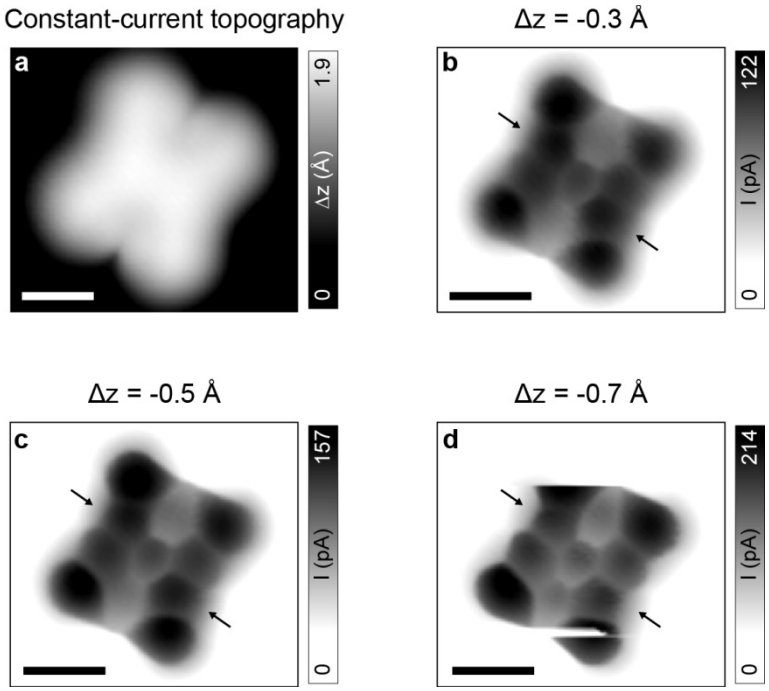

Figure S7 | UHR-STM imaging of 2´´ at different tip-molecule distances. (a) High-resolution STM image of **2´´** acquired with a CO-functionalized tip (V = -30 mV, I = 50 pA). **(b)-(d)** Corresponding UHR-STM images acquired at different tip-molecule distances. The black arrows indicate the pentagonal rings. The armchair-shaped bay regions formed by the peripheries of the pentagonal and the adjacent hexagonal rings become apparent only upon approaching the tip closer to the molecule (as in (c) and (d)). The instability in (d) arises as a result of the lateral movement of the molecule due to repulsive interaction with CO at the tip apex. For each image, the lowering of the tip height Δz, after the feedback loop was opened, is indicated at the top. Open feedback parameters: (b)-(d) V = - 5 mV, I = 50 pA. All scale bars: 0.5 nm.

8. Comparison of constant-height and constant-current d*I*/d*V* maps of 2´´

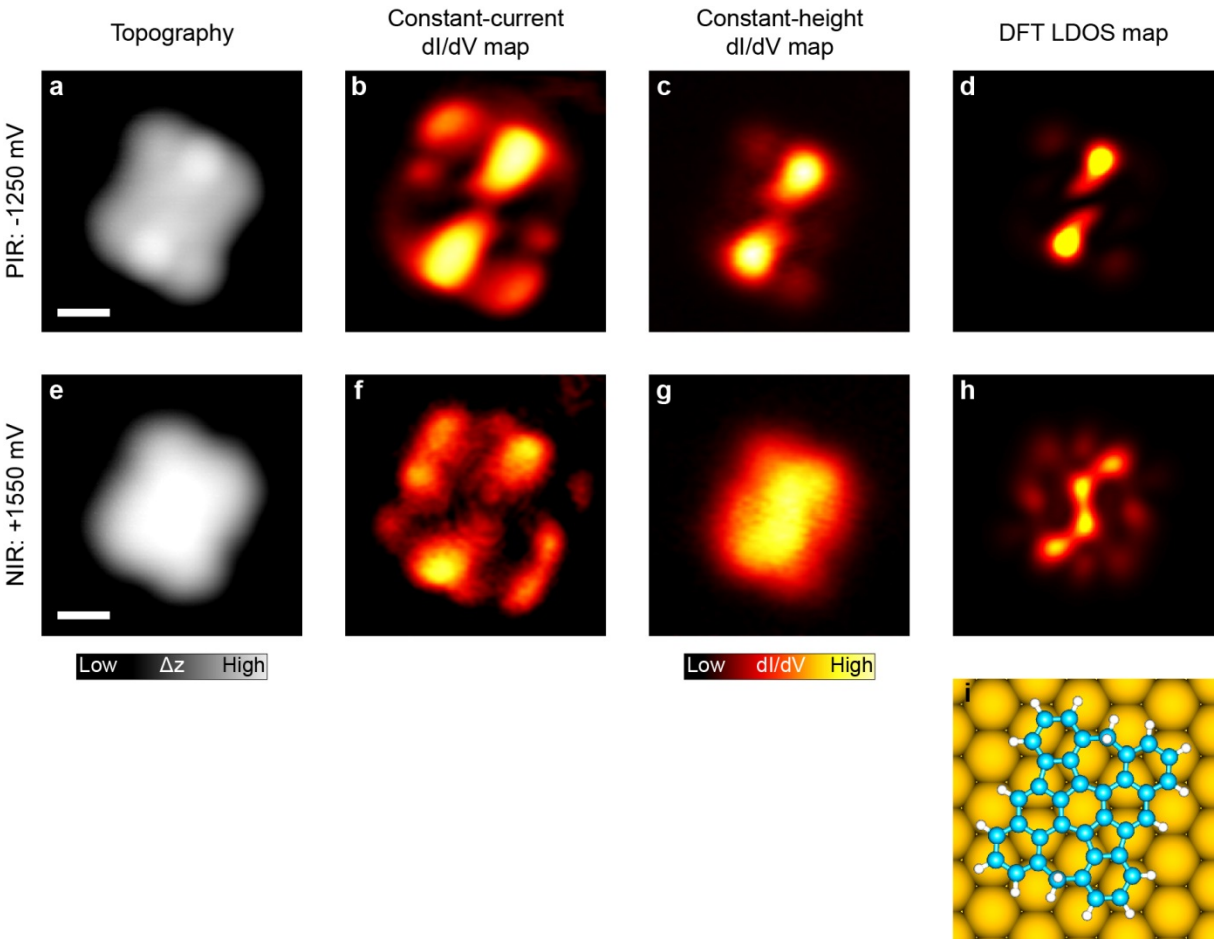

Figure S8 | Constant-current and constant-height d*I*/d*V* maps of 2´´. (a), (e) High-resolution STM images at the PIR (a) and the NIR (e) acquired with a CO-functionalized tip. **(b), (f)** Simultaneously acquired constant-current d*I*/d*V* maps at the PIR (b) and the NIR (f). **(c), (g)** Constant-height d*I*/d*V* maps at the PIR (c) and the NIR (g) acquired with a CO-functionalized tip. **(d), (h)** DFT-calculated LDOS maps at the PIR (d) and the NIR (h), evaluated at a height of 3 Å above the molecular plane. **(i)** Corresponding DFT-optimized equilibrium geometry of **2´´** on Au(111). Tunneling parameters for the STM images and the constant-current d*I*/d*V* maps: (a), (b) – V = -1.26 V, I = 140 pA; V_{rms} = 20 mV; (e), (f) – V = 1.58 V, I = 140 pA; V_{rms} = 20 mV. Open feedback parameters for the constant-height d*I*/d*V* maps: (c) – V = -1.26 V, I = 150 pA; V_{rms} = 20 mV; (g) – V = 1.58 V, I = 220 pA; V_{rms} = 20 mV. All scale bars: 0.5 nm.

9. Controlled on-surface generation of 2 *via* STM atom manipulation

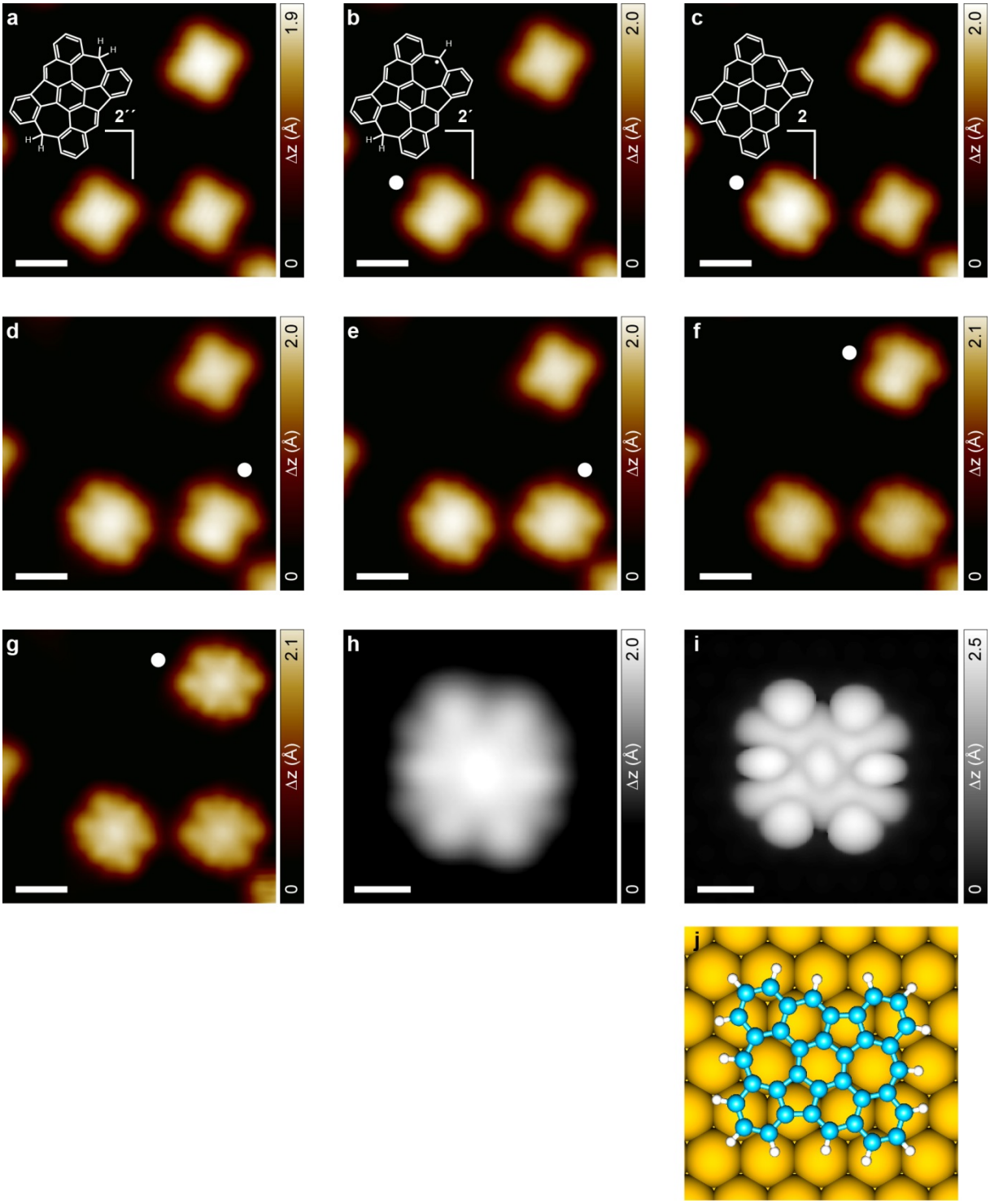

Figure S9 | Voltage-pulse-induced dehydrogenation of 2´´ to generate 2. (a)-(g) Series of STM images showing sequential voltage-pulse-induced dehydrogenation of three molecular species **2´´** to generate the fully conjugated species **2** *via* the radical intermediate **2´** (chemical structures of the corresponding species for a complete manipulation sequence of the bottom-left molecule are shown in (a)-(c)). The white marker indicates the species manipulated in each image ((a), (b) V = -200 mV, I = 50 pA; (c)-(f) V = -70 mV, I = 70 pA; (g) V = -10 mV, I

= 100 pA). **(h)** High-resolution STM image of **2** (V = -7 mV, I = 100 pA). **(i)** DFT-simulated STM image of **2** on Au(111) (V = -250 mV, scale bar: 0.5 nm). **(j)** Corresponding DFT-optimized equilibrium geometry of **2** on Au(111). Scale bars: (a)-(g) – 1 nm; (h), (i) – 0.5 nm.

10. Comparison of experimental and simulated STM images of 2´

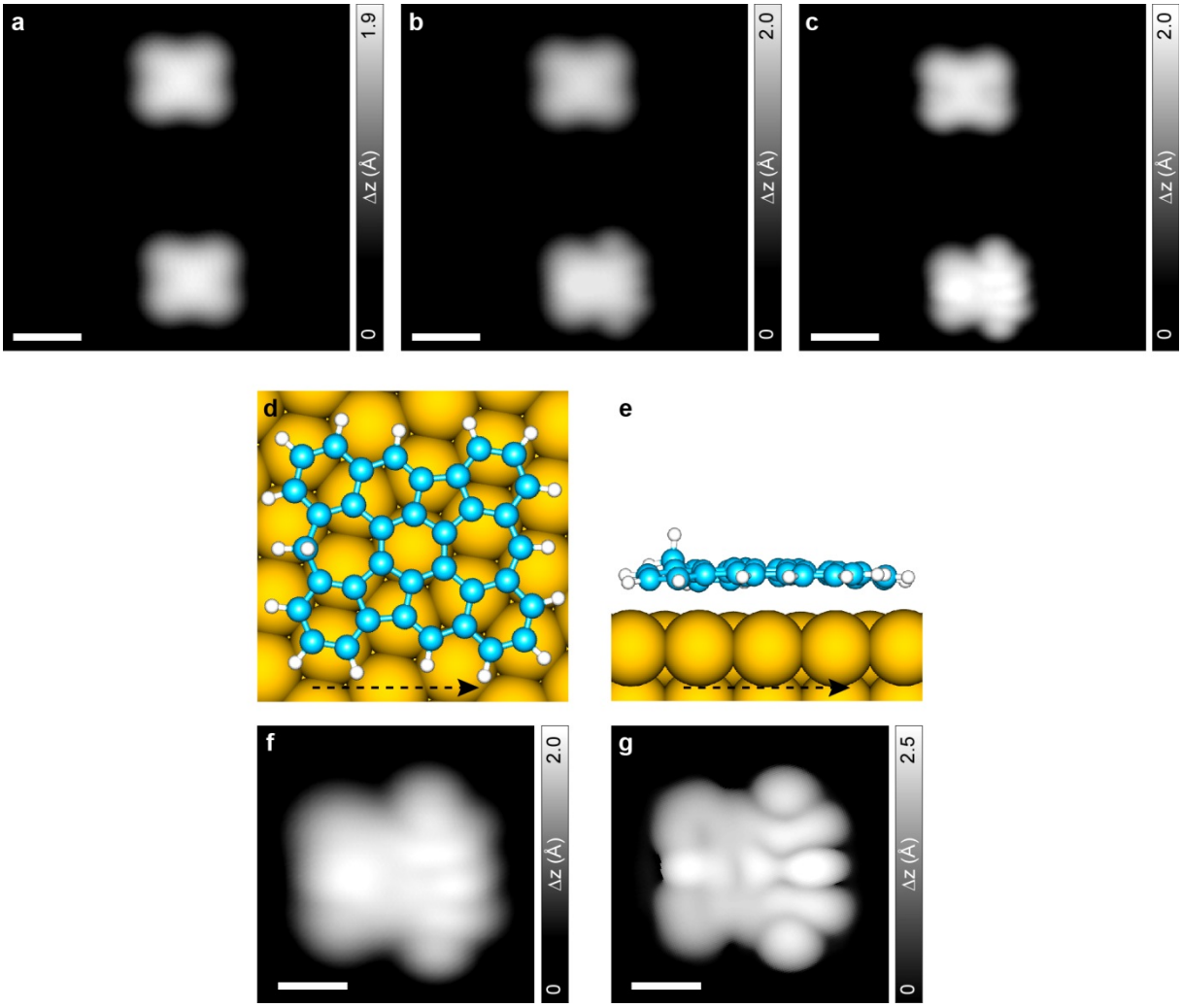

Figure S10 | Experimental and simulated STM images of 2´. (a), (b) High-resolution STM images of a pair of **2´´** species before (a) and after (b) the lower species was manipulated to generate the intermediate radical species **2´** (V = -100 mV, I = 50 pA). **(c)** Same scan frame as in (b) acquired with a CO-functionalized tip providing enhanced resolution (V = -100 mV, I = 50 pA). **(d), (e)** Top and side views of the DFT-optimized equilibrium geometry of **2´** on Au(111). **(f), (g)** High-resolution STM image of **2´** acquired with a CO-functionalized tip ((f), V = -100 mV, I = 50 pA) and the corresponding DFT-simulated STM image ((g), V = -250 mV). The excellent agreement between the experimental and the simulated STM images evidences that the first manipulation event leads to the formation of the intermediate radical species **2´**. Note that the bond dissociation energy for the CH group is much higher (4.8 eV in benzene[1]), a range not reached in our manipulation experiments, thus ensuring that only selective cleavage of a single hydrogen atom from CH_2 moieties is achieved upon manipulation. Scale bars: (a)-(c) – 1 nm; (f), (g) – 0.5 nm.

11. Annealing of 4 on Au(111) at 350°C

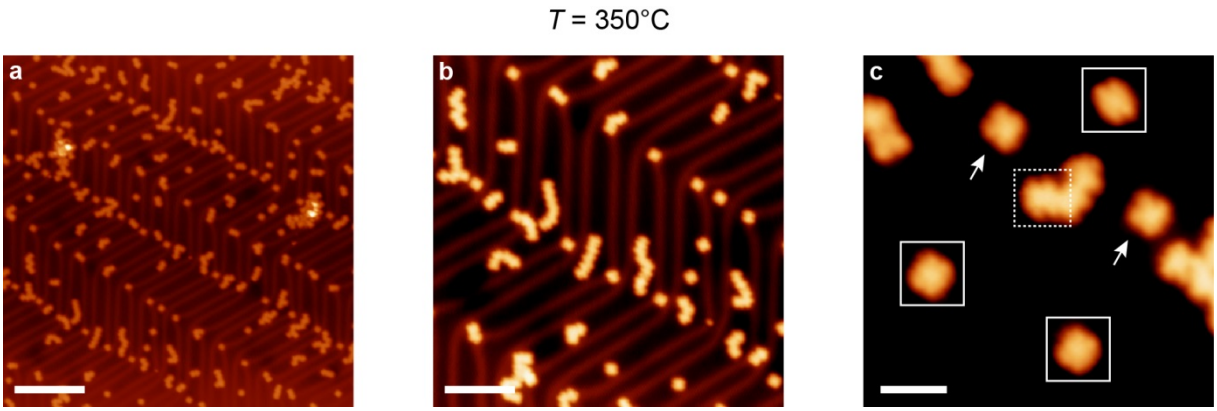

Figure S11 | High temperature annealing of 4 on Au(111). (a), (b) Overview STM topography images of the surface after room temperature deposition of **4** and annealing at 350°C ((a) V = -2 V, I = 30 pA; (b) V = -700 mV, I = 50 pA). **(c)** High-resolution STM image showing the species present on the surface (V = -100 mV, I = 150 pA). Individual species corresponding to **2** are highlighted by solid rectangles, while the dashed rectangle highlights **2** as a constituent unit of a molecular cluster. Arrows indicate individual **2´** species. After annealing to 300°C, the surface consists of individual **2** and **2´** species, and irregular covalently-bonded molecular clusters consisting of **2** and **2´**. Scale bars: (a) – 20 nm; (b) – 10 nm; (c) – 3 nm.

12. Height-dependent UHR-STM images of 2

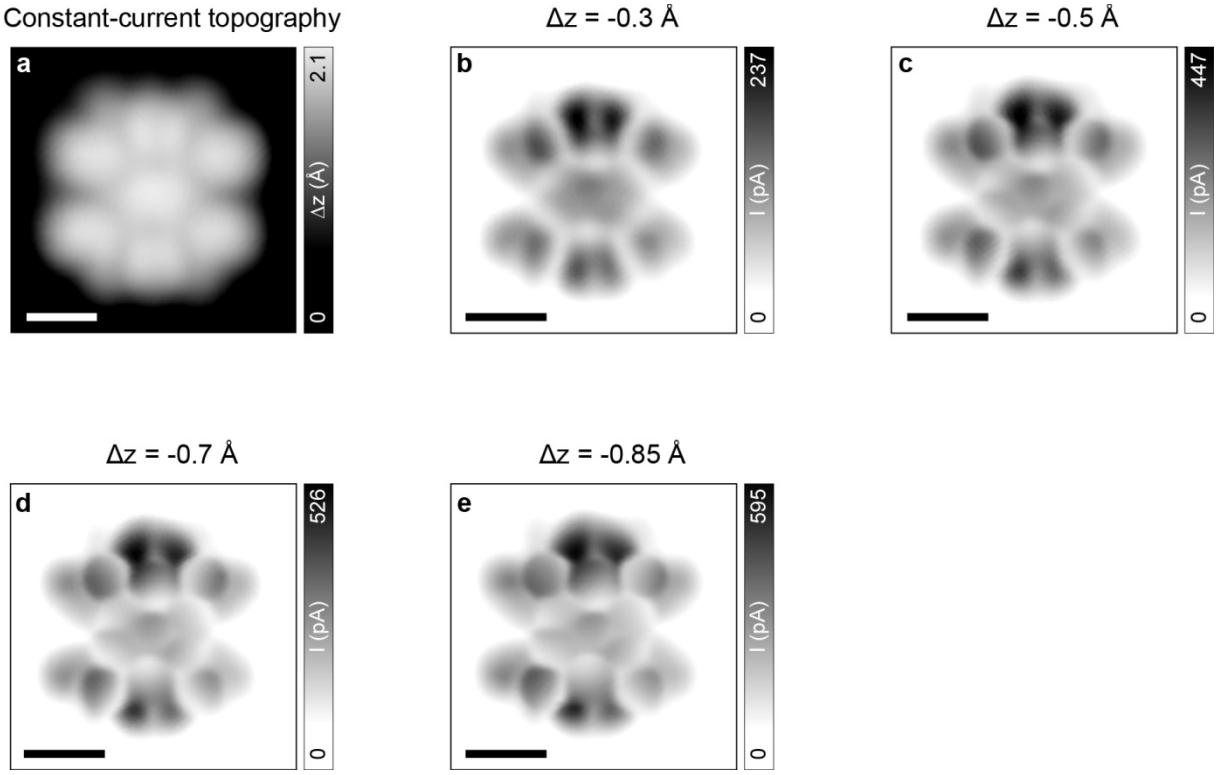

Figure S12 | UHR-STM imaging of 2 at different tip-molecule distances. (a) High-resolution STM image of **2** acquired with a CO tip (V = -100 mV, I = 50 pA). **(b)-(e)** Corresponding UHR-STM images acquired at different tip-molecule distances. For larger tip-molecule distances (*e.g.* in (b)), the UHR-STM image is completely dominated by the LDOS. For each image, the lowering of the tip height Δ*z*, after the feedback loop was opened, is indicated at the top. Open feedback parameters: (b)-(e) V = - 5 mV, I = 50 pA. All scale bars: 0.5 nm.

13. Comparison of constant-height and constant-current d*I*/d*V* maps of 2

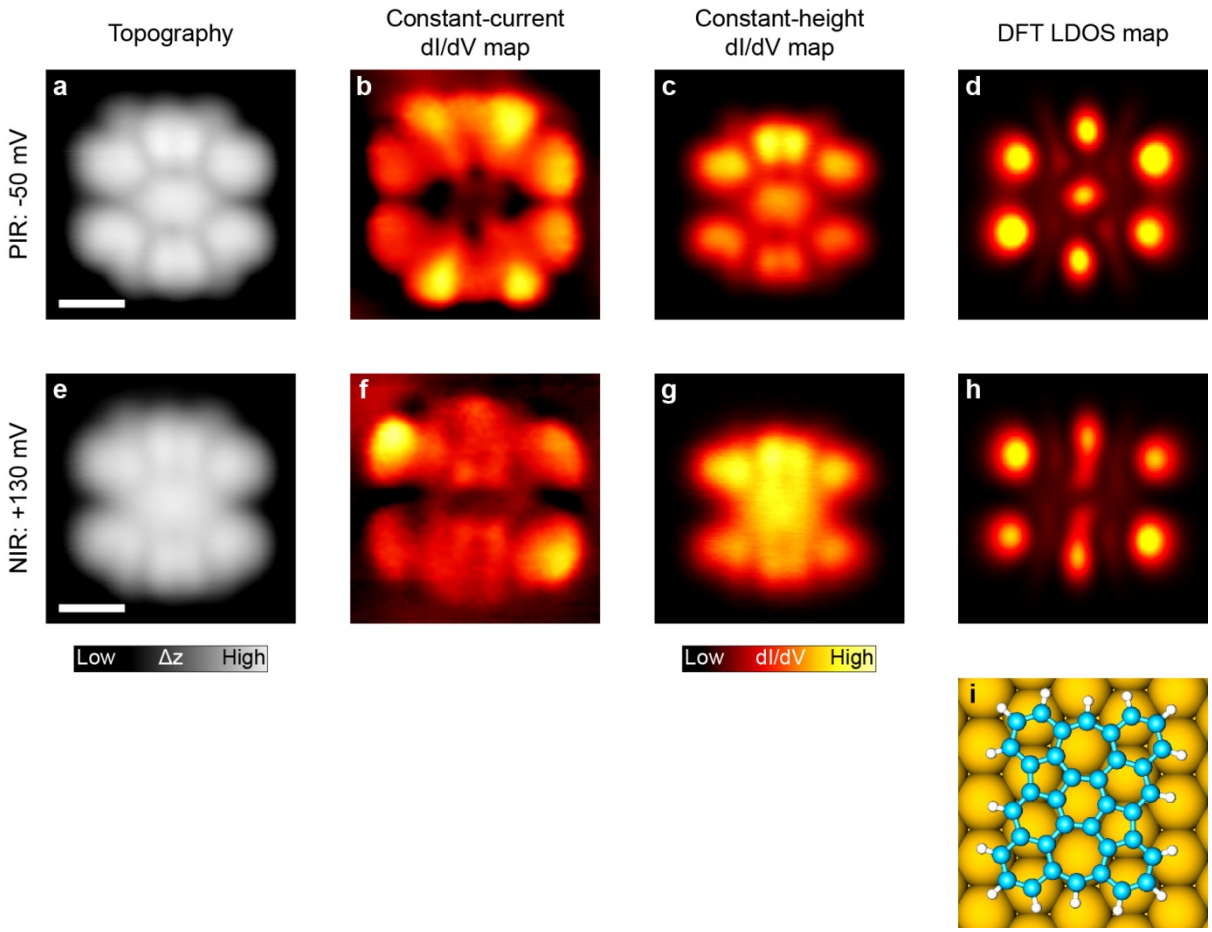

Figure S13 | Constant-current and constant-height d*I*/d*V* maps of 2. (a), (e) High-resolution STM images at the PIR (a) and the NIR (e) acquired with a CO-functionalized tip. **(b), (f)** Simultaneously acquired constant-current d*I*/d*V* maps at the PIR (b) and the NIR (f). **(c), (g)** Constant-height d*I*/d*V* maps at the PIR (c) and the NIR (g) acquired with a CO-functionalized tip. **(d), (h)** DFT-calculated LDOS maps at the PIR (d) and the NIR (h), evaluated at a height of 5 Å above the molecular plane. **(i)** Corresponding DFT-optimized equilibrium geometry of **2** on Au(111). Tunneling parameters for the STM images and the constant-current d*I*/d*V* maps: (a), (b) – V = -50 mV, I = 150 pA; V_{rms} = 20 mV; (e), (f) – V = 120 mV, I = 150 pA; V_{rms} = 20 mV. Open feedback parameters for the constant-height d*I*/d*V* maps: (c) – V = -50 mV, I = 130 pA; V_{rms} = 20 mV; (g) – V = 130 mV, I = 150 pA; V_{rms} = 20 mV. All scale bars: 0.5 nm.

14. DFT-calculated gas-phase molecular orbitals of 2

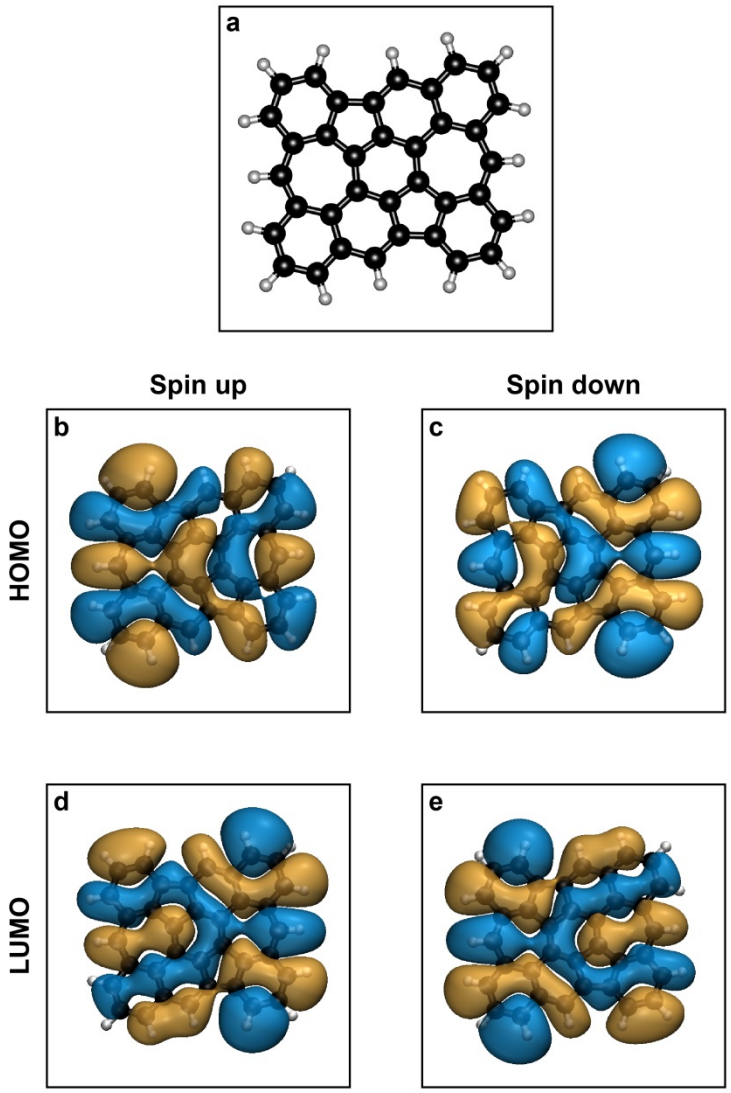

Figure S14 | Spin-polarized-DFT-calculated frontier orbitals of 2. (a) DFT-optimized equilibrium geometry of **2** in the gas-phase. **(b), (c)** Highest occupied molecular orbital (HOMO) for spin up (b) and spin down (c) channels. **(d), (e)** Lowest unoccupied molecular orbital (LUMO) for spin up (d) and spin down (e) channels. The blue and brown isosurfaces denote opposite signs of the wavefunctions.

15. Synthetic procedures, instrumentation and characterization methods

General

The reactions were performed using standard vacuum-line and Schlenk techniques; synthesis and purification of all compounds were performed under air and with reagent-grade solvents. Column chromatography was done with silica gel (particle size 0.063-0.200 mm from VWR) and silica coated aluminum sheets with fluorescence indicator from Merck were used for thin layer chromatography. NMR spectra were recorded on Bruker spectrometer (300, 500 or 600 MHz) and $CDCl_3$ ($\delta(^1H)$ = 7.26 ppm, $\delta(^{13}C)$ = 77.2 ppm), CD_2Cl_2 ($\delta(^1H)$ = 5.32 ppm, $\delta(^{13}C)$ = 54.0 ppm) or $C_2D_2Cl_4$ ($\delta(^1H)$ = 6.00 ppm; $\delta(^{13}C)$ = 73.8 ppm) were used as solvent, lock and internal standard. Coupling constants (*J* values) are given in Hz whereas chemical shifts are reported in parts per million (ppm). Splitting patterns are designated as s (singlet), d (doublet), t (triplet), q (quartet), and m (multiplets). The high-resolution mass spectrometry analyses were performed by using Bruker Autoflex MALDI TOF (dithranol or TCNQ as matrix) and Agilent Q-TOF (APCI mode using acetonitrile as solvent) instruments. The recycling gel permeation chromatography (rGPC) was recorded on JAI HPLC LC 9110 II NEXT with fraction collector FC-3310 and GPC columns 2H and 1H (connected in series). The rGPC was used with HPLC-grade chloroform at room temperature. Melting points were determined on a Büchi Melting Point M-560 in a range of 50-400°C with a temperature rate of 10°C/min. Elemental analysis was measured at Vario MICRO cube device by Elementar.

Materials

All the starting materials were obtained from Sigma Aldrich, TCI, ABCR, or chemPUR, and catalysts were purchased from Strem. All chemicals were used as received. Dry solvents were used without further purification.

Synthesis of 7,14-Di-(2-methylphenyl)benzo[*k*]tetraphene (3)

Compound **3** was synthesized as shown in Supplementary Figure 14.

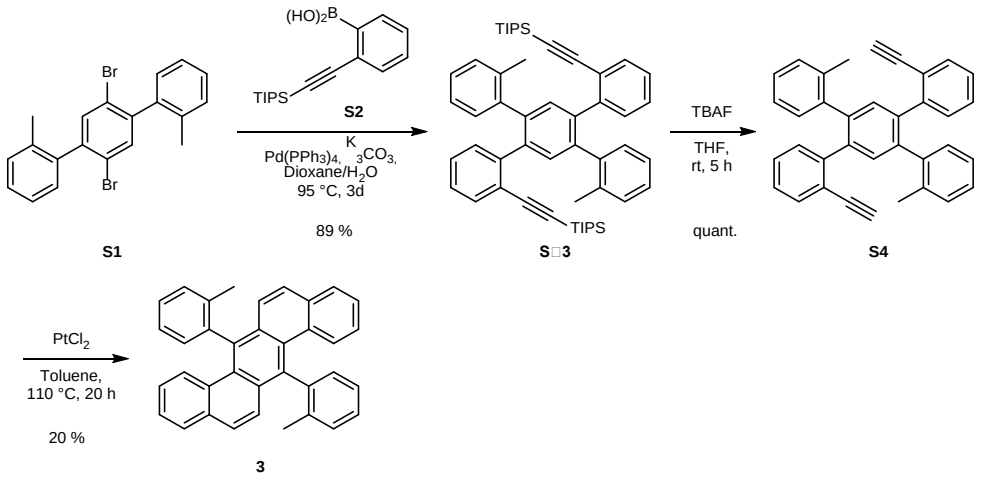

Figure S15 | Synthetic route towards compound **3**.

1,4-Di(2-methylphenyl)-2,5-di(2-((triisopropylsilyl)ethynyl)phenyl)benzene (S3)

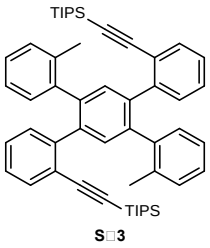

In a two-necked round-bottom flask equipped with a condenser, a mixture of terphenyl **S1**[2] (1.90 g, 4.57 mmol), (2-((triisopropylsilyl)ethynyl)phenyl)boronic acid **S2**[3] (4.83 g, 15.98 mmol) and potassium carbonate (3.38 g, 24.00 mmol) was dissolved in dioxane (54 ml). Then water (12 ml) was added, the mixture was degassed with argon for 30 minutes and tetrakis(triphenylphosphine)palladium(0) (264 mg, 0.20 mmol) was added. The reaction mixture was heated to 95°C for 72 h. After cooling, the reaction mixture was diluted with 200 ml dichloromethane, the organic layer was washed with water (3×100 mL) and dried over magnesium sulfate. After removal of the solvent under reduced pressure, the residue was first purified by column chromatography (cyclohexane:dichloromethane = 20:1, later 15:1), then washed with cold pentane to obtain the title compound (3.13 g, 89%) as a white solid. mp: 241-242°C; ^{1}H-NMR (600 MHz, $C_2D_2Cl_4$, 80°C): δ (ppm) 7.55-7.53 (m, 4H), 7.39 (d, J = 7.9 Hz, 2H), 7.14-7.05 (m, 10H), 6.98 (dd, J = 7.8 Hz, 0.9 Hz, 2H), 2.18 (s, 6H), 1.10 (s, 42H); ^{13}C NMR (151 MHz, $C_2D_2Cl_4$, 80°C): δ (ppm) 143.12, 140.48, 138.84, 138.82, 135.99, 133.57, 132.77, 130.92, 130.81, 129.33, 126.91, 126.53, 126.05, 124.54, 122.84, 107.08,

93.96, 20.31, 18.45, 11.33; HR-MS (APCI, pos) *m/z*: [(M+H)$^+$] calcd for $C_{54}H_{67}Si_2$: 771.4776; found: 771.4779; elemental analysis calcd for $C_{54}H_{66}Si_2$: C 84.09; H 8.63; found C 84.35; H 8.62.

1,4-Di(2-methylphenyl)-2,5-di((2-ethynyl)phenyl)benzene (S4)

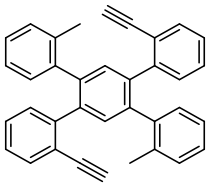

S4

Compound **S3** (1.60 g, 2.07 mmol) was dissolved in 60 mL degassed tetrahydrofuran, then tetrabutylammonium fluoride (2.5 ml, 1 M in tetrahydrofuran) was added dropwise to the solution. After 30 min, the reaction was quenched with methanol. The solvent was removed under vacuum, the residue was filtered and washed with methanol and pentane. After drying under vacuum, the target compound was obtained as a white solid (0.95 g, quant.). mp: ≥ 260°C (dec.); ^{1}H NMR (600 MHz, $C_2Cl_4D_2$, 80°C): δ (ppm) 7.53 (dd, J = 7.6 Hz, 1.2 Hz, 2H), 7.49 (s, 2H), 7.21 (d, J = 7.4 Hz, 2H), 7.15 (td, J = 7.5 Hz, 1.5 Hz, 2H), 7.12-7.09 (m, 6H), 7.07-7.04 (m, 4H), 3.11 (s, 2H), 2.25 (s, 6H); ^{13}C NMR (151 MHz, $C_2Cl_4D_2$, 80°C): δ (ppm) 140.36, 138.79, 138.26, 132.88, 132.79, 130.57, 129.45, 127.47, 126.64, 126.27, 124.68, 80.06, 20.04; HR-MS (APCI, pos.) *m/z*: [(M+H)$^+$] calcd for $C_{36}H_{27}$: 459.2107; found: 459.2105; elemental analysis calcd for $C_{36}H_{26}$: C 94.29; H 5.71; found C 94.08; H 5.84.

7,14-Di-(2-methylphenyl)benzo[*k*]tetraphene (3)

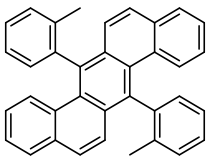

3

A reaction flask containing platinum(II) chloride (58 mg, 0.22 mmol) was dried in vacuum for 1 h, then filled with argon. To this round bottom flask, **S4** (200 mg, 0.44 mmol) and toluene (160 mL) were added, and the mixture was stirred at 25°C for 5 min before it was heated at 110°C for 24 h. After removal of solvent in vacuum, the crude material was purified by column chromatography (dichloromethane:cyclohexane = 1:15) and washed with pentane to afford the title compound (40 mg, yield: 20%) as a light yellow solid. mp: 238-240°C; ^{1}H NMR (600 MHz, $C_2D_2Cl_4$, 80°C): δ (ppm) 7.81 (dd, J = 7.7 Hz, 1.3 Hz, 2H), 7.65-7.53 (m, 2H), 7.59-7.54 (m, 6H), 7.50-7.46 (m, 6H), 7.39-7.35 (m, 2H), 7.18-7.15 (ddd, J = 8.6 Hz, 7.0 Hz, 1.5 Hz, 2H), 1.99-1.97 (m, 6H); ^{13}C NMR (151 MHz, $C_2D_2Cl_4$, 80°C): δ (ppm) 142.60,

142.58, 137.48, 137.44, 136.48, 136.42, 132.99, 132.97, 131.20, 131.02, 130.98, 130.68, 130.64, 130.54, 130.53, 127.92, 127.88, 127.87, 127.83, 127.81, 127.67, 127.64, 127.20, 127.14, 126.85, 126.80, 126.11, 126.08, 125.38, 125.32, 125.29, 19.63; HR-MS (MALDI-TOF) *m/z*: $[(M)^+]$ calculated for $C_{36}H_{26}$: 458.2035; found: 458.2054; elemental analysis calcd for $C_{36}H_{26}$: C 94.29; H 5.71; found C 94.28; H 5.48.

Synthesis of 1,10-Dimethyldibenzo[*a*,*m*]rubicene (4)

Compound **4** was synthesized as shown in Supplementary Figure 15.

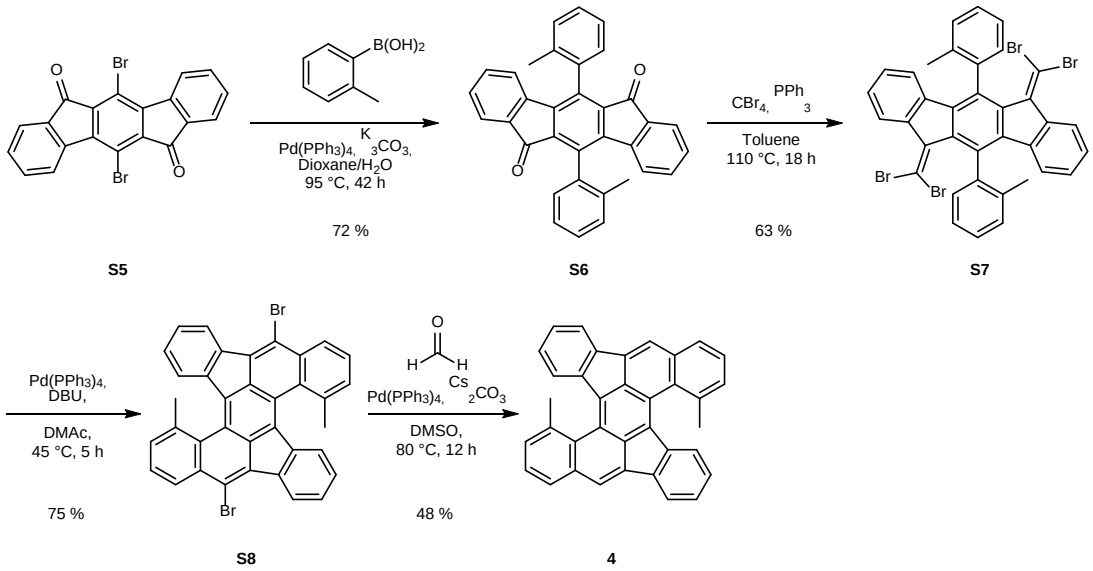

Figure S16 | Synthetic route towards compound **4**.

5,11-Di-(2-methylphenyl)indeno[1,2-*b*]fluorene-6,12-dione (S6)

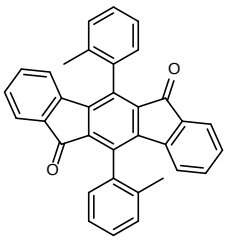

S6

A 250 mL round-bottom Schlenk flask was charged with 5,11-dibromoindeno[1,2-*b*]fluorine-6,12-dione[4] (**S5**, 1.01 g, 2.29 mmol), 2-methylbenzeneboronic acid (2.18 g, 16.06 mmol), potassium carbonate (5.71 g, 41.31 mmol) and tetrakis(triphenylphosphine)palladium(0) (530 mg, 0.46 mmol) and was evacuated and charged with argon three times. Then degassed 1,4-dioxane (225 mL) and water (22 mL) were added and the reaction mixture was heated at 95°C for 42 h under argon atmosphere. After cooling to the room temperature, the mixture was poured into water and extracted with dichloromethane. The organic layer was washed by brine and dried over anhydrous magnesium sulfate. The solvent was removed under vacuum and the residue was purified by silica gel column chromatography (cyclohexane:ethyl acetate = 15:1) as eluent to give target compound as a red solid (0.77 g, yield: 72%). mp: 354°C; ^{1}H NMR (600 MHz, CD_2Cl_2): δ 7.52-7.48 (m, 4H), 7.45 (d, *J* = 7.6 Hz, 2H), 7.39 (t, *J* = 7.4 Hz,

2H), 7.30-7.26 (m, 2H), 7.21-7.15 (m, 4H), 6.14 (d, J = 7.5 Hz, 2H), 2.16 (s, 6H). ^{13}C NMR (151 MHz, CD_2Cl_2): δ (ppm)192.72, 192.70, 145.09, 143.55, 143.53, 136.54, 136.48, 136.30, 135.88, 135.86, 135.40, 134.87, 130.77, 130.75, 129.50, 129.12, 128.75, 126.92, 124.11, 123.35, 123.33, 20.12, 20.04; HR-MS (APCI, pos) *m/z*: [(M+H)$^+$] calcd for $C_{34}H_{23}O_2$: 463.1693; found: 463.1696.

5,11-Di(2-methylphenyl)-6,12-bis(dibromomethylene)-6*H*,12*H*-indeno[1,2-*b*]fluorene (S7)

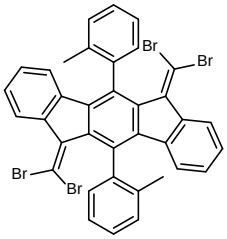

S7

5,11-Di-(2-methylphenyl)indeno[1,2-*b*]fluorene-6,12-dione (**S6**, 0.16 g, 0.35 mmol), triphenylphosphane (1.09 g, 4.15 mmol) and tetrabromomethane (0.69 g, 2.08 mmol) were dissolved in 6.25 mL of dry and degassed toluene under argon atmosphere. The solution was refluxed for 18 h, and then cooled to room temperature. The resulting mixture was filtered through celite and washed with toluene. The filtrate was collected, and concentrated under a reduced pressure. The residue was purified by column chromatography (cyclohexane:dichloromethane = 10:1) to yield **S7** (0.17 g, 0.22 mmol, 63%) as a yellow solid. mp: ≥ 248°C (dec.); ^{1}H NMR (500 MHz, CD_2Cl_2): δ (ppm) 8.27-8.25 (m, 2H), 7.54-7.33 (m, 7H), 7.16-7.12 (m, 3H), 6.98-6.94 (m, 2H), 6.33-6.22 (m, 2H), 2.36-2.14 (m, 6H); ^{13}C NMR (151 MHz, CD_2Cl_2): δ (ppm) 144.33, 142.80, 141.54, 140.05, 138.82, 133.32, 133.13, 131.65, 131.53, 129.34, 129.29, 127.31, 127.27, 126.64, 126.52, 125.13, 121.99, 121.17, 21.20; HR-MS (APCI, pos) *m/z*: [(M+H)$^+$] calcd for $C_{36}H_{23}Br_4$: 774.8487; found: 774.8492.

5,14-Dibromo-1,10-dimethyldibenzo[*a*,*m*]rubicene (S8)

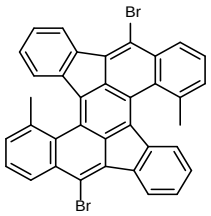

S8

5,11-Di(2-methylphenyl)-6,12-bis(dibromomethylene)-6*H*,12*H*-indeno[1,2-*b*]fluorene (**S7**, 519 mg, 0.67 mmol), tetrakis(triphenylphosphine)palladium(0) (155 mg, 0.13 mmol) and 1,8-

diazabicyclo[5.4.0]undec-7-ene (0.41 mL, 2.68 mmol) were dissolved in 10 mL of dry and degassed *N*,*N*-dimethylacetamide in a sealed tube, and heated at 45°C for 5 h. The reaction mixture was cooled to room temperature resulting in precipitates, which were collected by filtration and washed with methanol. 310 mg (75%, 0.67 mmol) of 5,14-dibromo-1,10-dimethyldibenzo[*a*,*m*]rubicene was collected as red crystals. Analytically pure samples were purified by rGPC. mp: ≥ 352°C (dec.); ^{1}H NMR (300 MHz, CD_2Cl_2): δ (ppm) 8.80 (dd, J = 7.5 Hz, 0.9 Hz, 2H), 8.53 (d, J = 7.6 Hz, 2H), 7.78-7.75 (m, 4H), 7.63 (d, J = 6.9 Hz, 2H), 7.43-7.32 (m, 4H), 2.82 (s, 6H); ^{13}C NMR (151 MHz, $C_2Cl_4D_2$): δ (ppm) 141.69, 137.42, 136.81, 135.39, 134.29, 134.19, 131.54, 131.17, 130.83, 128.41, 128.06, 127.19, 126.41, 124.85, 123.69, 123.33, 121.56, 23.00; HR-MS (MALDI-TOF) *m/z*: [M^+] calcd for $C_{36}H_{20}Br_2$: 611.9911; found: 611.9973; elemental analysis calcd for $C_{36}H_{20}Br_2$: C 70.61; H 3.29; found C 70.57; H 3.64.

1,10-Dimethyldibenzo[*a*,*m*]rubicene (4)

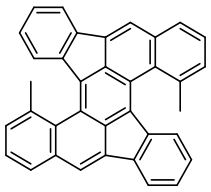

4

5,14-Dibromo-1,10-dimethyldibenzo[*a*,*m*]rubicene (**S8**, 233 mg, 0.34 mmol), paraformaldehyde (51 mg, 1.71 mmol), tetrakis(triphenylphosphine)palladium(0) (79 mg, 0.07 mmol) and caesium carbonate (892 mg, 2.74 mmol) were reacted in dimethyl sulfoxide at 80°C for 20 h. The reaction mixture was cooled to room temperature and the solvent was removed. The residue was purified by column chromatography (cyclohexane:dichloromethane = 6:1) to yield 1,10-dimethyldibenzo[*a*,*m*]rubicene (75 mg, 0.16 mmol, 48%) as an orange solid. Analytically pure samples were achieved by rGPC. mp: 308-311°C; ^{1}H NMR (600 MHz, $CDCl_3$): δ (ppm) 8.13 (s, 2H), 7.94-7.93 (m, 2H), 7.90 (d, J = 7.5 Hz, 2H), 7.80-7.78 (m, 2H), 7.63 (t, J = 7.5 Hz, 2H), 7.58 (d, J = 7.3 Hz, 2H), 7.32-7.29 (m, 4H), 2.87 (s, 6H); ^{13}C NMR (151 MHz, $CDCl_3$): δ (ppm) 142.03, 137.74, 137.42, 135.94, 135.47, 135.29, 132.73, 131.42, 130.07, 127.73, 127.42, 127.34, 126.98, 124.84, 124.30, 122.61, 121.18, 23.06; HR-MS (MALDI-TOF) *m/z*: [M^+] calcd for $C_8H_{11}Br_2O_4$: 454.1788; found: 454.1722; elemental analysis calcd for $C_{36}H_{22}$: C 95.12; H 4.88; found C 95.04; H 4.81.

16. MALDI-TOF and APCI spectra of chemical compounds

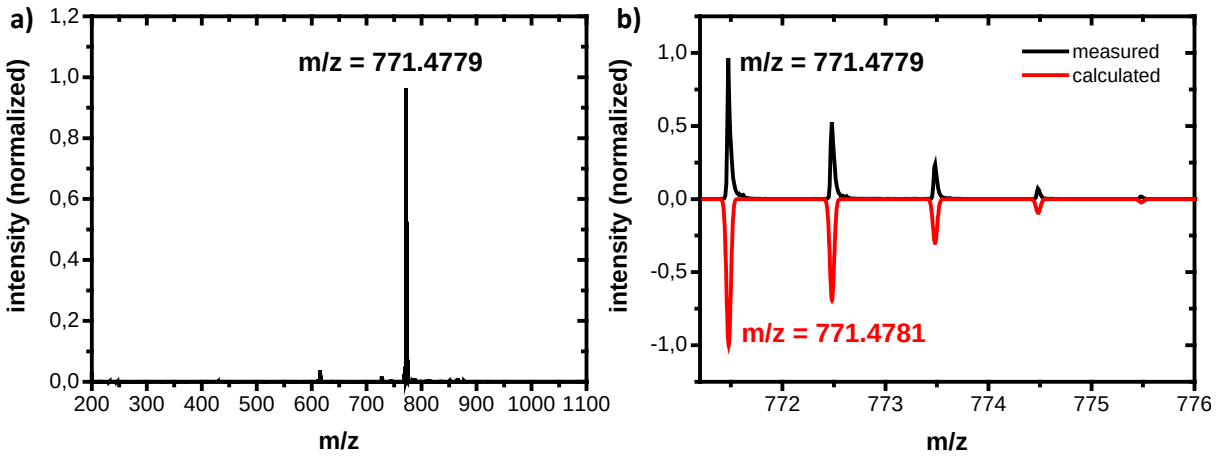

Figure S17 | a) HR-APCI-TOF spectrum of **S3**; b) HR-APCI-TOF magnified spectrum of **S3** (black line) is in agreement to the expected isotopic distribution pattern (red line).

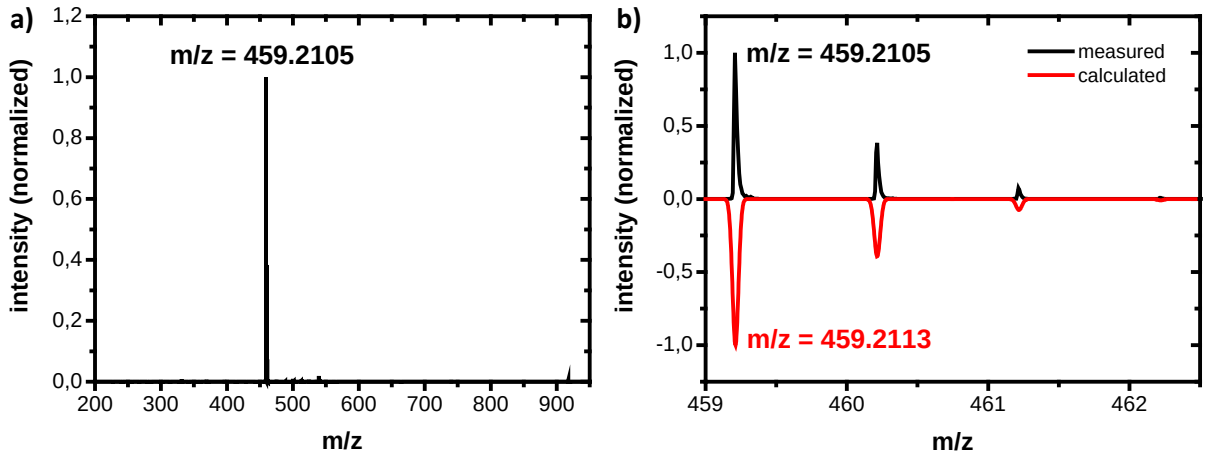

Figure S18 | a) HR-APCI-TOF spectrum of **S4**; b) HR-APCI-TOF magnified spectrum of **S4** (black line) is in agreement to the expected isotopic distribution pattern (red line).

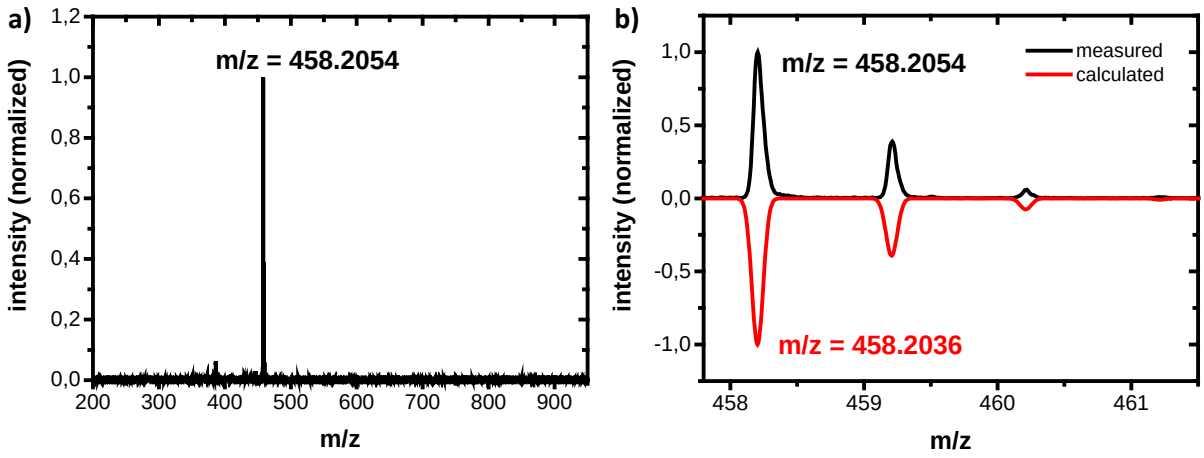

Figure S19 | a) HR-MALDI-TOF spectrum of **3**; b) HR-MALDI-TOF magnified spectrum of **3** (black line) is in agreement to the expected isotopic distribution pattern (red line).

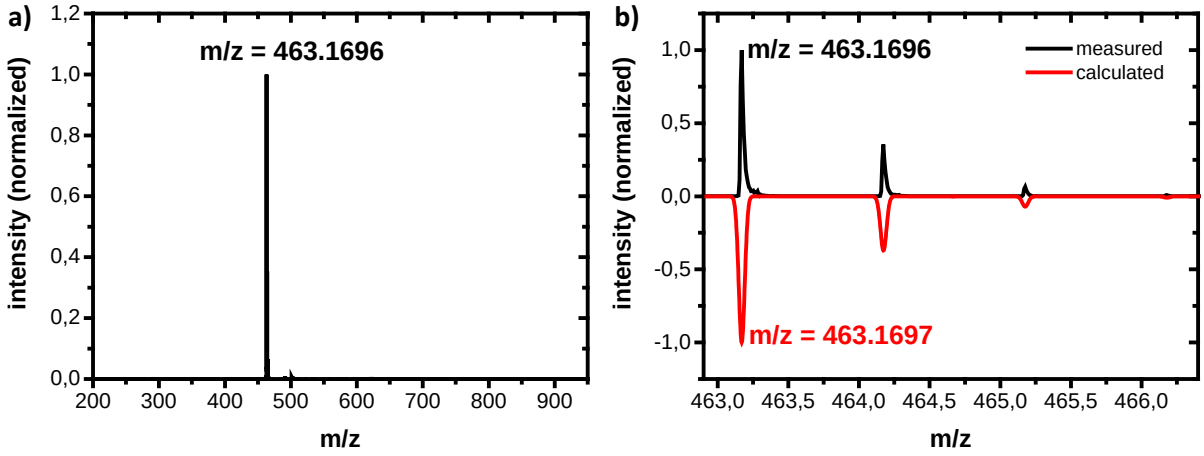

Figure S20 | a) HR-APCI-TOF spectrum of **S6**; b) HR-APCI-TOF magnified spectrum of **S6** (black line) is in agreement to the expected isotopic distribution pattern (red line).

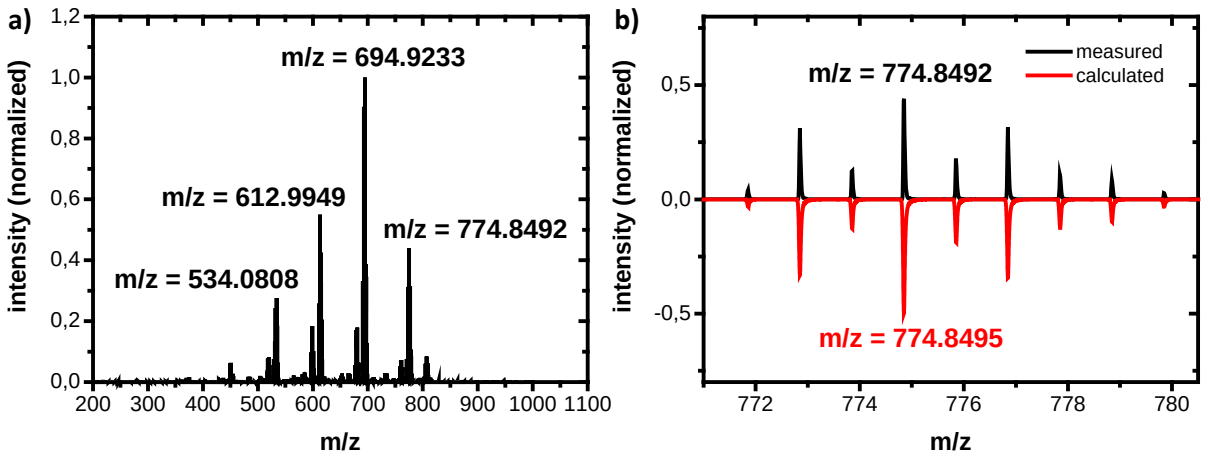

Figure S21 | a) HR-APCI-TOF spectrum of **S7** ($[P+H]^+$, $[P-Br]^+$, $[P-2Br]^+$, $[P-3Br]^+$); b) HR-APCI-TOF magnified spectrum of **S7** (black line) is in agreement to the expected isotopic distribution pattern (red line).

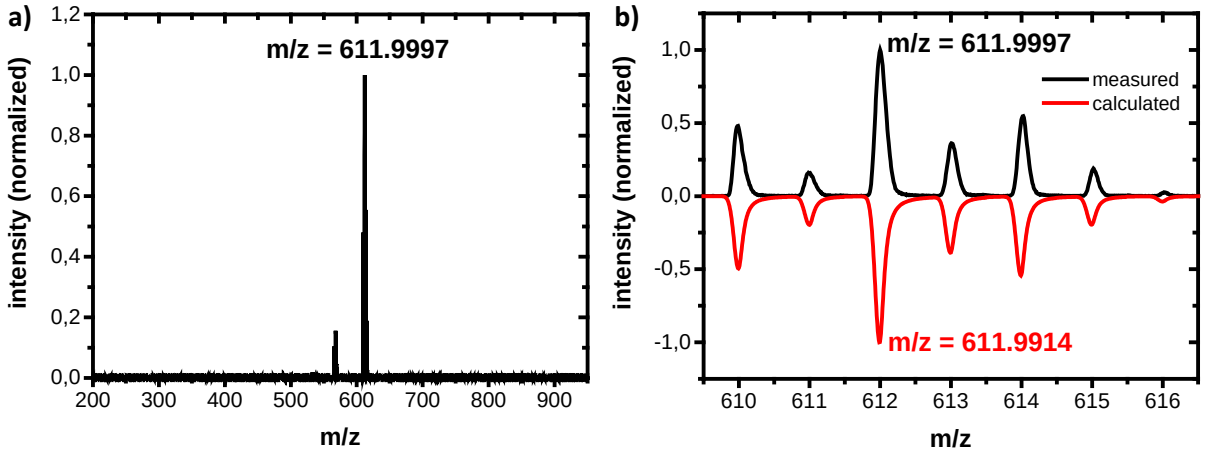

Figure S22 | a) HR-MALDI-TOF spectrum of **S8**; b) HR-MALDI-TOF magnified spectrum of **S8** (black line) is in agreement to the expected isotopic distribution pattern (red line).

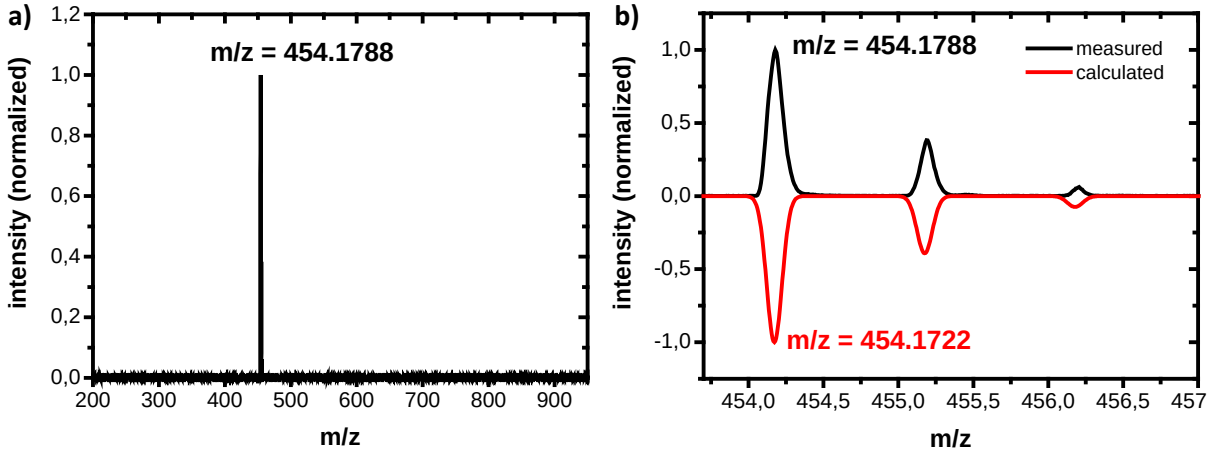

Figure S23 | a) HR-MALDI-TOF spectrum of **4**; b) HR-MALDI-TOF magnified spectrum of **4** (black line) is in agreement to the expected isotopic distribution pattern (red line).

17. NMR spectra of chemical compounds

When we enlarge the spectra of the ^{1}H-NMR and ^{13}C-NMR of compound **3** at room temperature, there are two peaks of the methyl groups, as a result of the restricted rotation of the phenyl group (Supplementary Figure 37). At 80°C the spectrum shows one average signal (Supplementary Figure 38). The same effects were observed for compounds **S3** and **S4**.

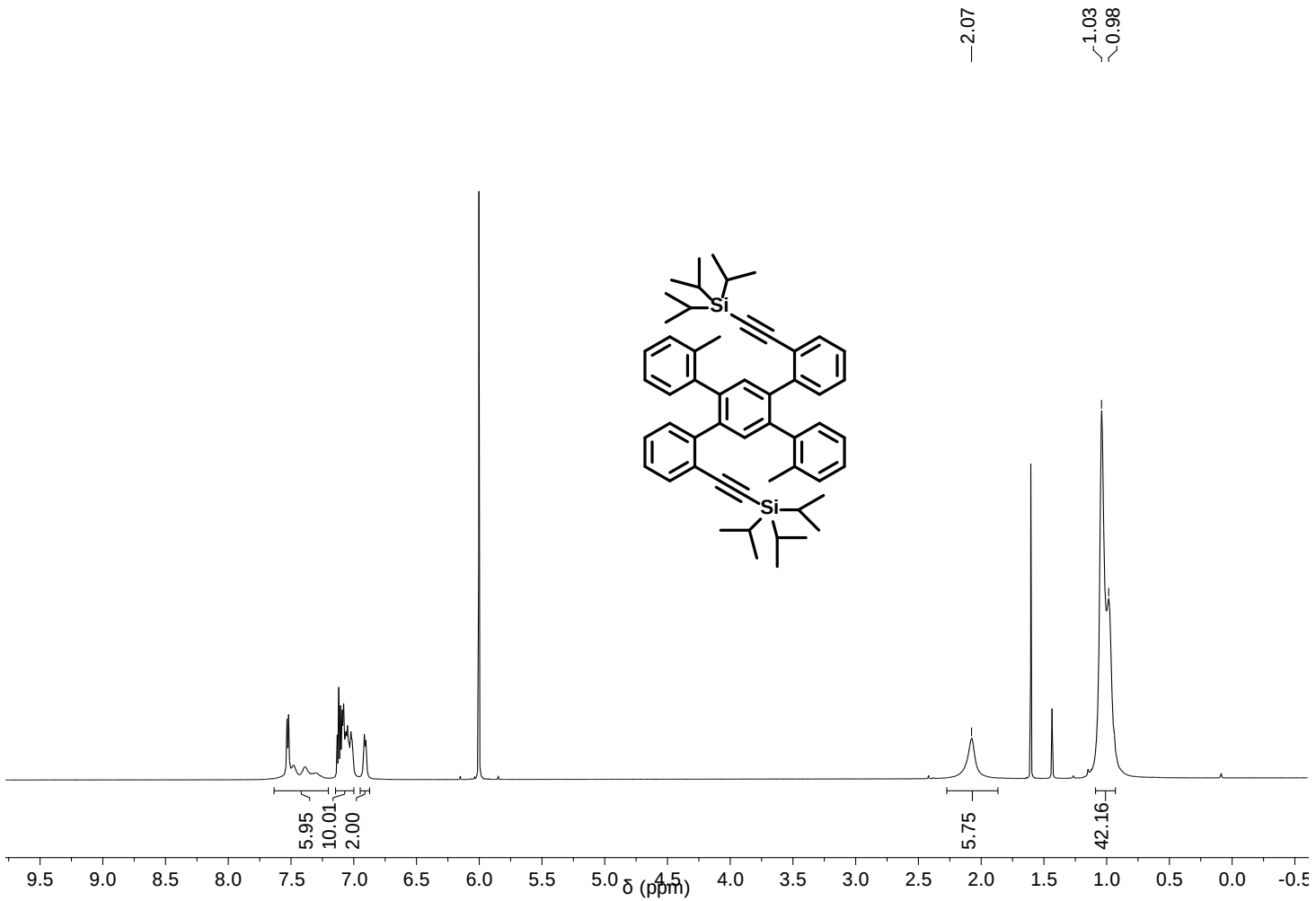

Figure S24: ^{1}H-NMR spectrum of **S3** dissolved in tetrachloroethane-d_2, 600 MHz, 296 K.

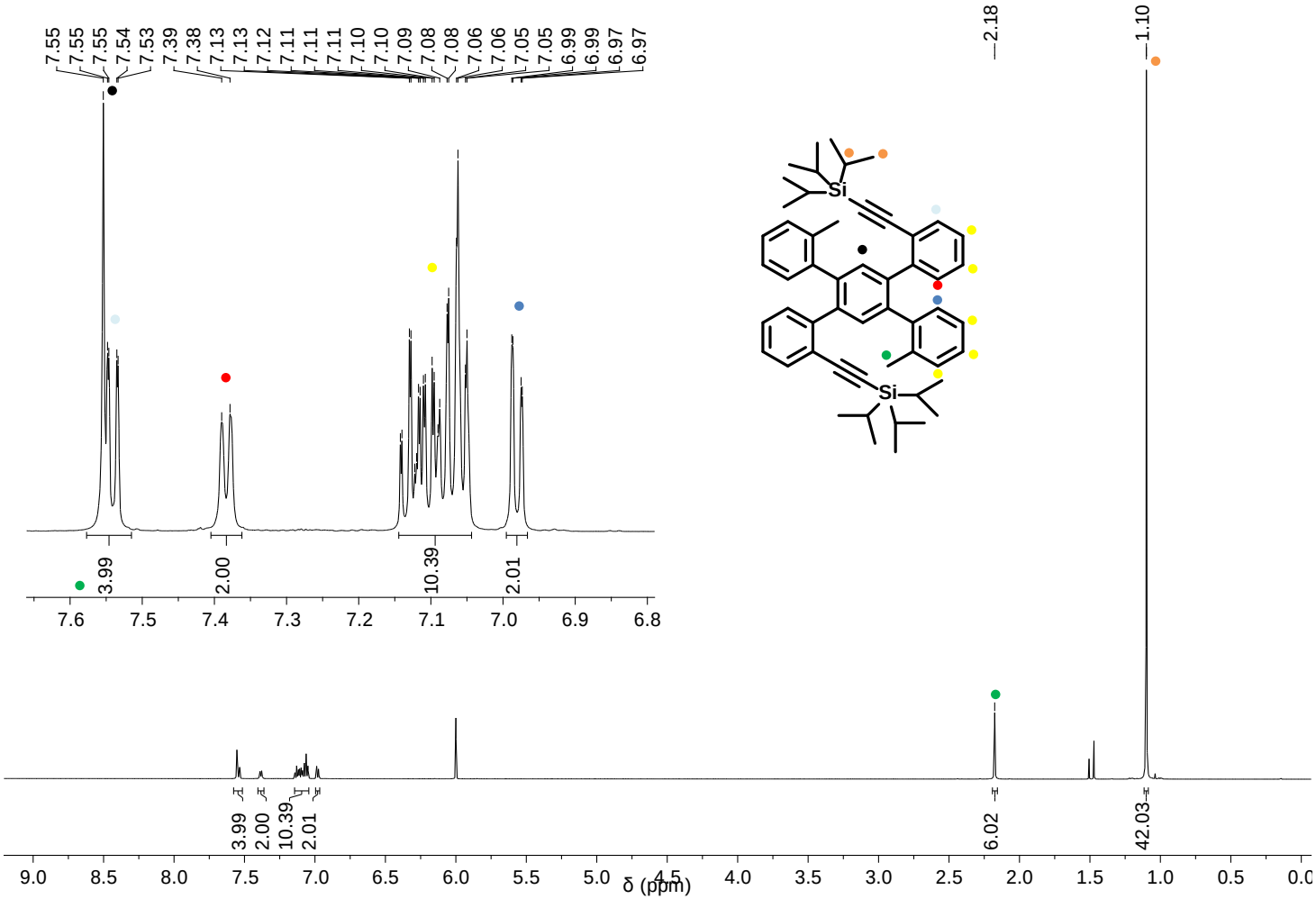

Figure S25: ^{1}H-NMR spectrum of **S3** dissolved in tetrachloroethane-d_2, 600 MHz, 363 K.

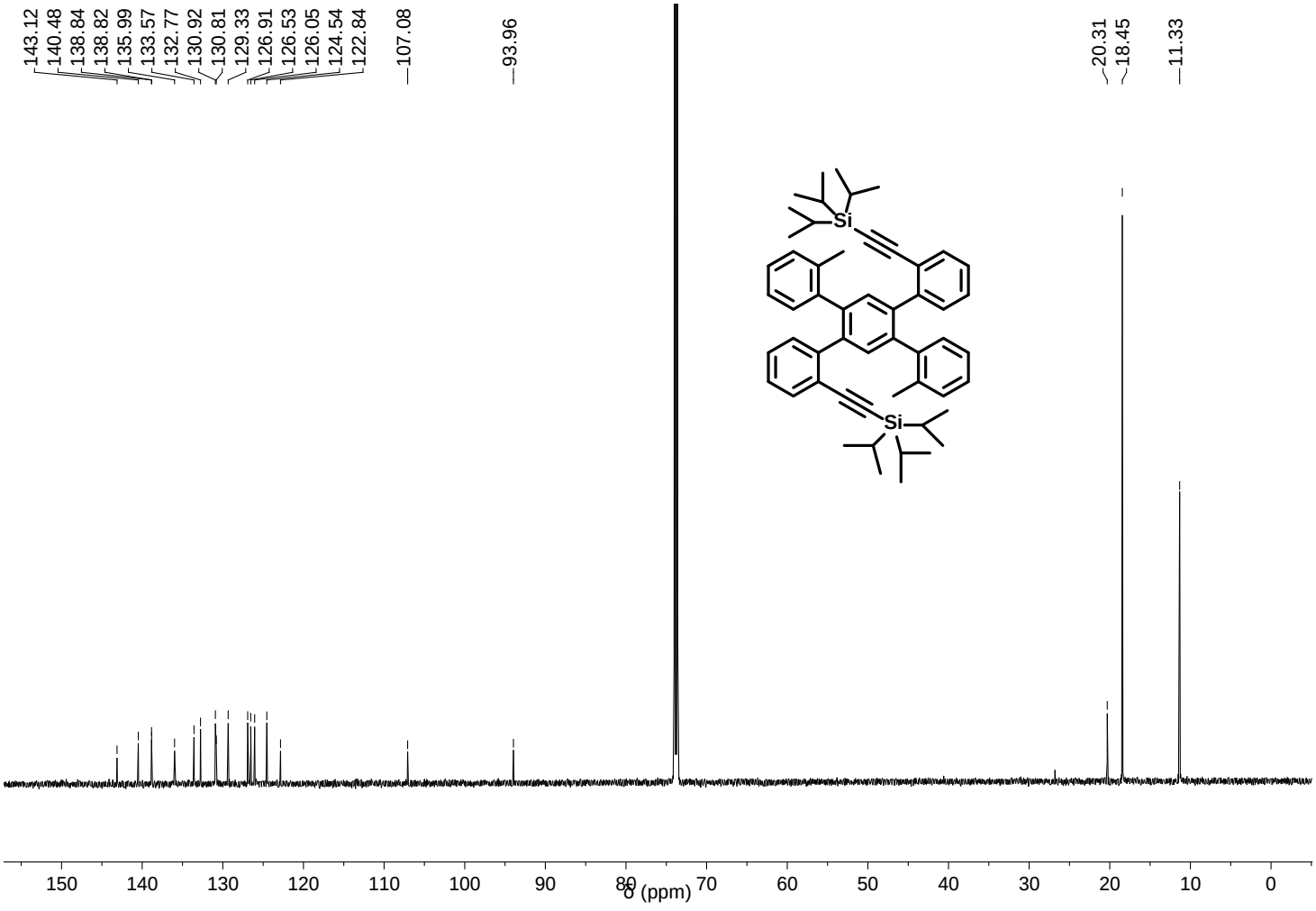

Figure S26: ^{13}C-NMR spectrum of **S3** dissolved in tetrachloroethane-d_2, 150 MHz, 363 K.

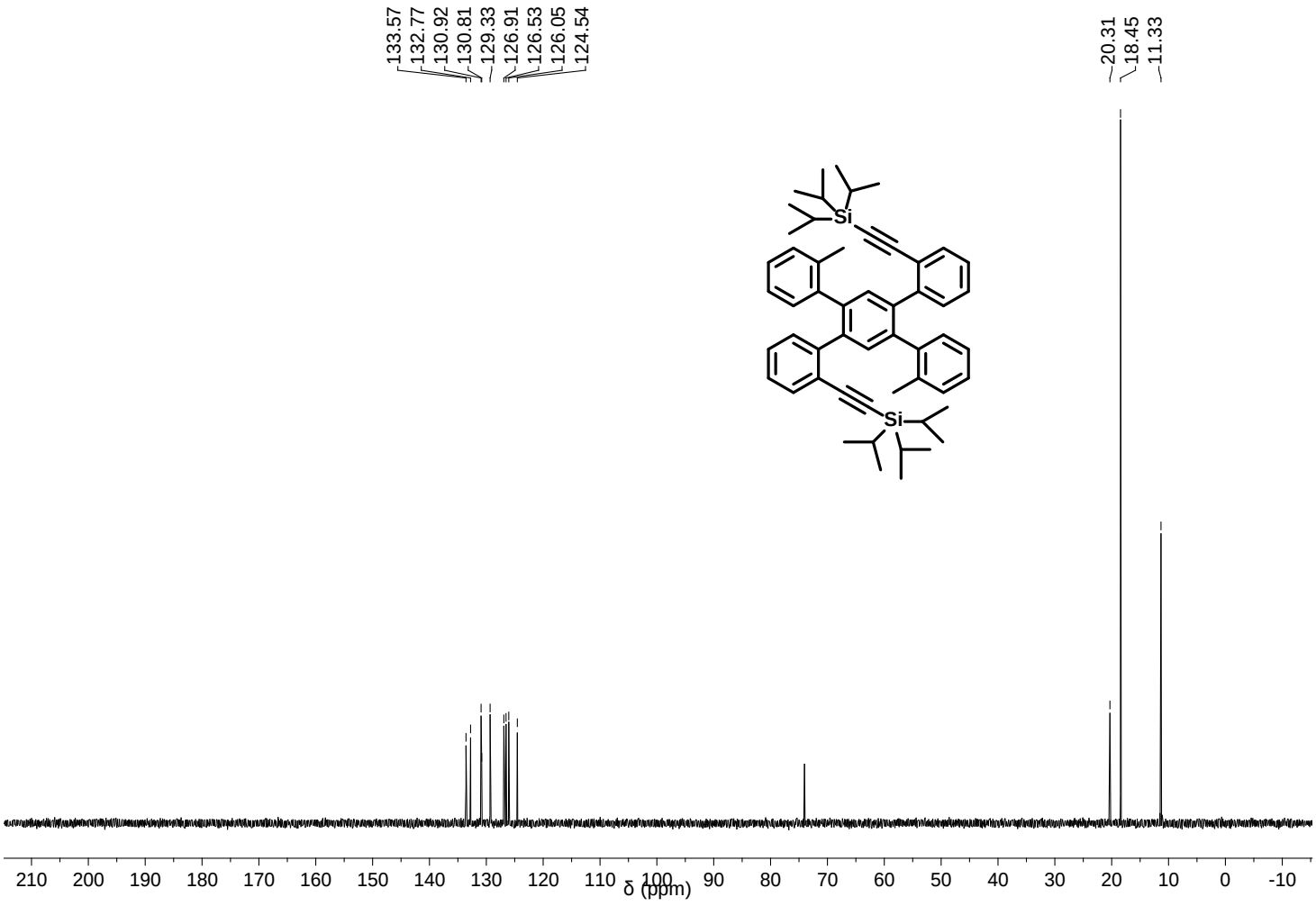

Figure S27: ^{13}C-DEPT135-NMR spectrum of **S3** dissolved in tetrachloroethane-d_2, 150 MHz, 363 K.

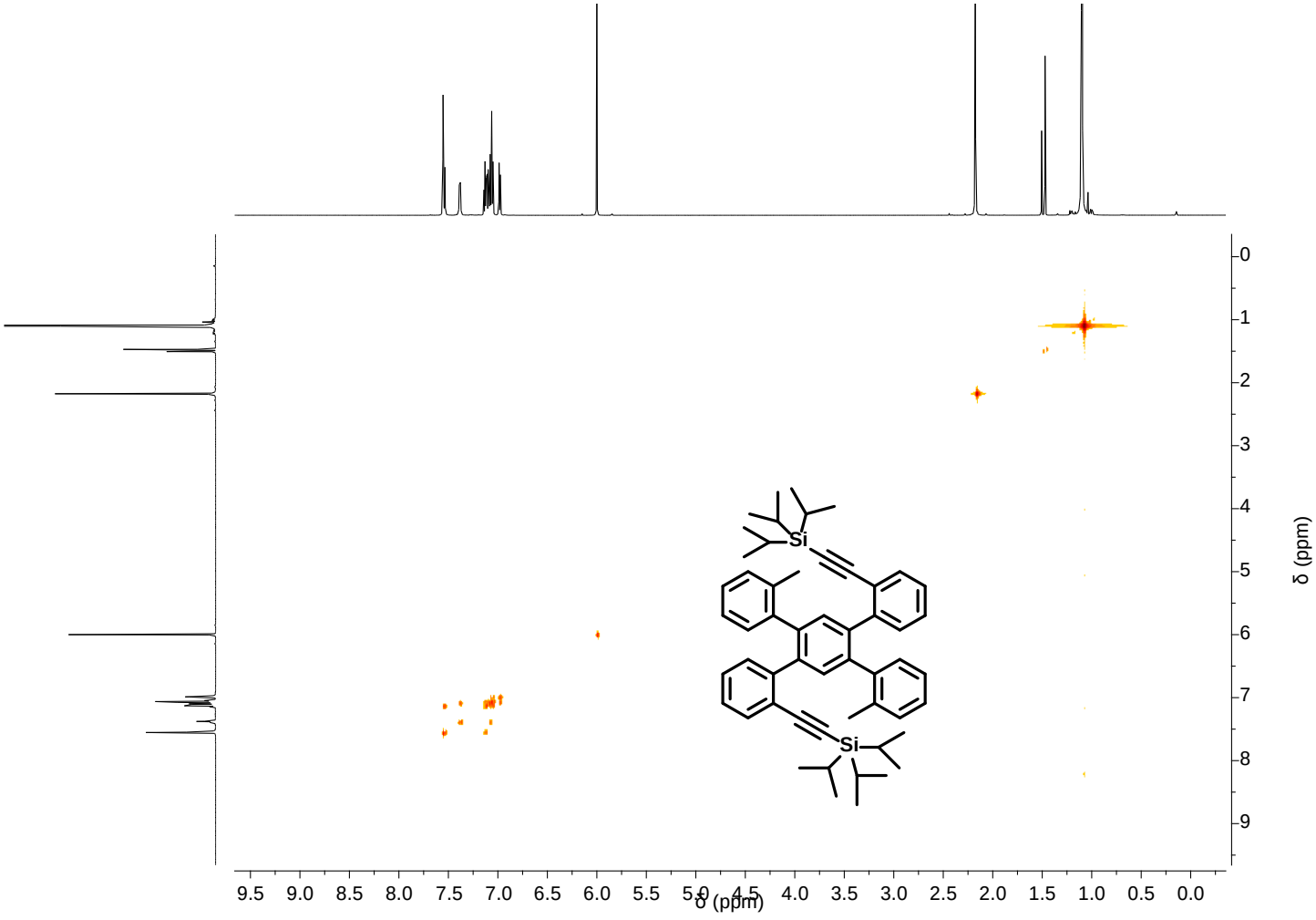

Figure S28: $^{1}H/^{1}H$-COSY-NMR spectrum of **S3** dissolved in tetrachloroethane-d_2, 600 MHz, 363 K.

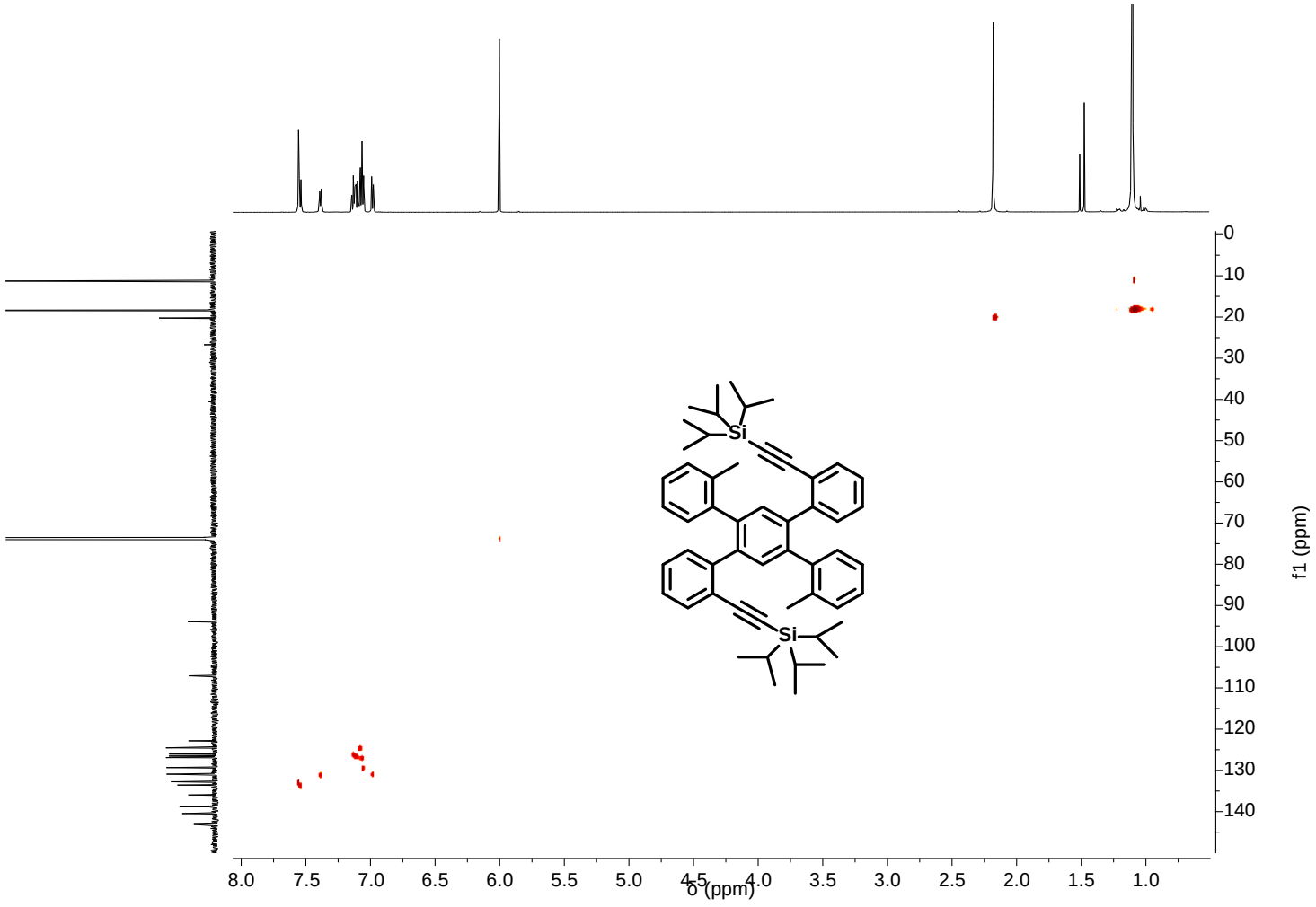

Figure S29: HSQC-NMR spectrum of **S3** dissolved in tetrachloroethane-d_2, 150 MHz, 363 K.

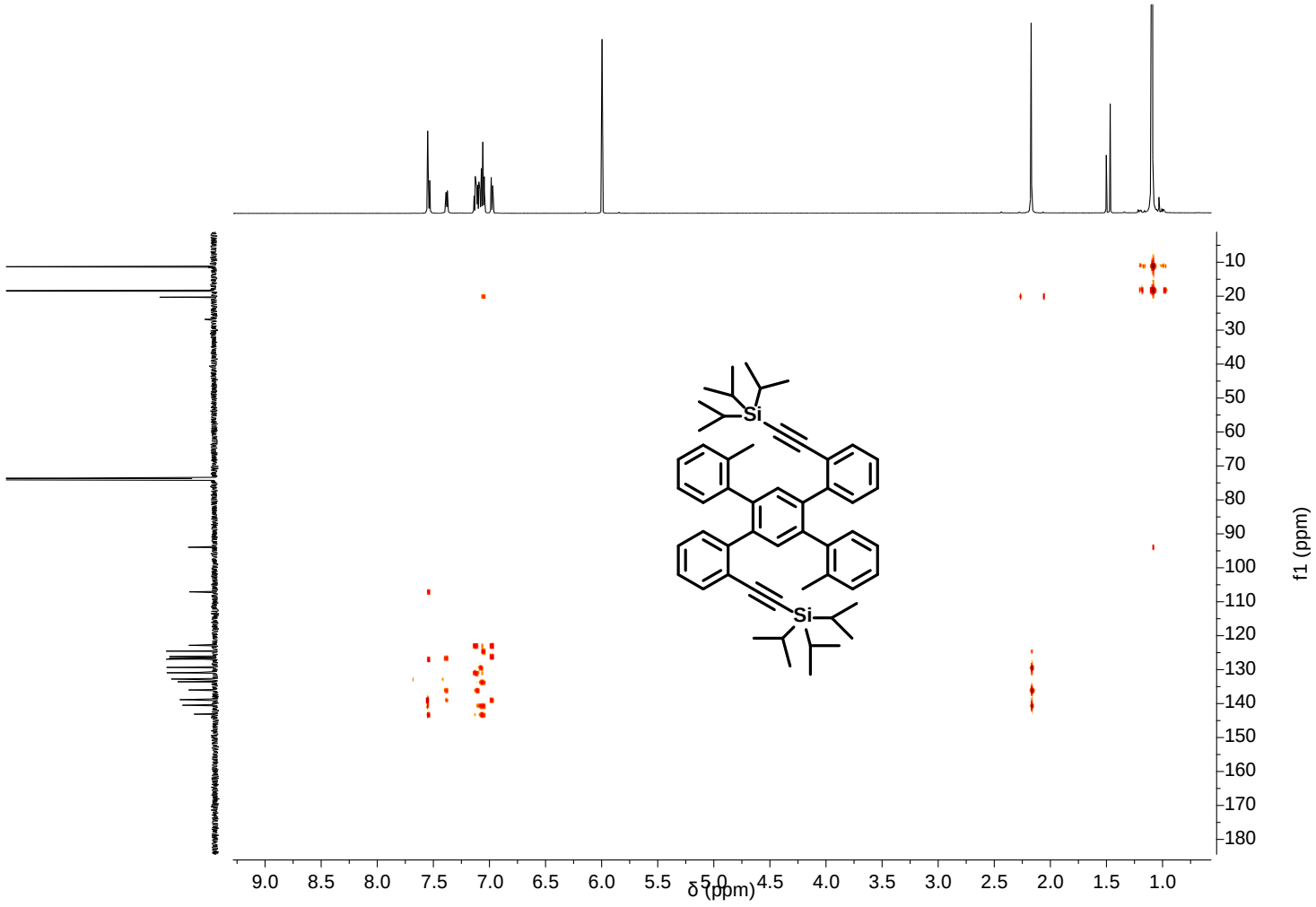

Figure S30: HMBC-NMR spectrum of **S3** dissolved in tetrachloroethane-d_2, 150 MHz, 363 K.

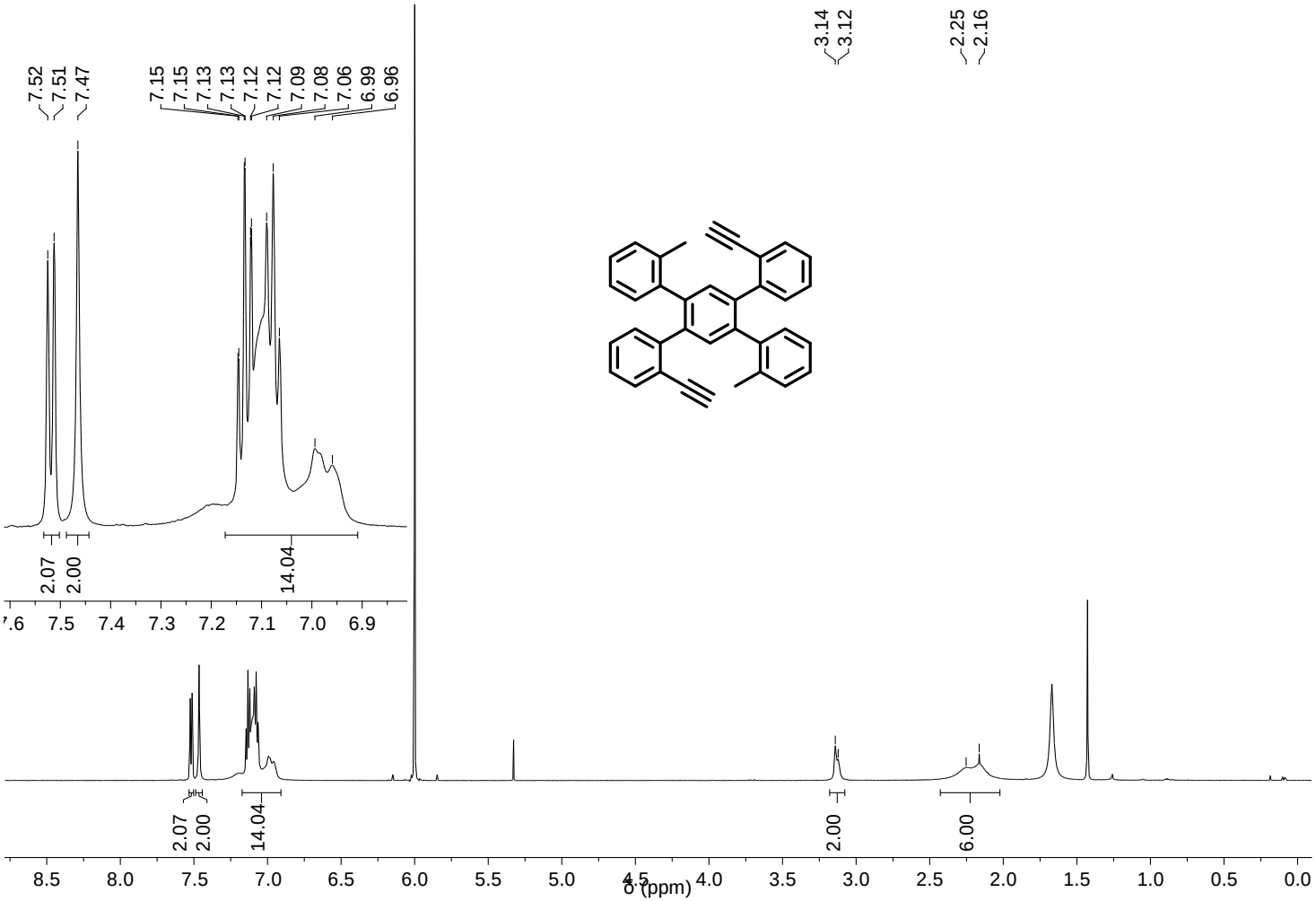

Figure S31: ^{1}H-NMR spectrum of **S4** dissolved in tetrachloroethane-d_2, 600 MHz, 296 K.

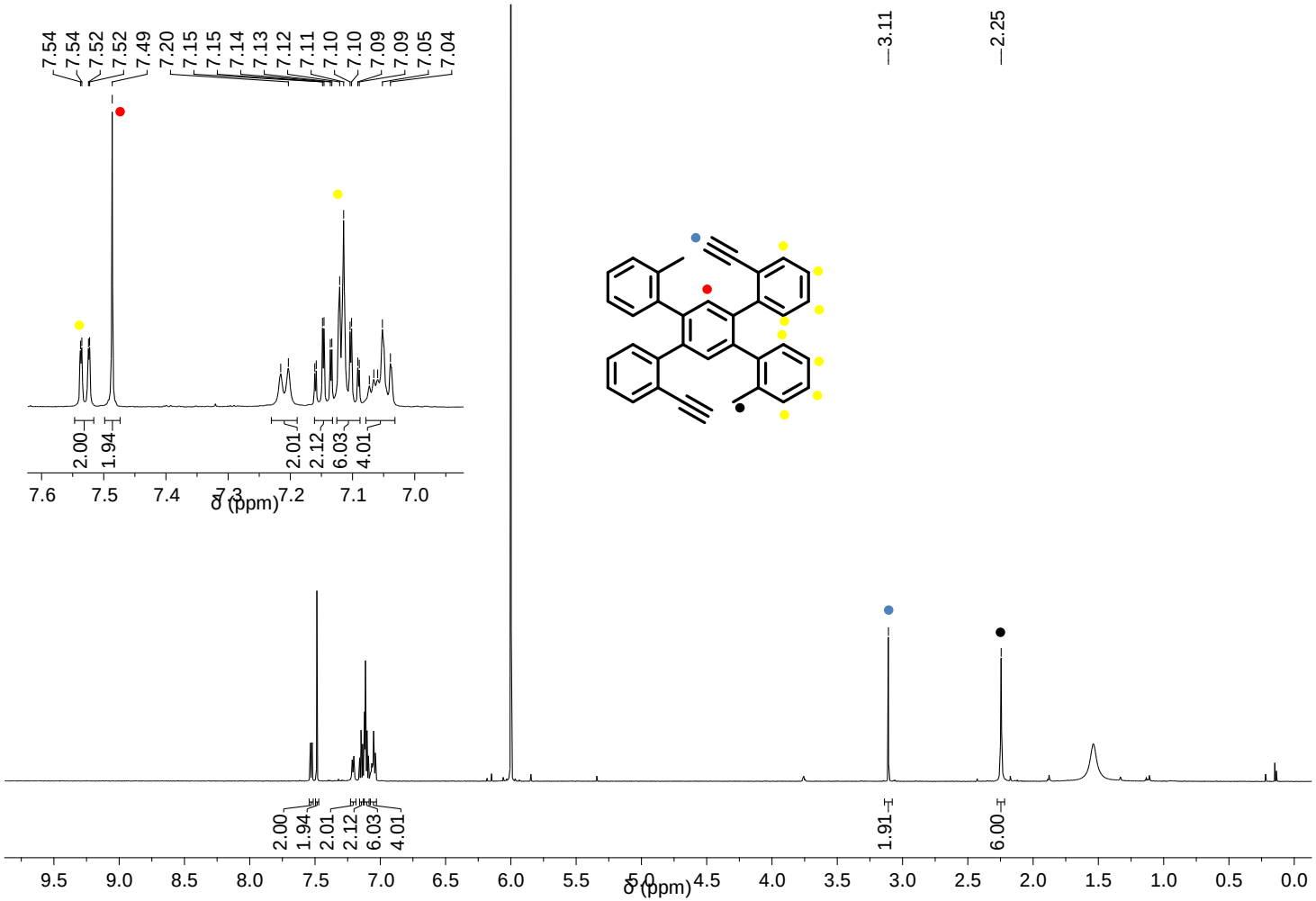

Figure S32: ^{1}H-NMR spectrum of **S4** dissolved in tetrachloroethane-d_2, 600 MHz, 353 K.

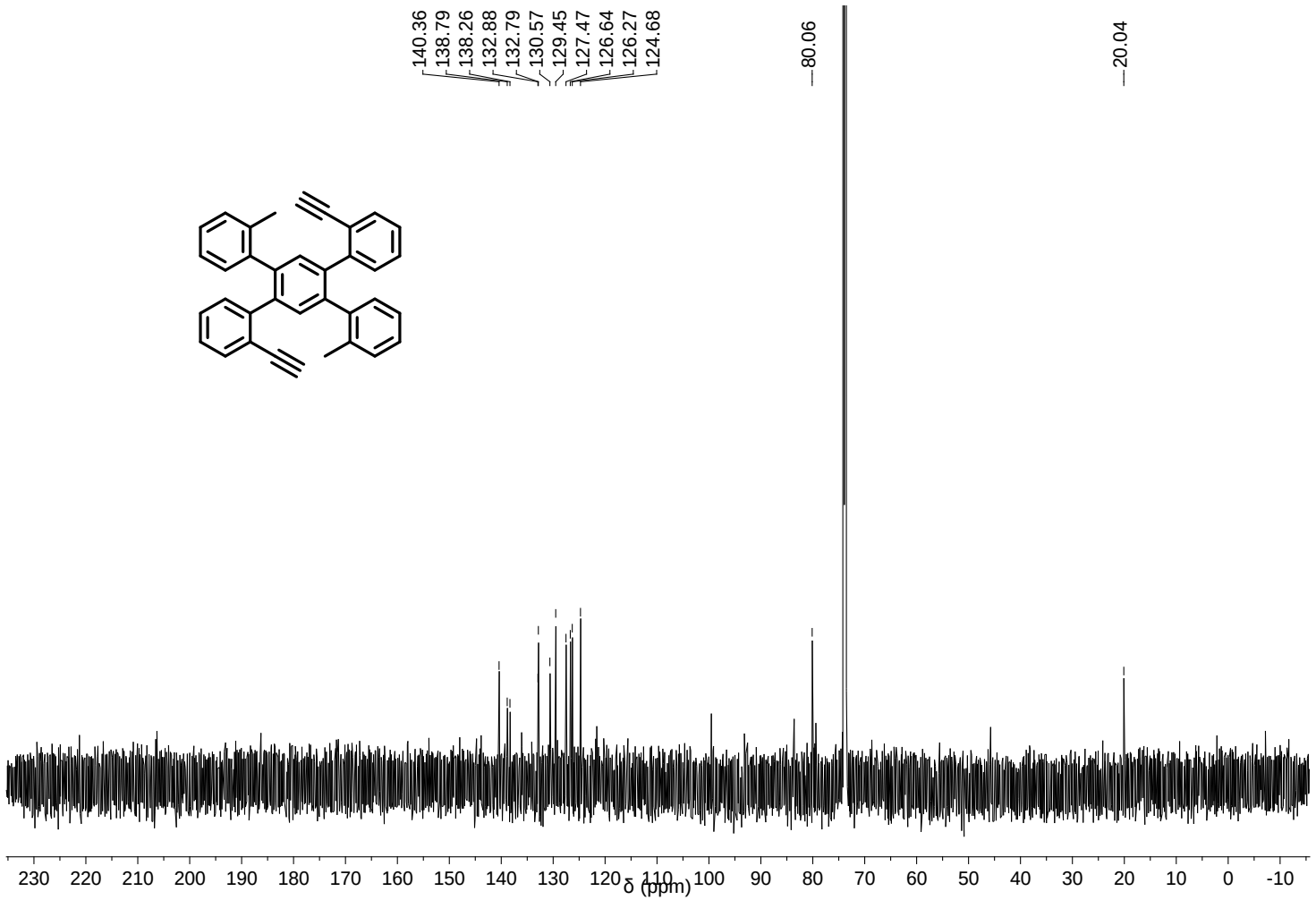

Figure S33: ^{13}C-NMR spectrum of **S4** dissolved in tetrachloroethane-d_2, 150 MHz, 353 K.

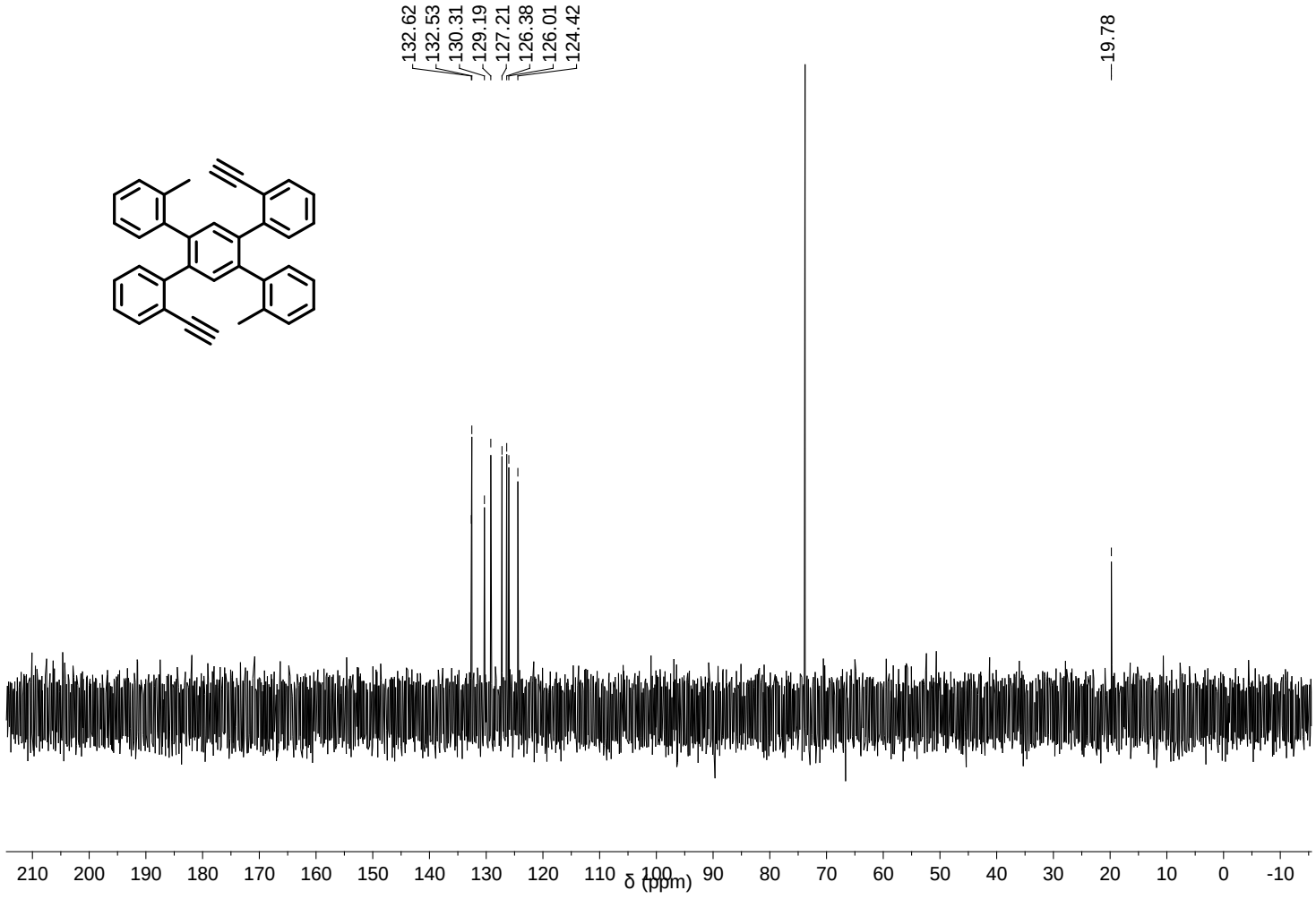

Figure S34: ^{13}C-DEPT135-NMR spectrum of **S4** dissolved in tetrachloroethane-d_2, 150 MHz, 353 K.

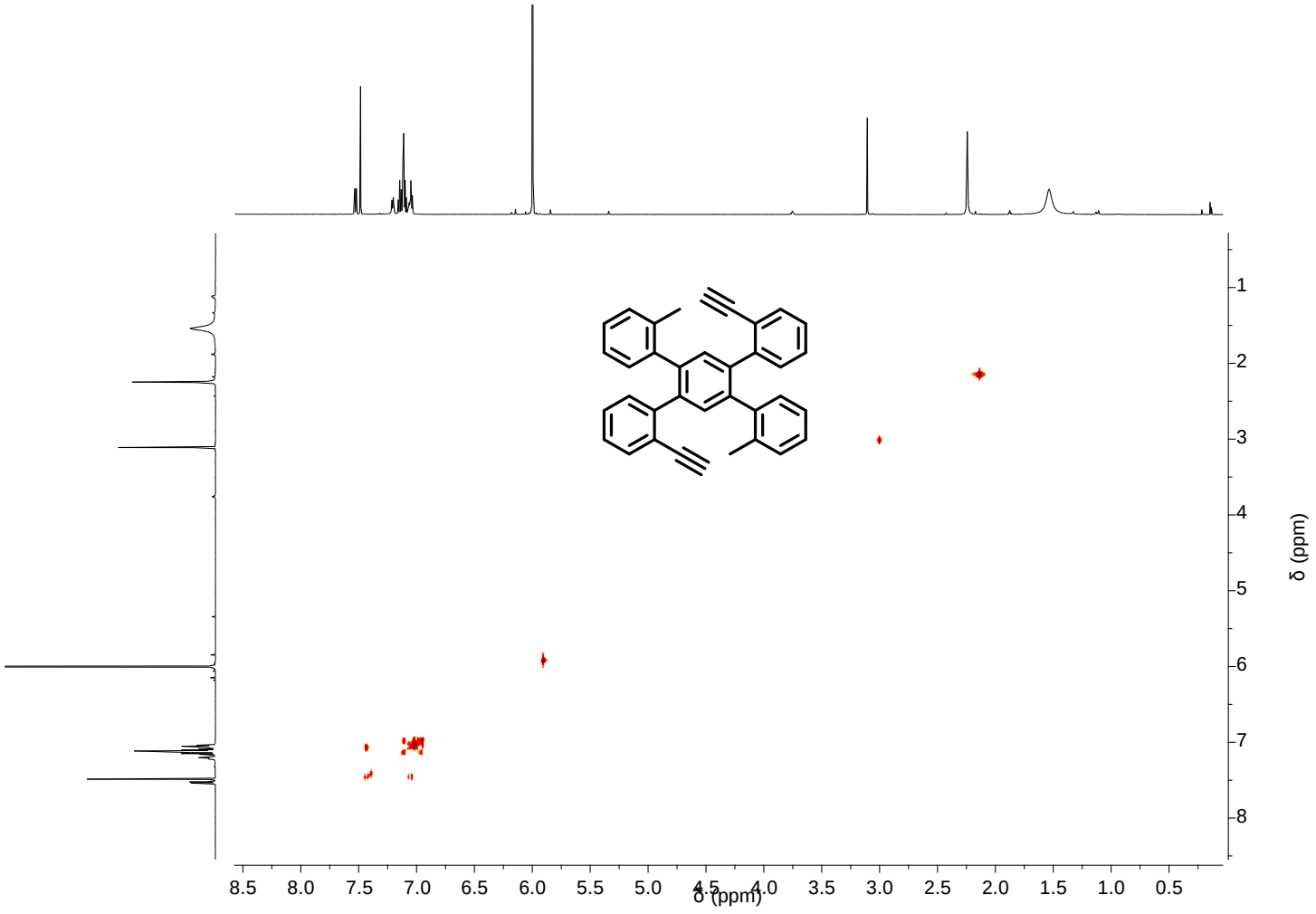

Figure S35: $^{1}H/^{1}H$-COSY-NMR spectrum of **S4** dissolved in tetrachloroethane-d_2, 600 MHz, 353 K.

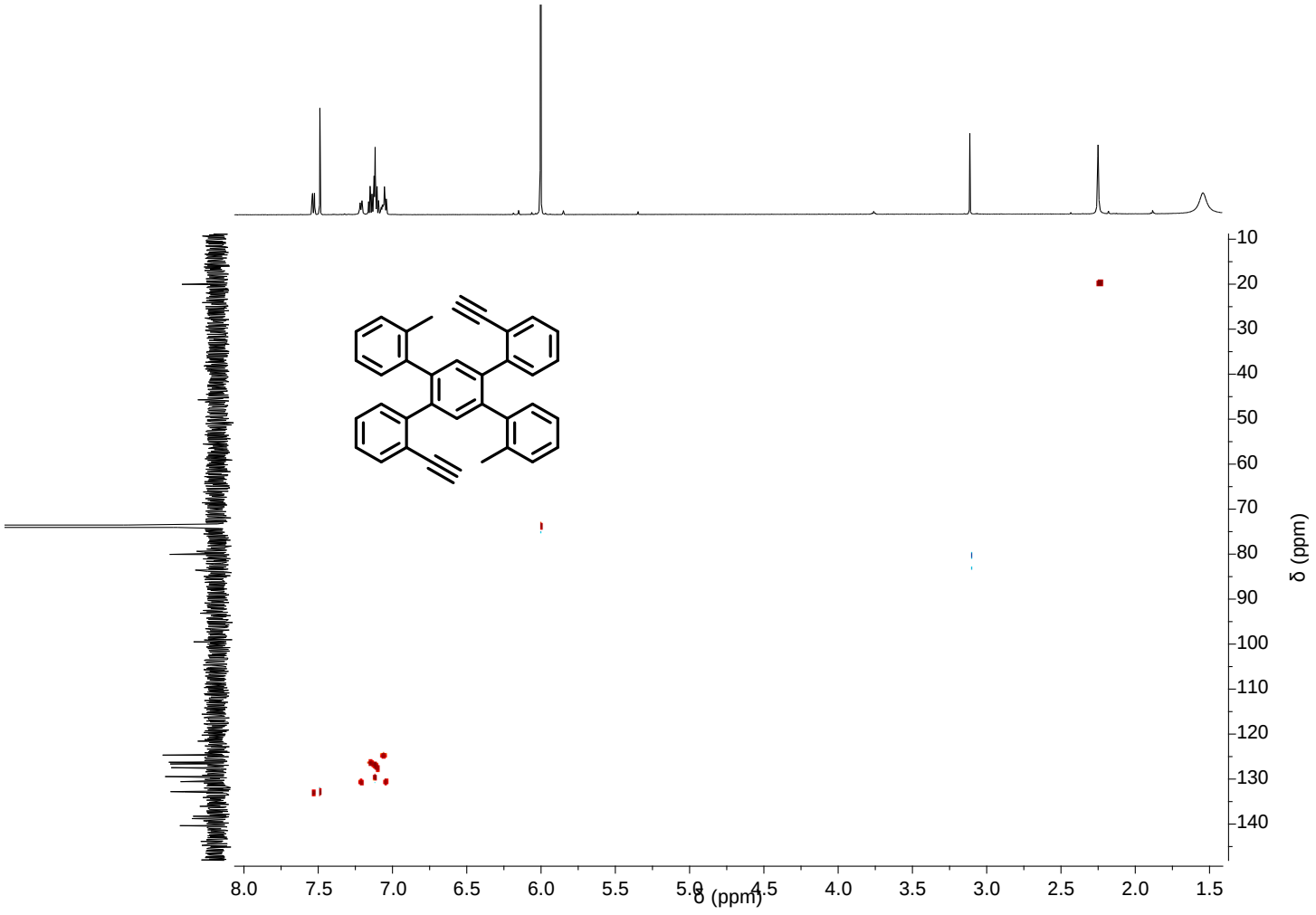

Figure S36: HSQC-NMR spectrum of **S4** dissolved in tetrachloroethane-d_2, 150 MHz, 353 K.

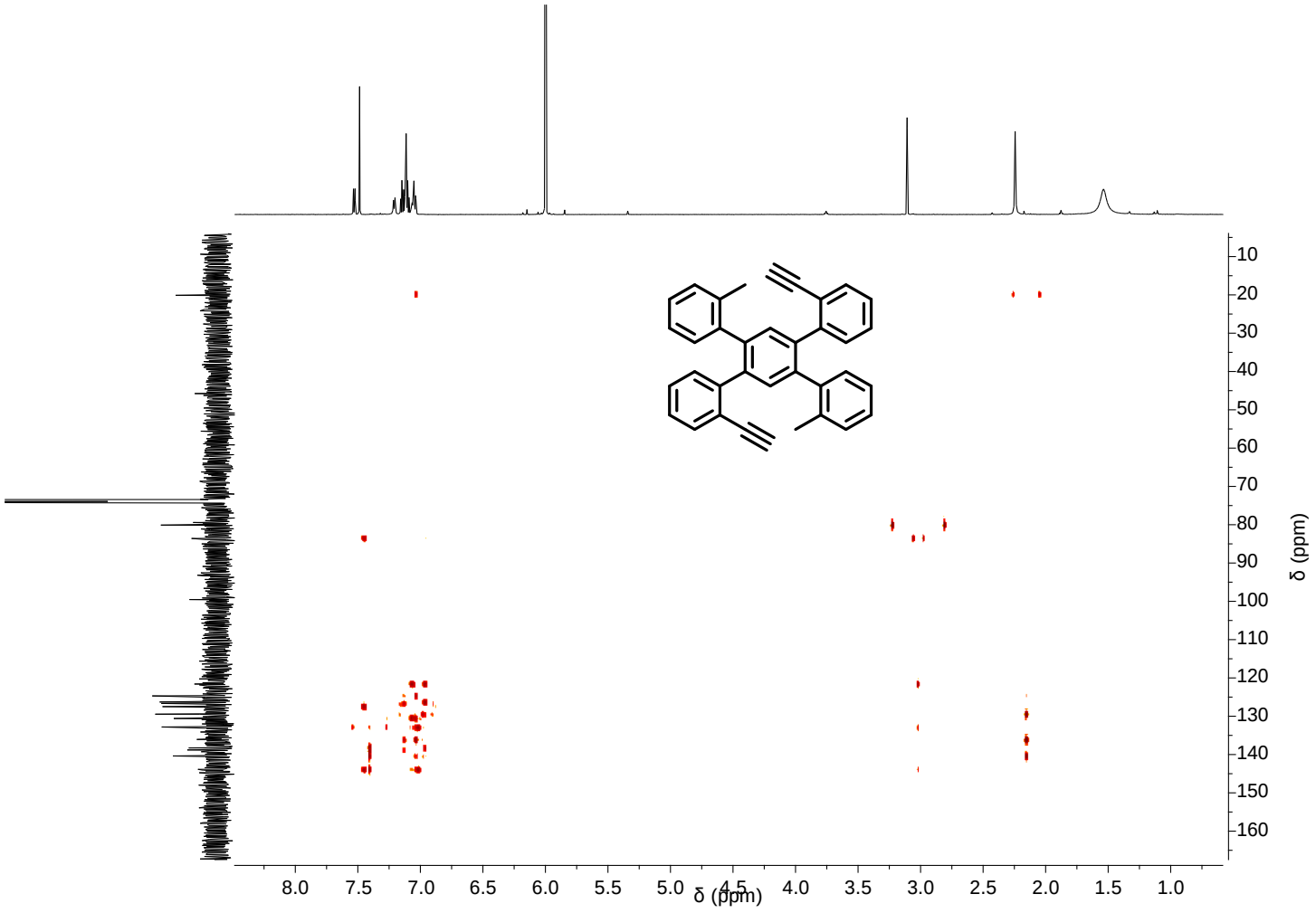

Figure S37: HMBC-NMR spectrum of **S4** dissolved in tetrachloroethane-d_2, 150 MHz, 353 K.

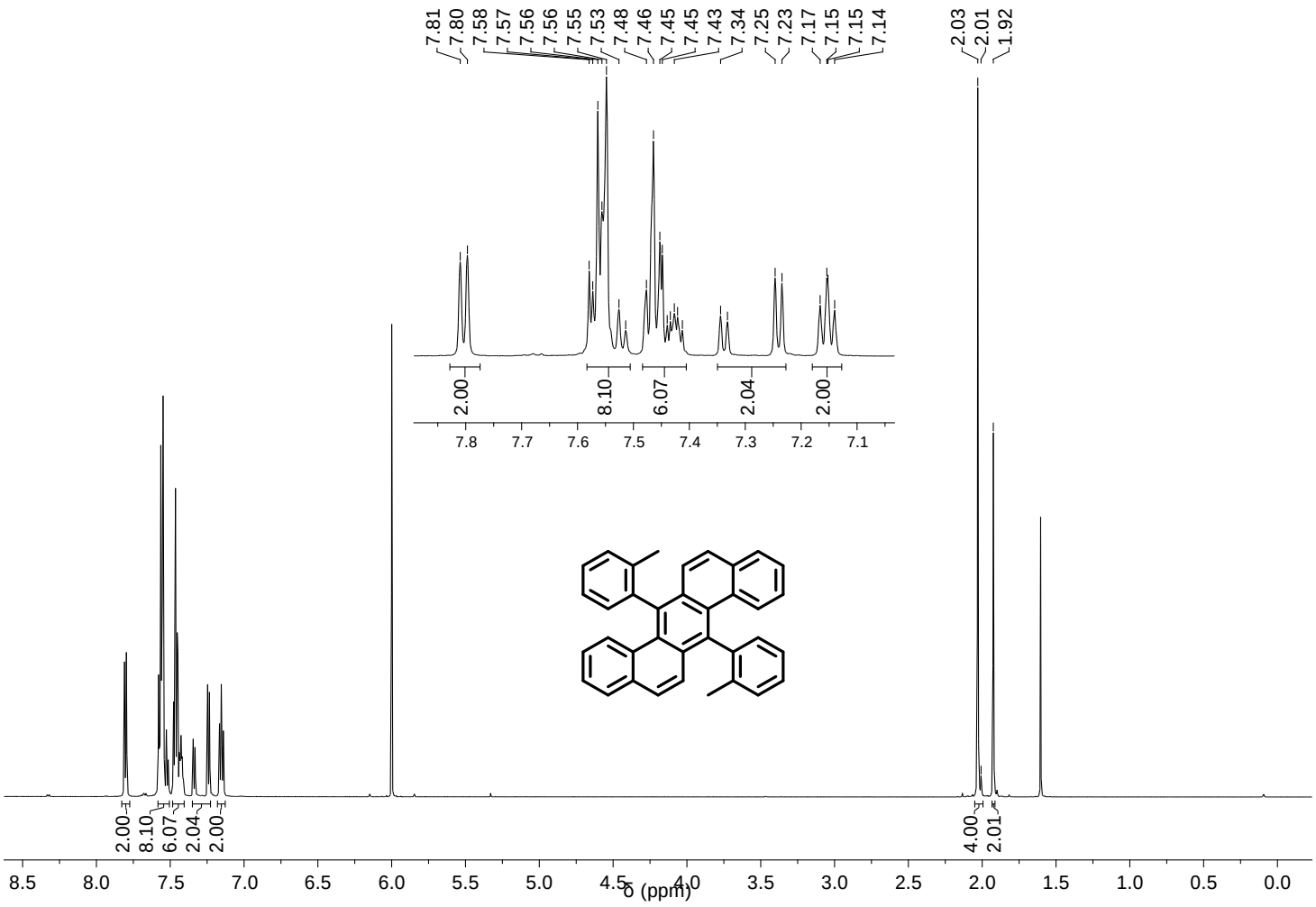

Figure S38: ^{1}H-NMR spectrum of **3** dissolved in tetrachloroethane-d_2, 600 MHz, 296 K.

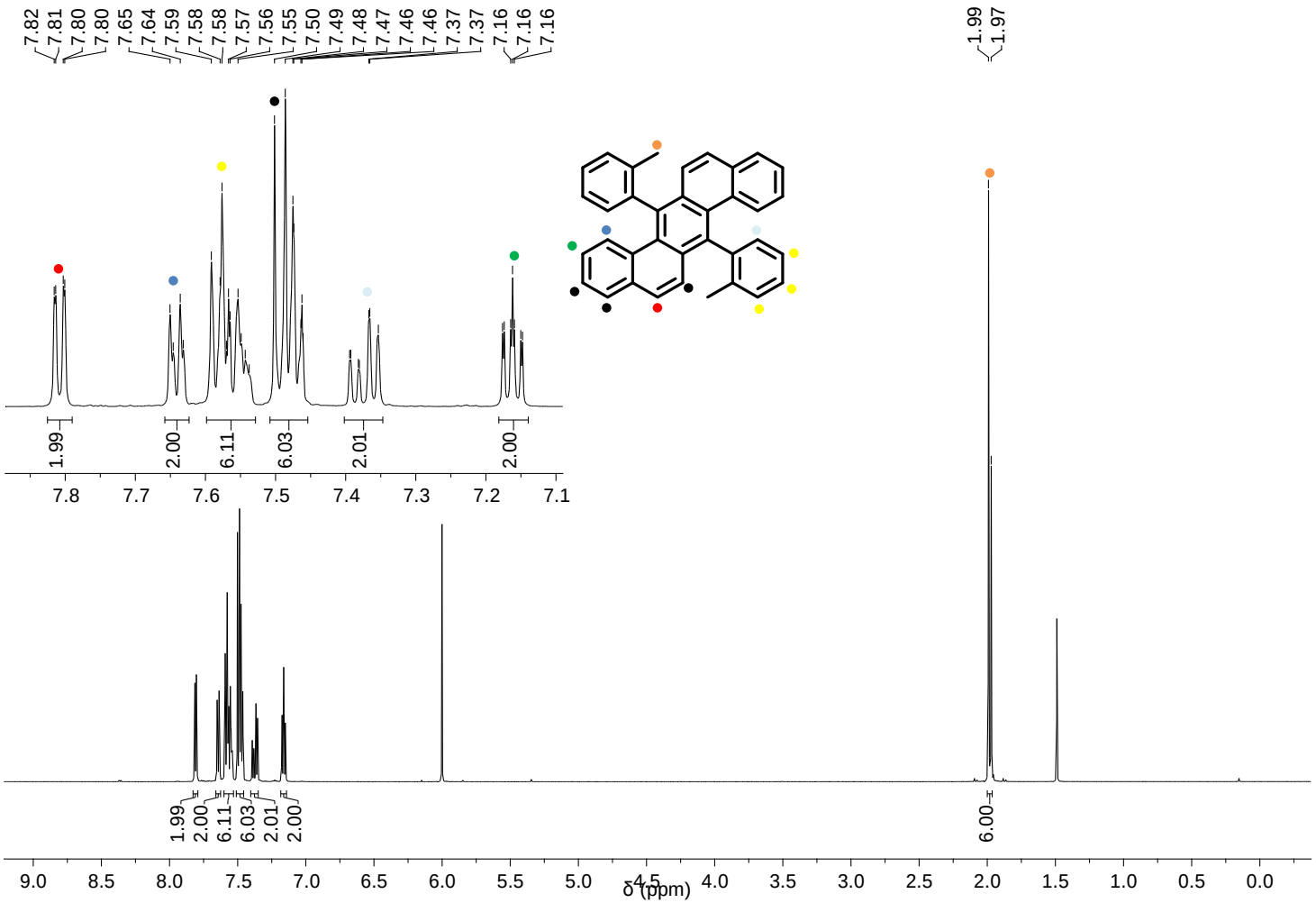

Figure S39: ^{1}H-NMR spectrum of **3** dissolved in tetrachloroethane-d_2, 600 MHz, 353 K.

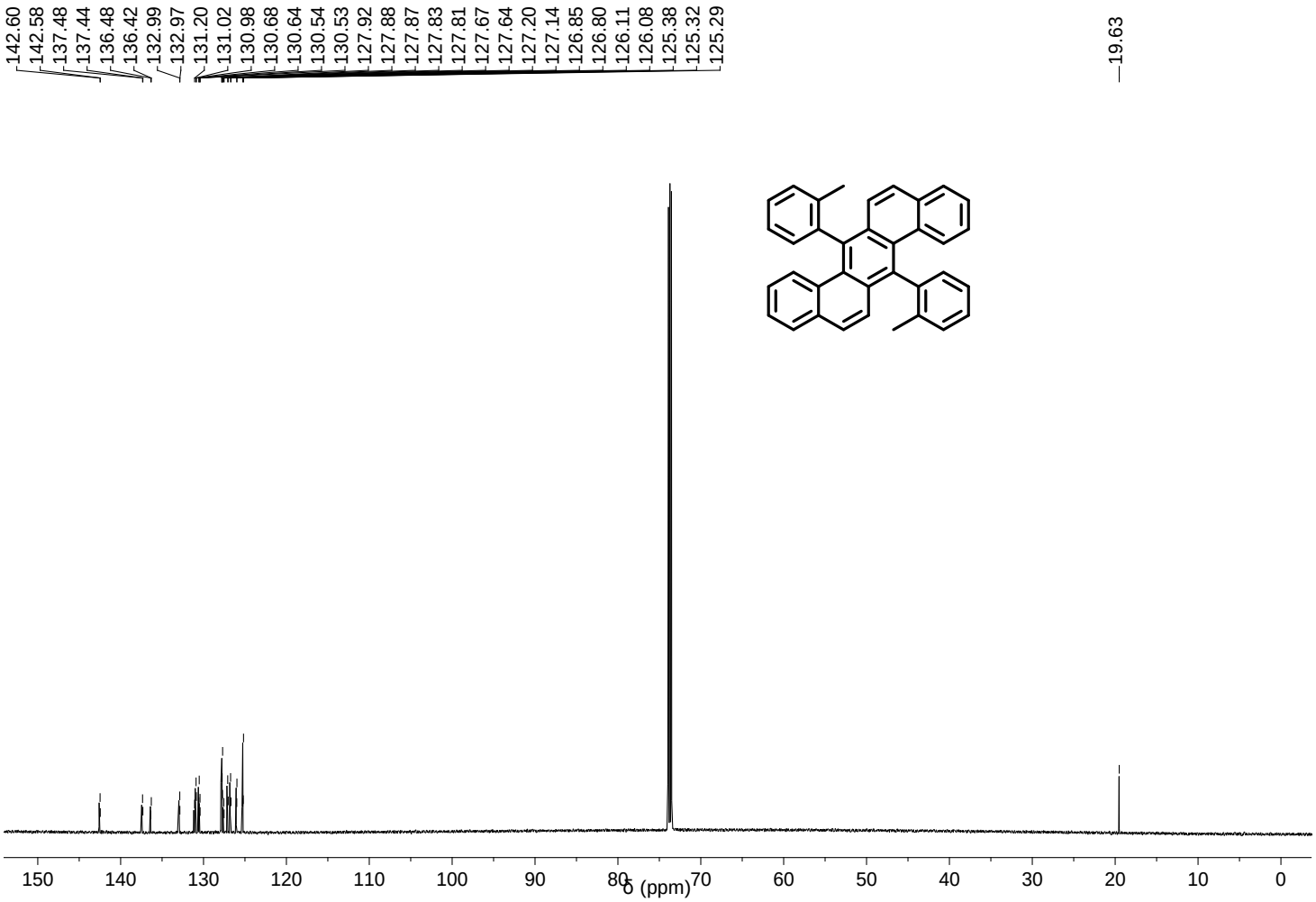

Figure S40: ^{13}C-NMR spectrum of **3** dissolved in tetrachloroethane-d_2, 150 MHz, 353 K.

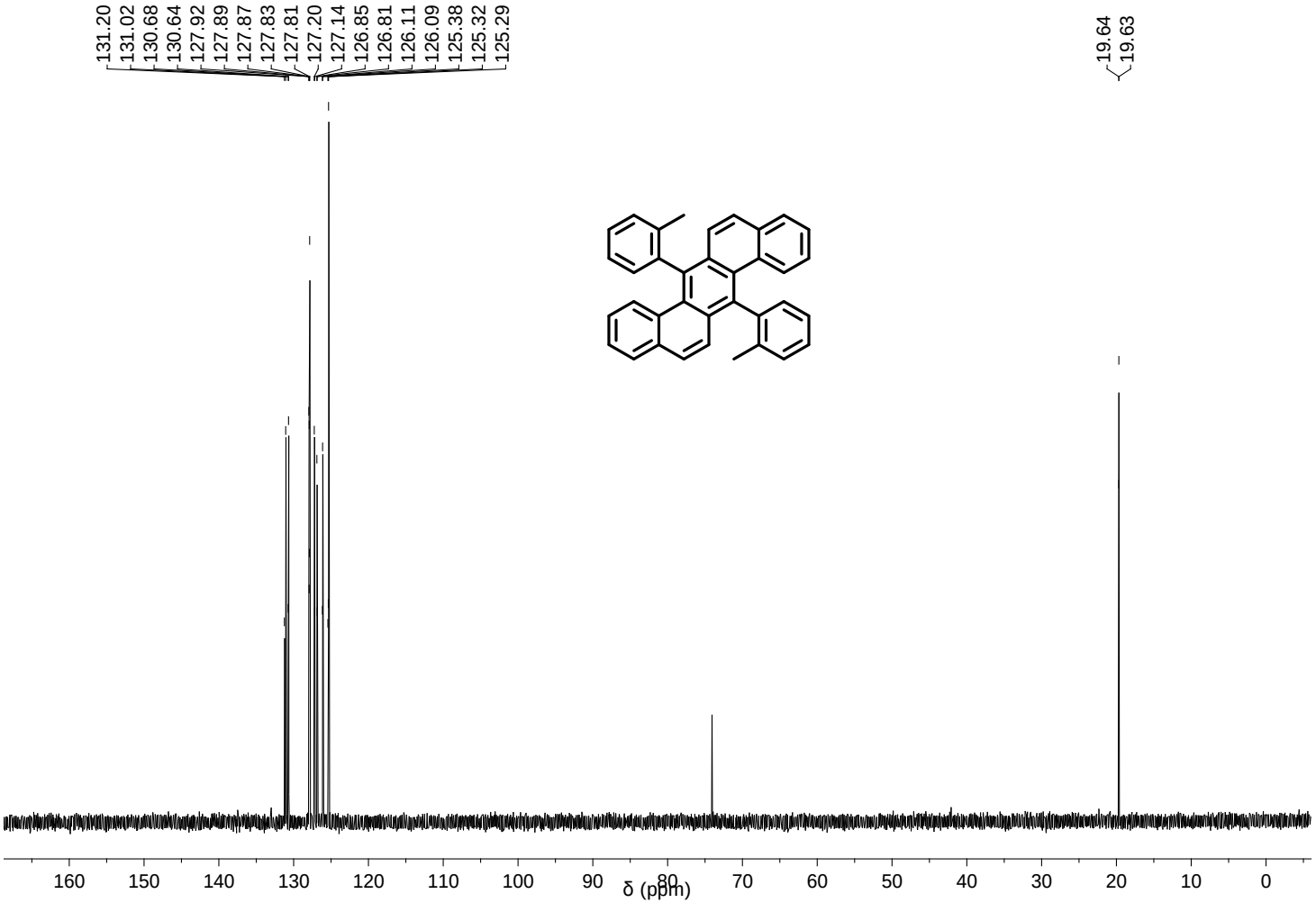

Figure S41: ^{13}C-DEPT135-NMR spectrum of **3** dissolved in tetrachloroethane-d_2, 150 MHz, 353 K.

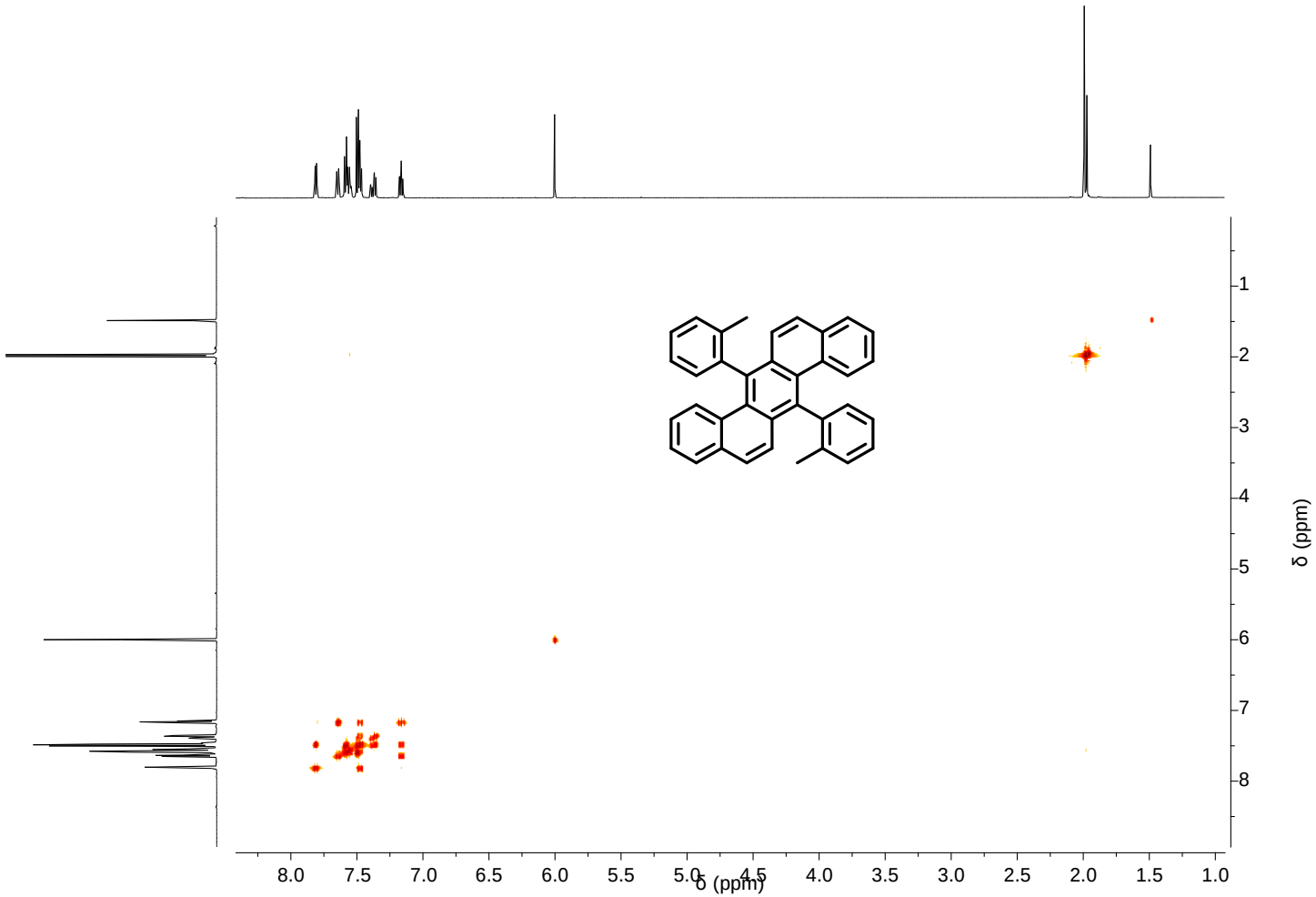

Figure S42: $^{1}H/^{1}H$-COSY-NMR spectrum of **3** dissolved in tetrachloroethane-d_2, 600 MHz, 353 K.

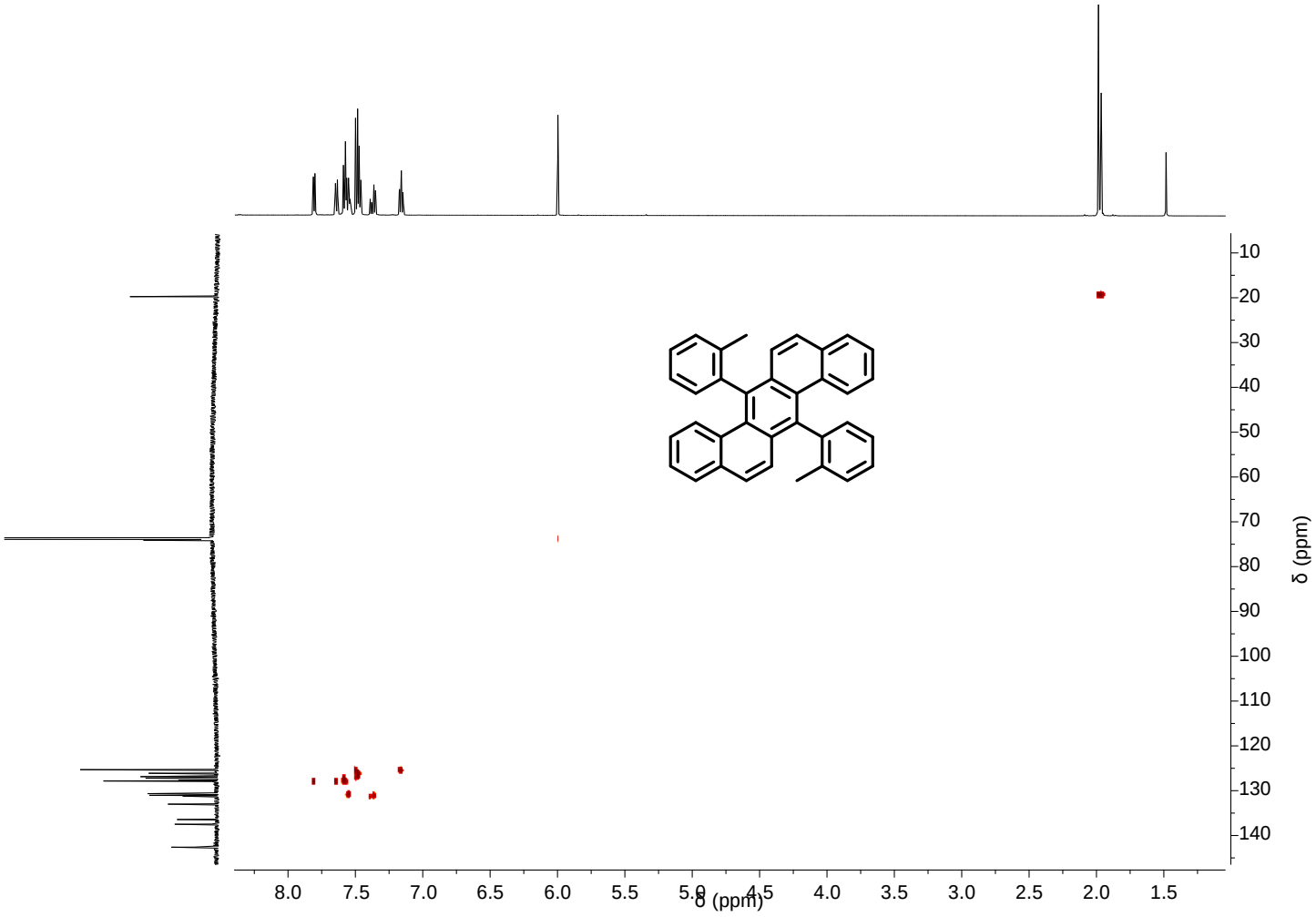

Figure S43: HSQC-NMR spectrum of **3** dissolved in tetrachloroethane-d_2, 150 MHz, 353 K.

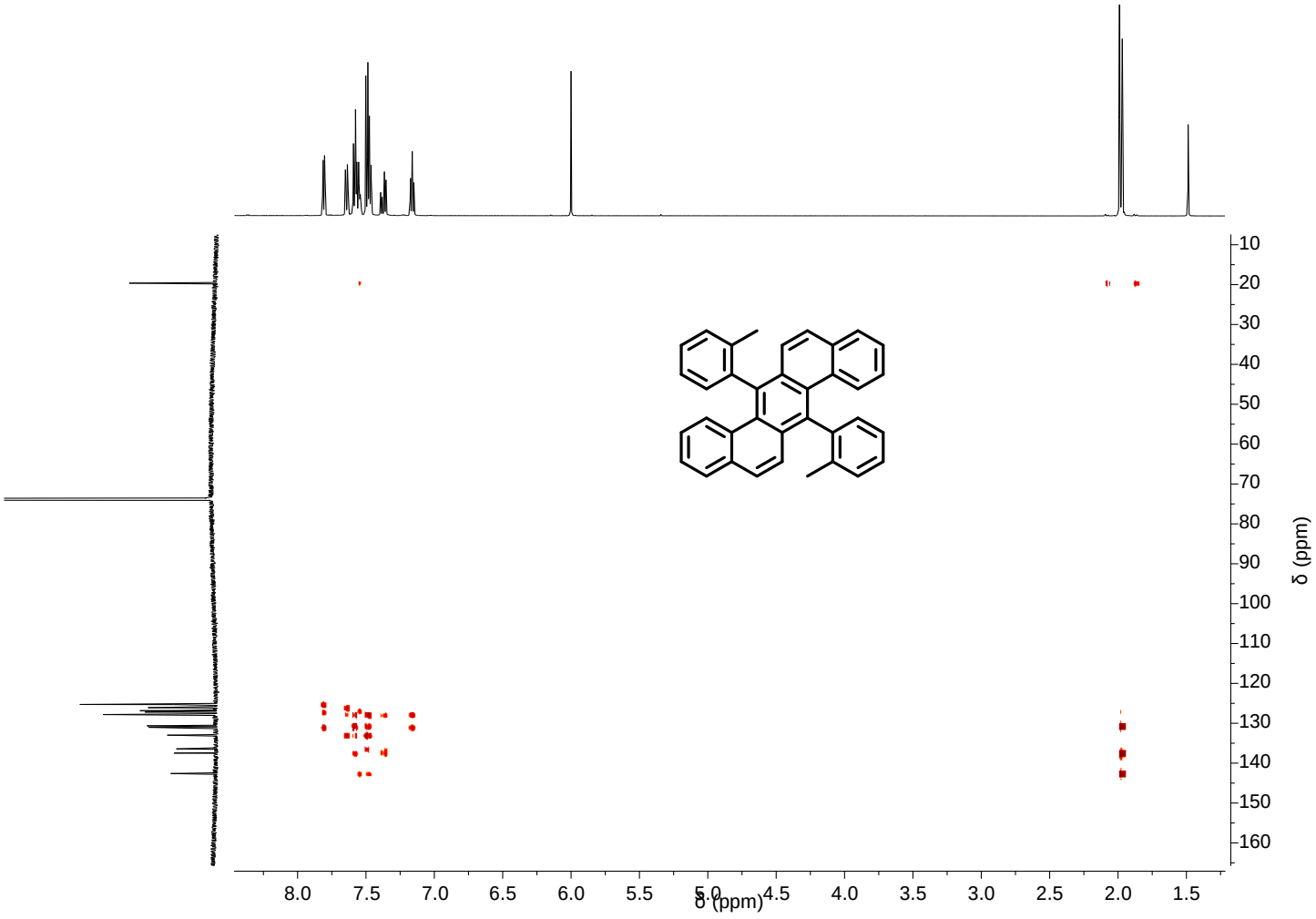

Figure S44: HMBC-NMR spectrum of **3** dissolved in tetrachloroethane-d_2, 150 MHz, 353 K.

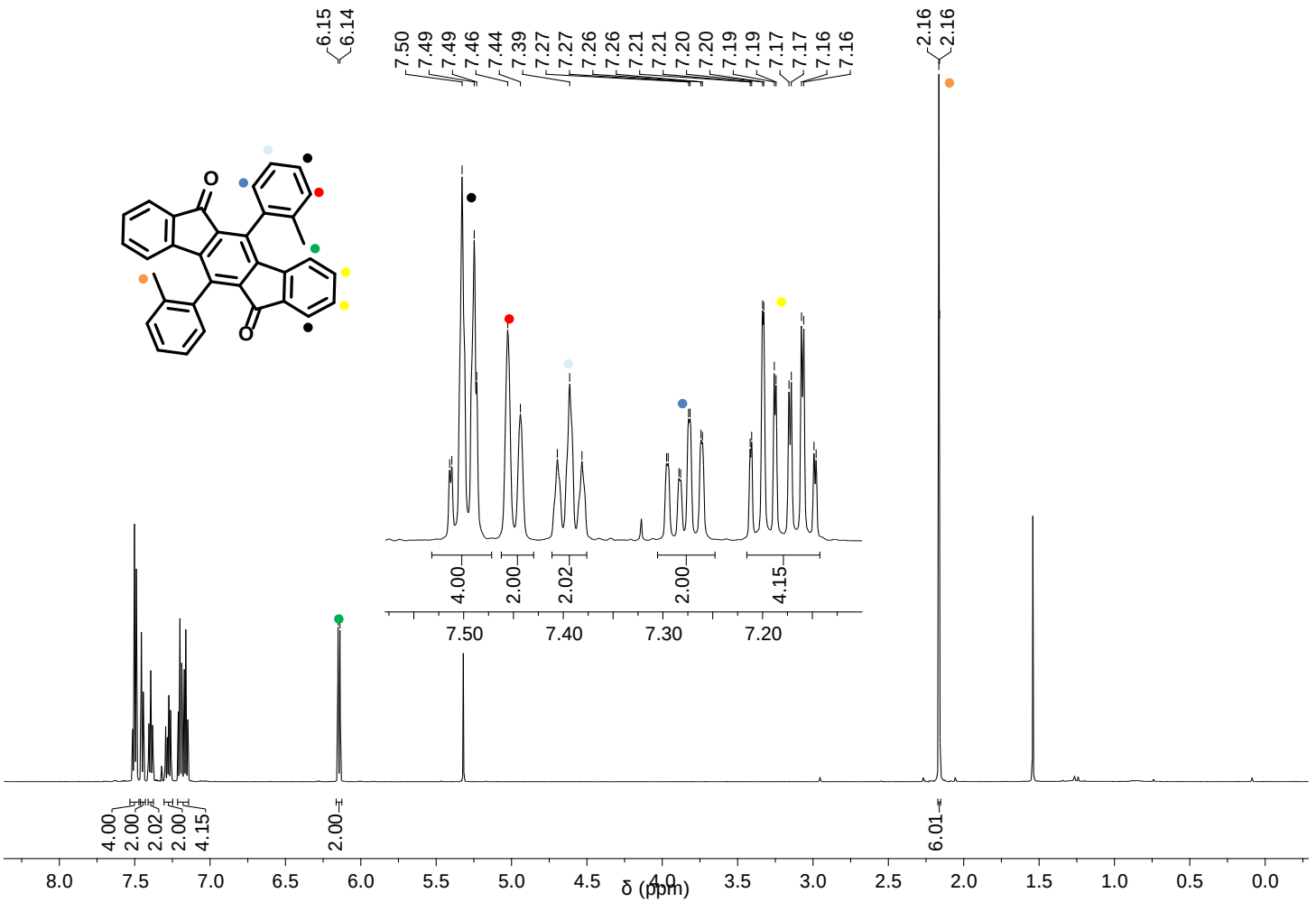

Figure S45: ^{1}H-NMR spectrum of **S6** dissolved in dichloromethane-d_2, 600 MHz, 296 K.

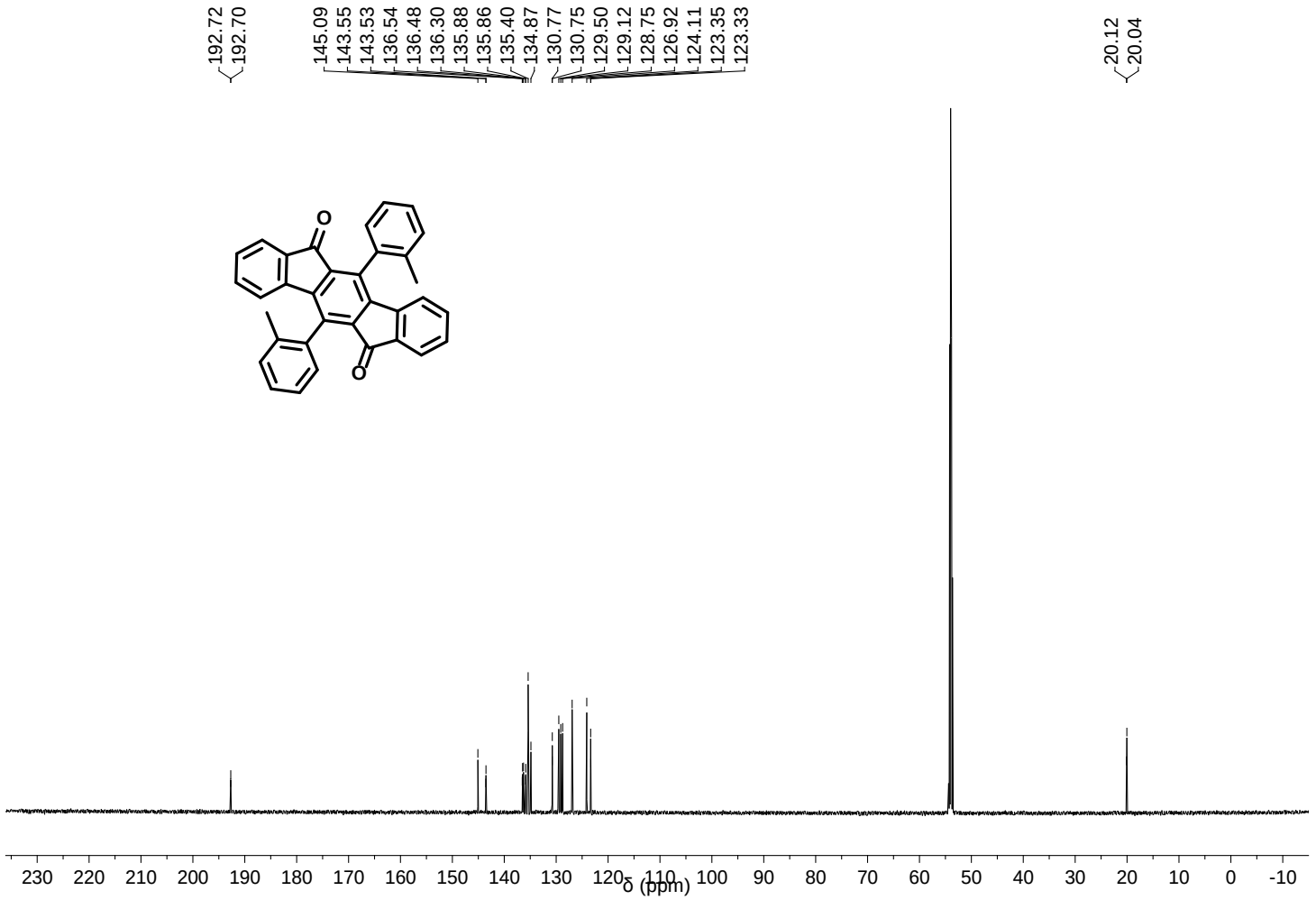

Figure S46: ^{13}C-NMR spectrum of **S6** dissolved in dichloromethane-d_2, 150 MHz, 296 K.

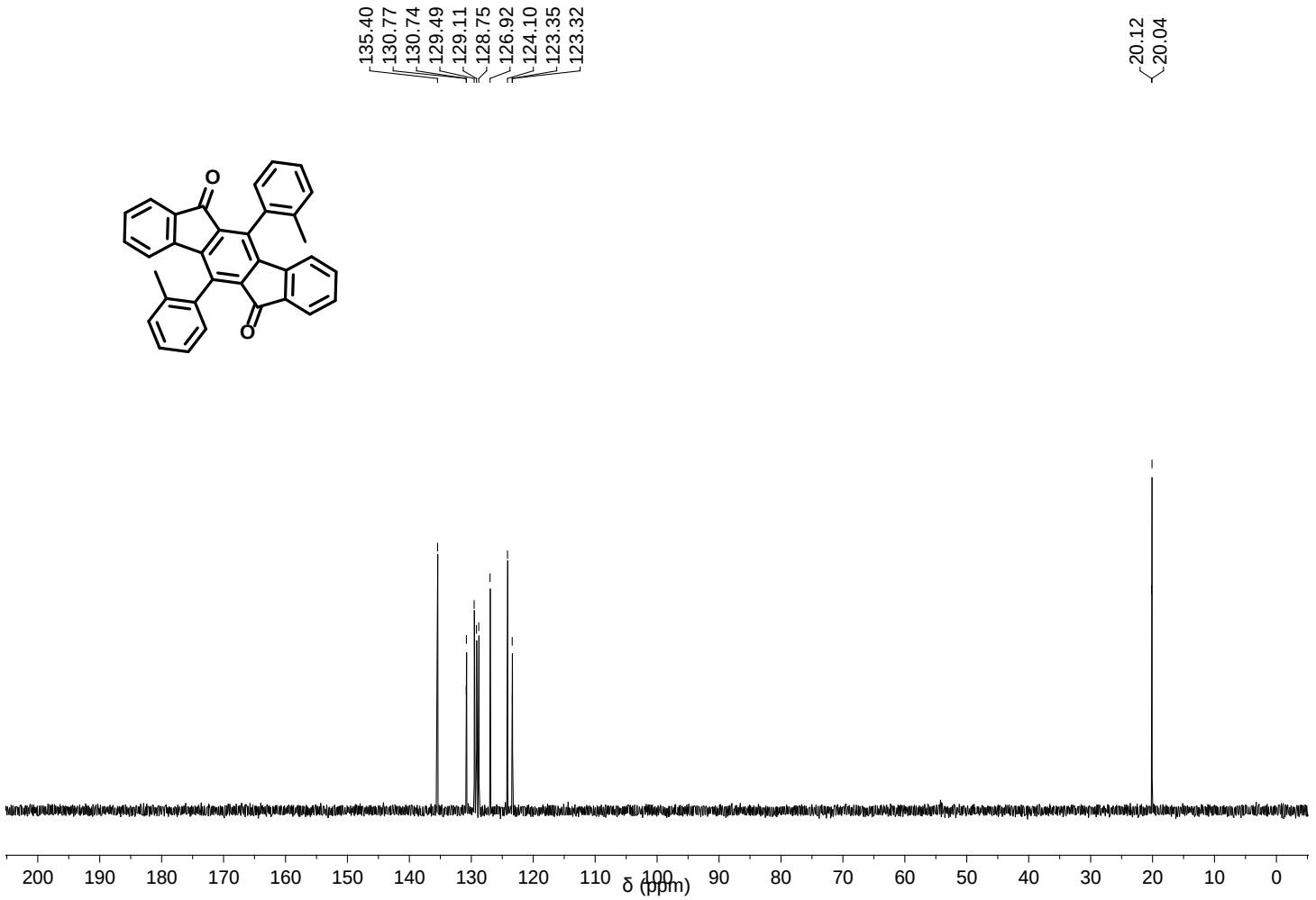

Figure S47: ^{13}C-DEPT135-NMR spectrum of **S6** dissolved in dichloromethane-d_2, 150 MHz, 296 K.

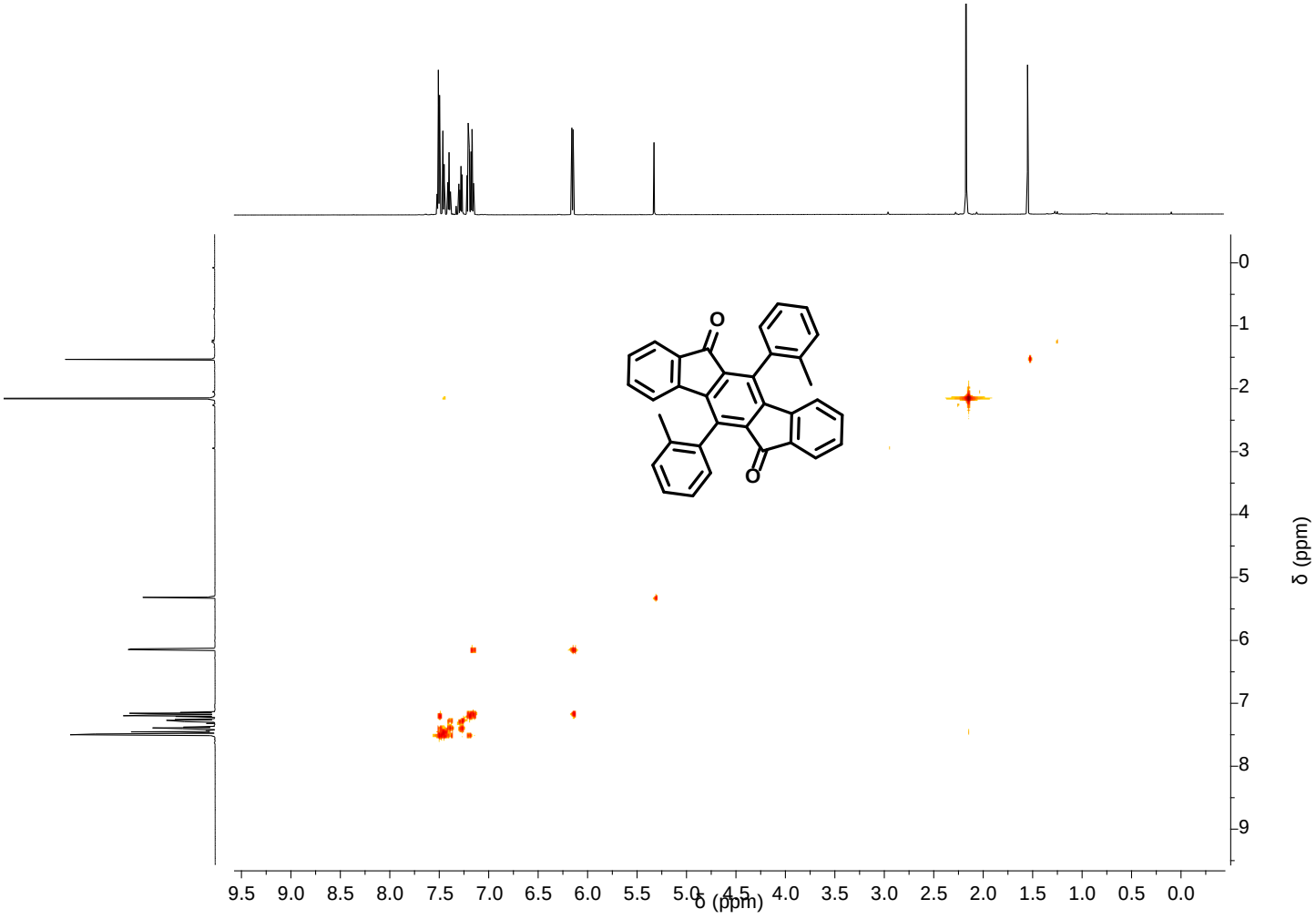

Figure S48: $^{1}H/^{1}H$-COSY-NMR spectrum of **S6** dissolved in dichloromethane-d_2, 600 MHz, 296 K.

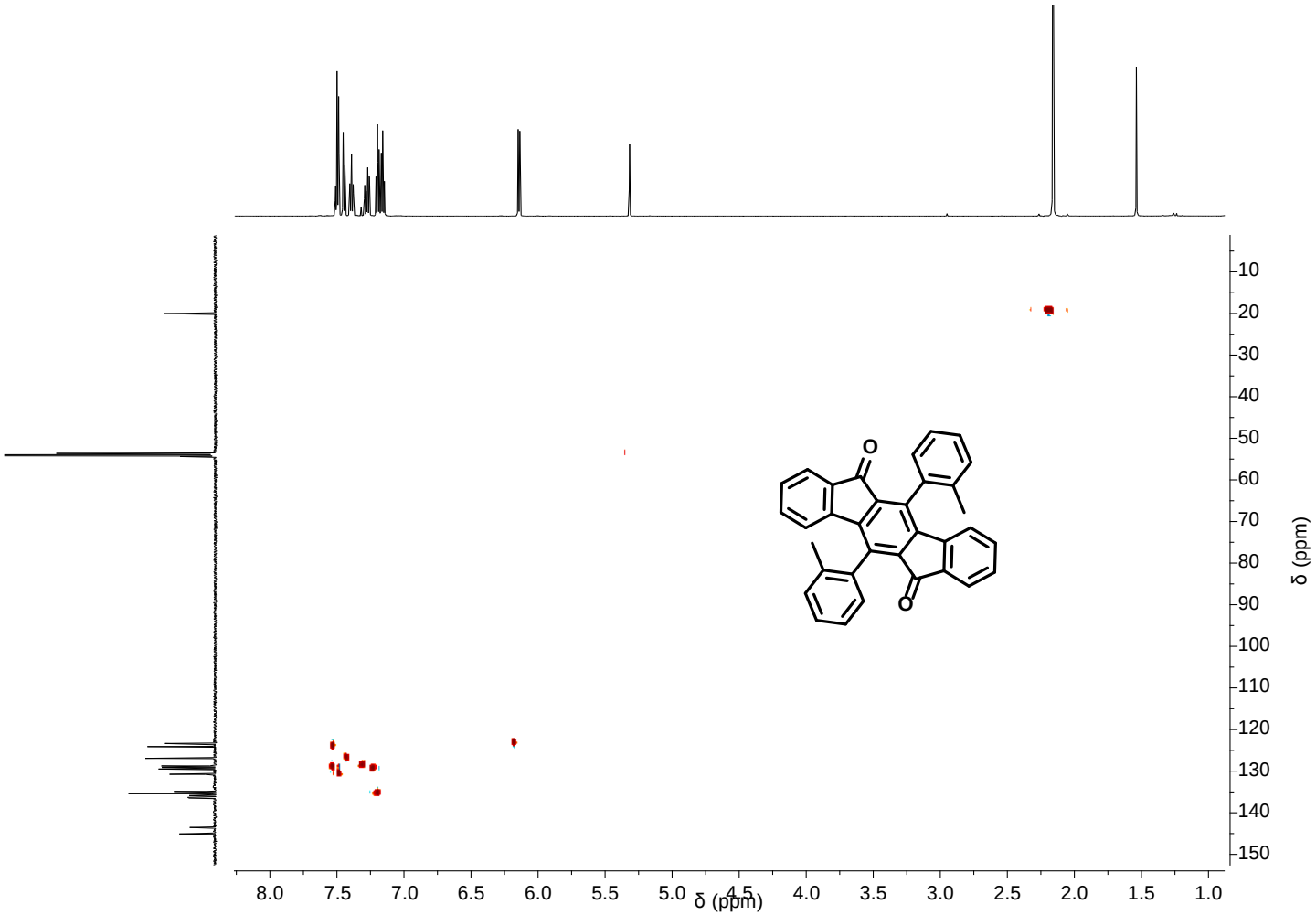

Figure S49: HSQC-NMR spectrum of **S6** dissolved in dichloromethane-d_2, 150 MHz, 296 K.

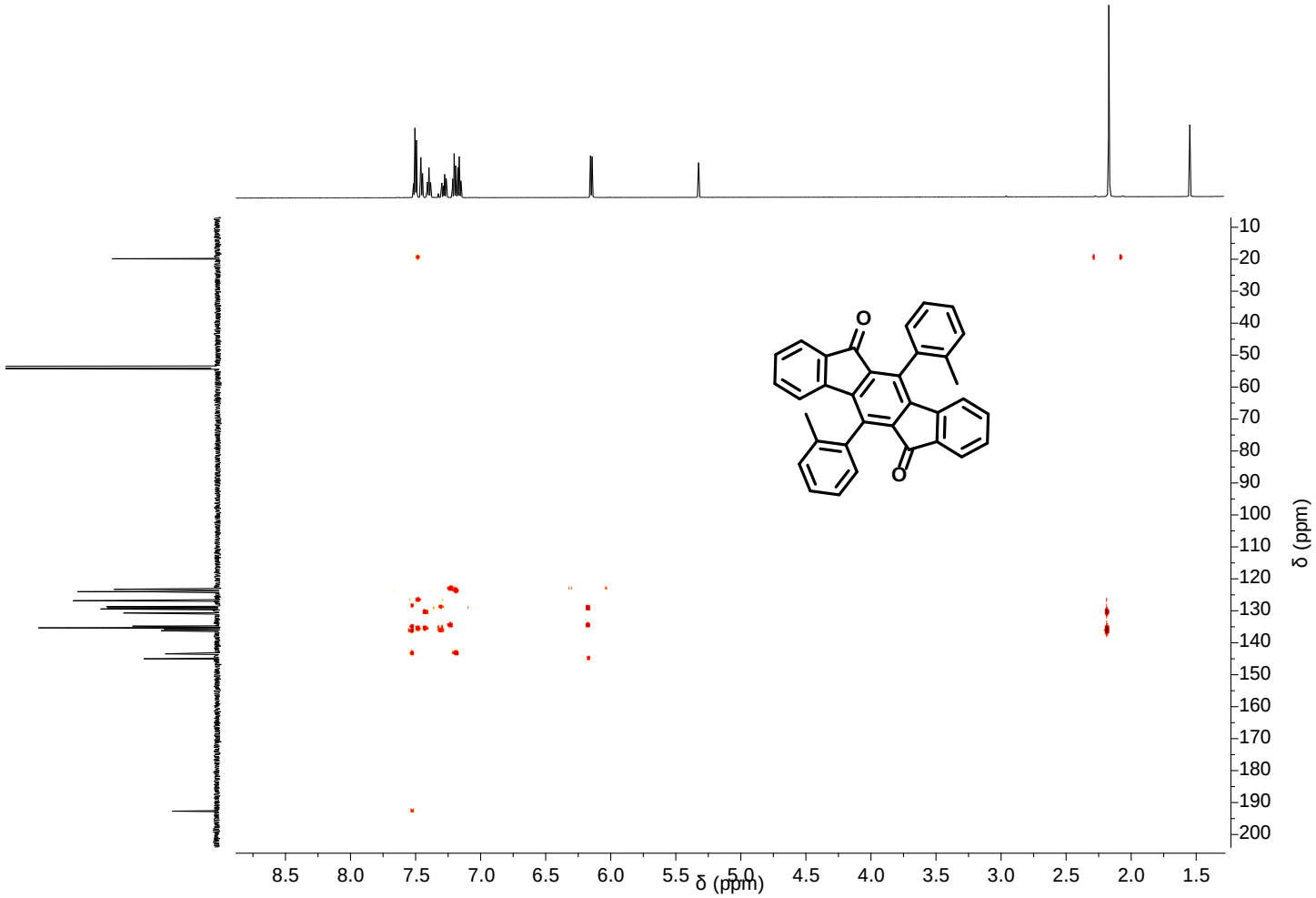

Figure S50: HMBC-NMR spectrum of **S6** dissolved in dichloromethane-d_2, 150 MHz, 296 K.

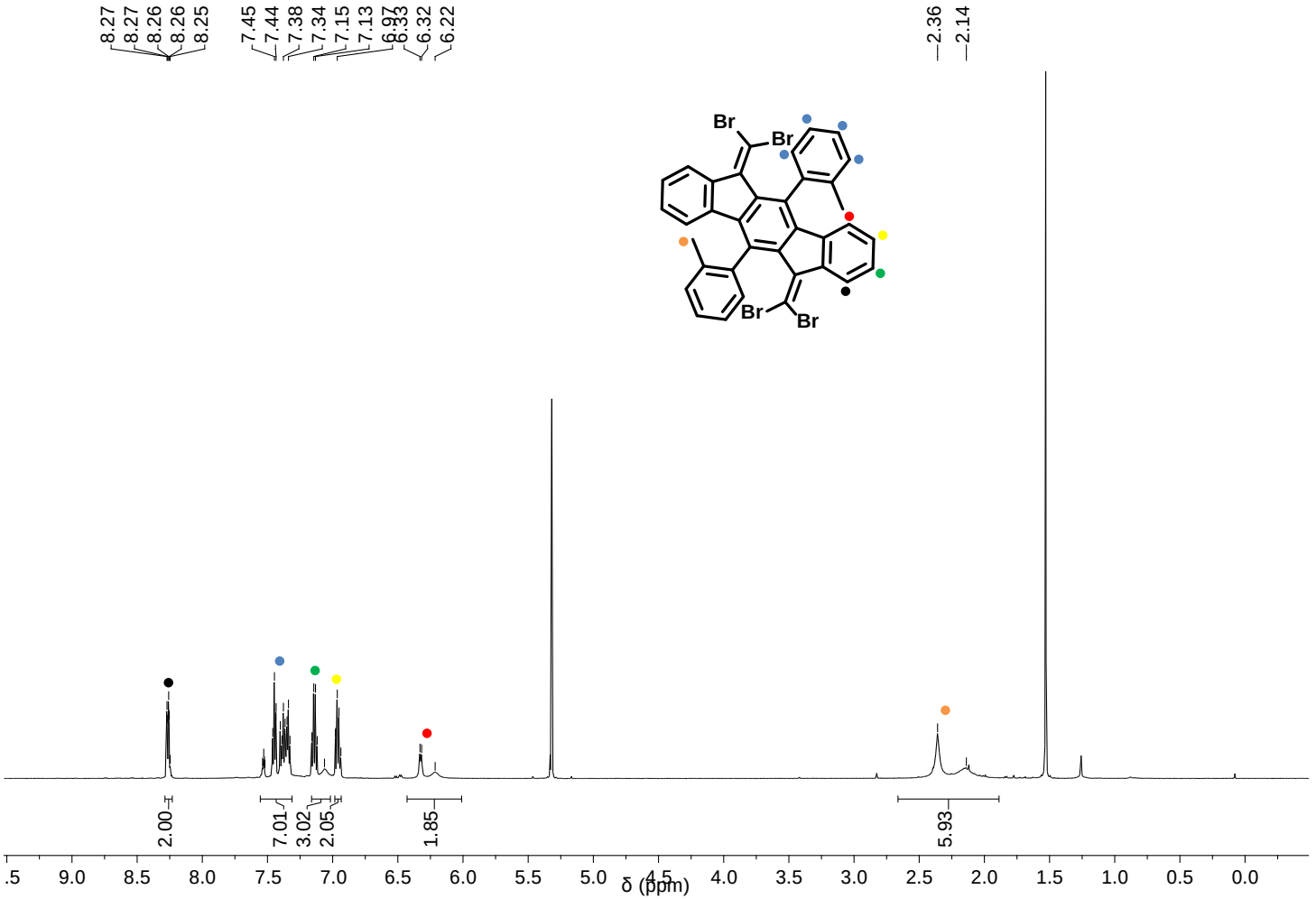

Figure S51: ^{1}H-NMR spectrum of **S7** dissolved in dichloromethane-d_2, 600 MHz, 296 K.

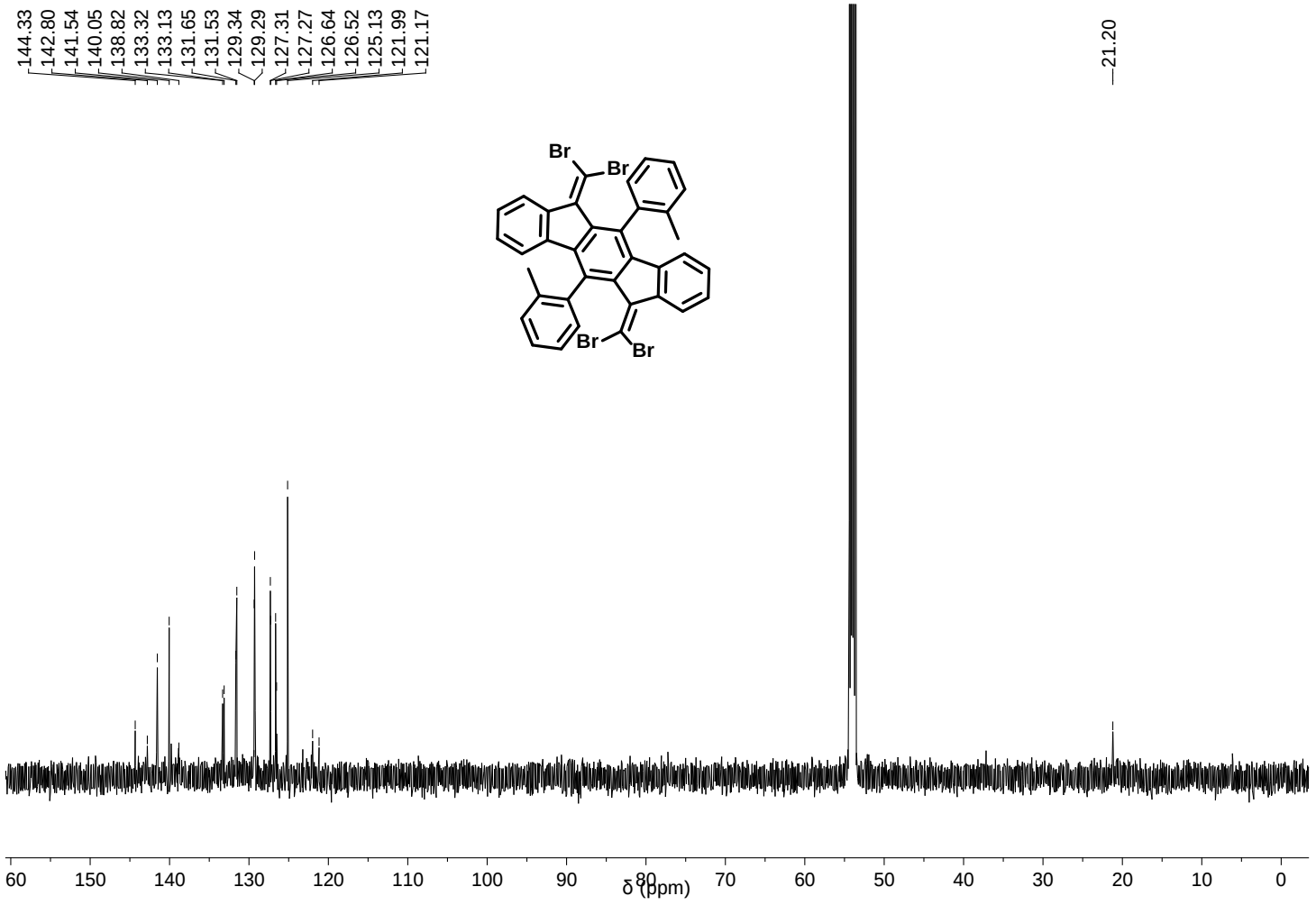

Figure S52: ^{13}C-NMR spectrum of **S7** dissolved in dichloromethane-d_2, 150 MHz, 296 K.

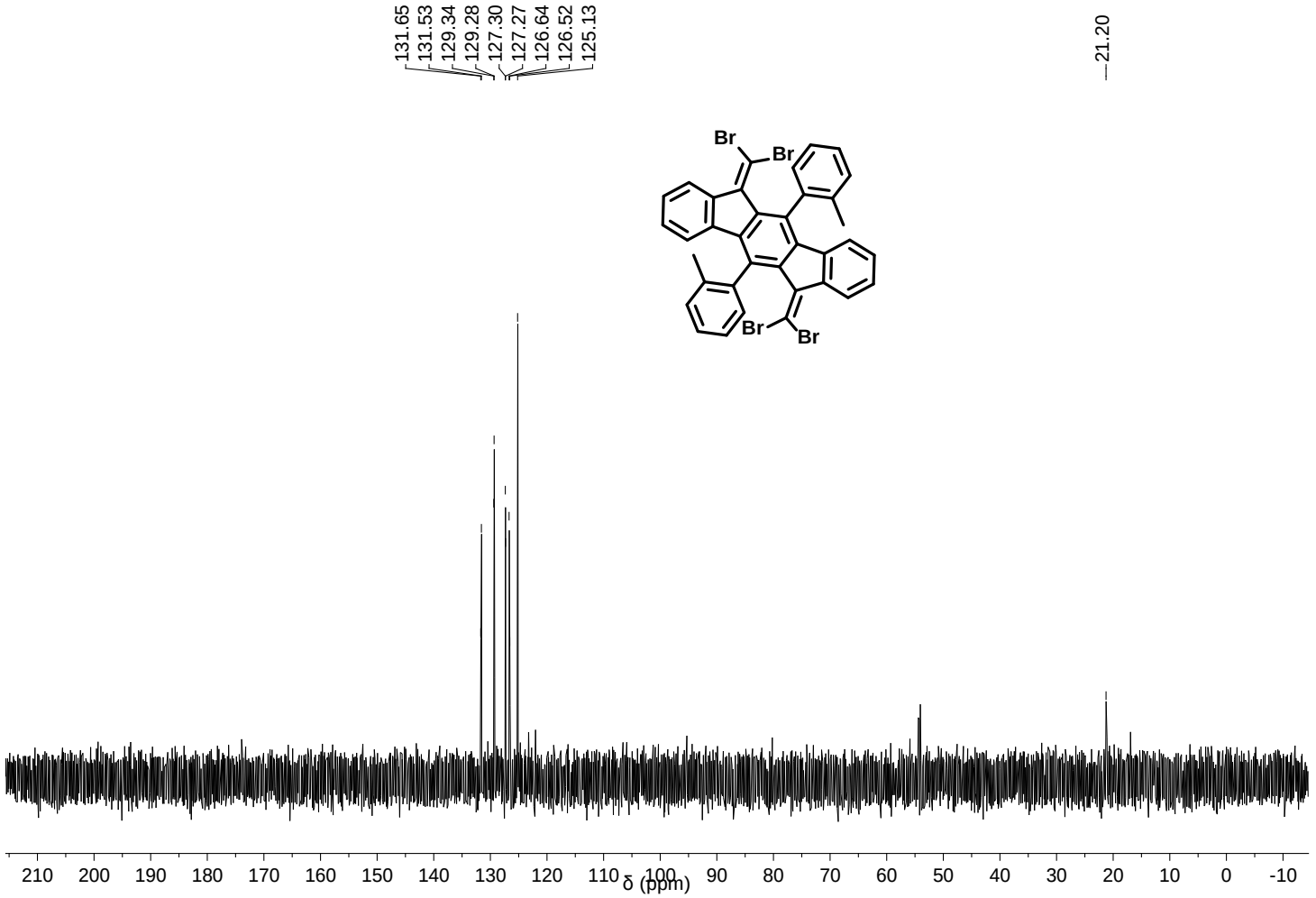

Figure S53: ^{13}C-DEPT135-NMR spectrum of **S7** dissolved in dichloromethane-d_2, 150 MHz, 296 K.

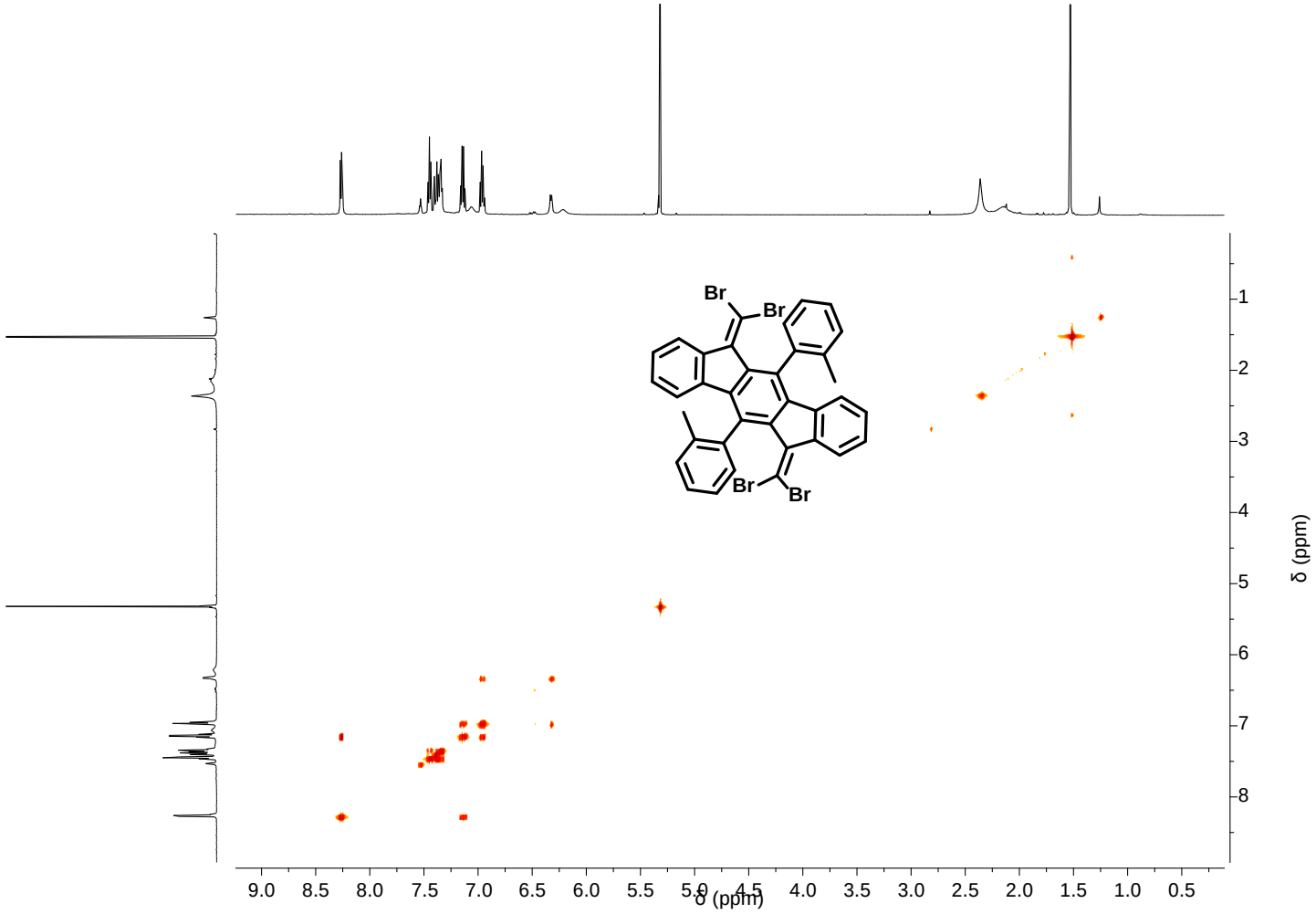

Figure S54: $^{1}H/^{1}H$-COSY-NMR spectrum of **S7** dissolved in dichloromethane-d_2, 600 MHz, 296 K.

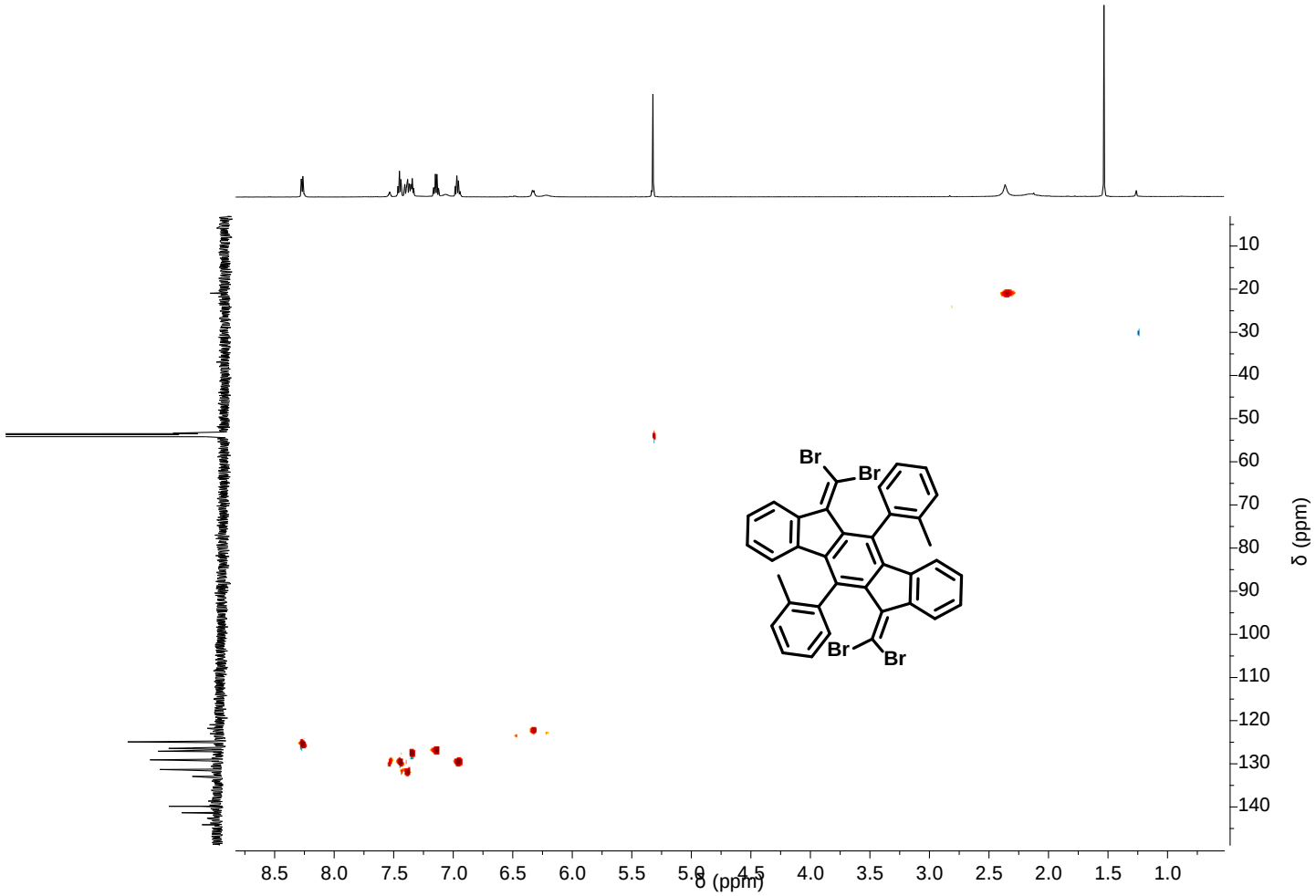

Figure S55: HSQC-NMR spectrum of **S7** dissolved in dichloromethane-d_2, 150 MHz, 296 K.

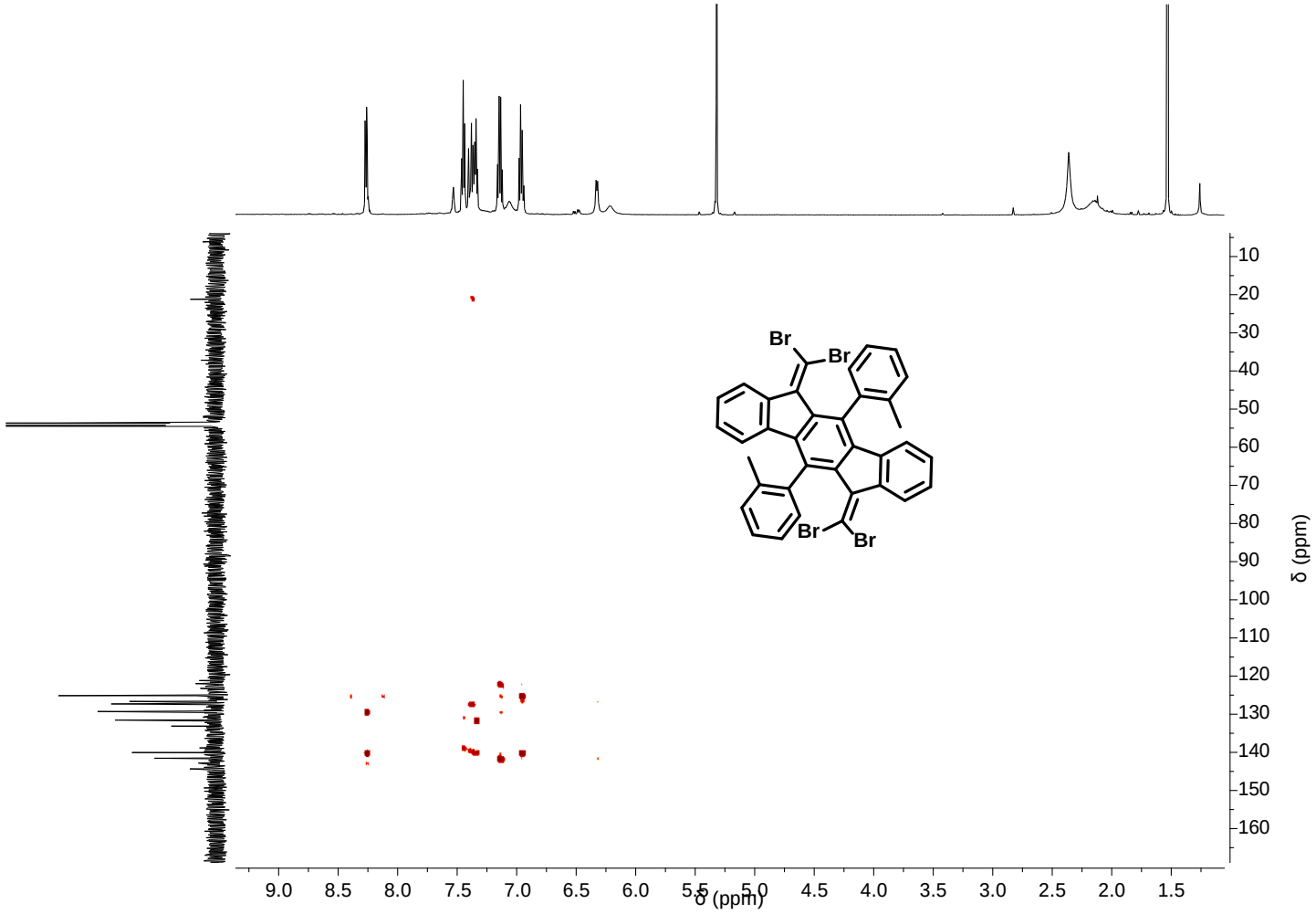

Figure S56: HMBC-NMR spectrum of **S7** dissolved in dichloromethane-d_2, 150 MHz, 296 K.

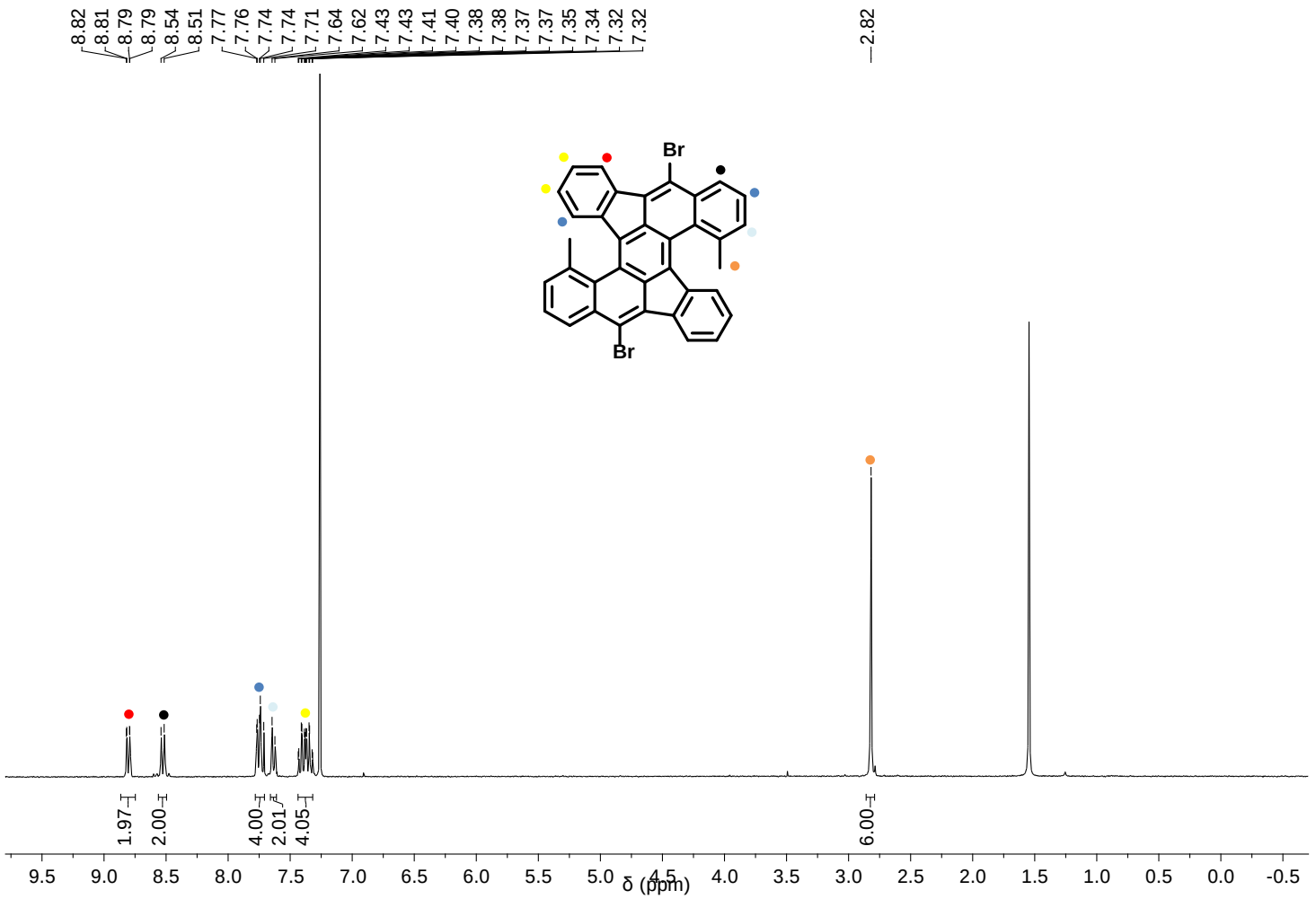

Figure S57: ^{1}H-NMR spectrum of **S8** dissolved in chloroform-d$_1$, 300 MHz, 296 K.

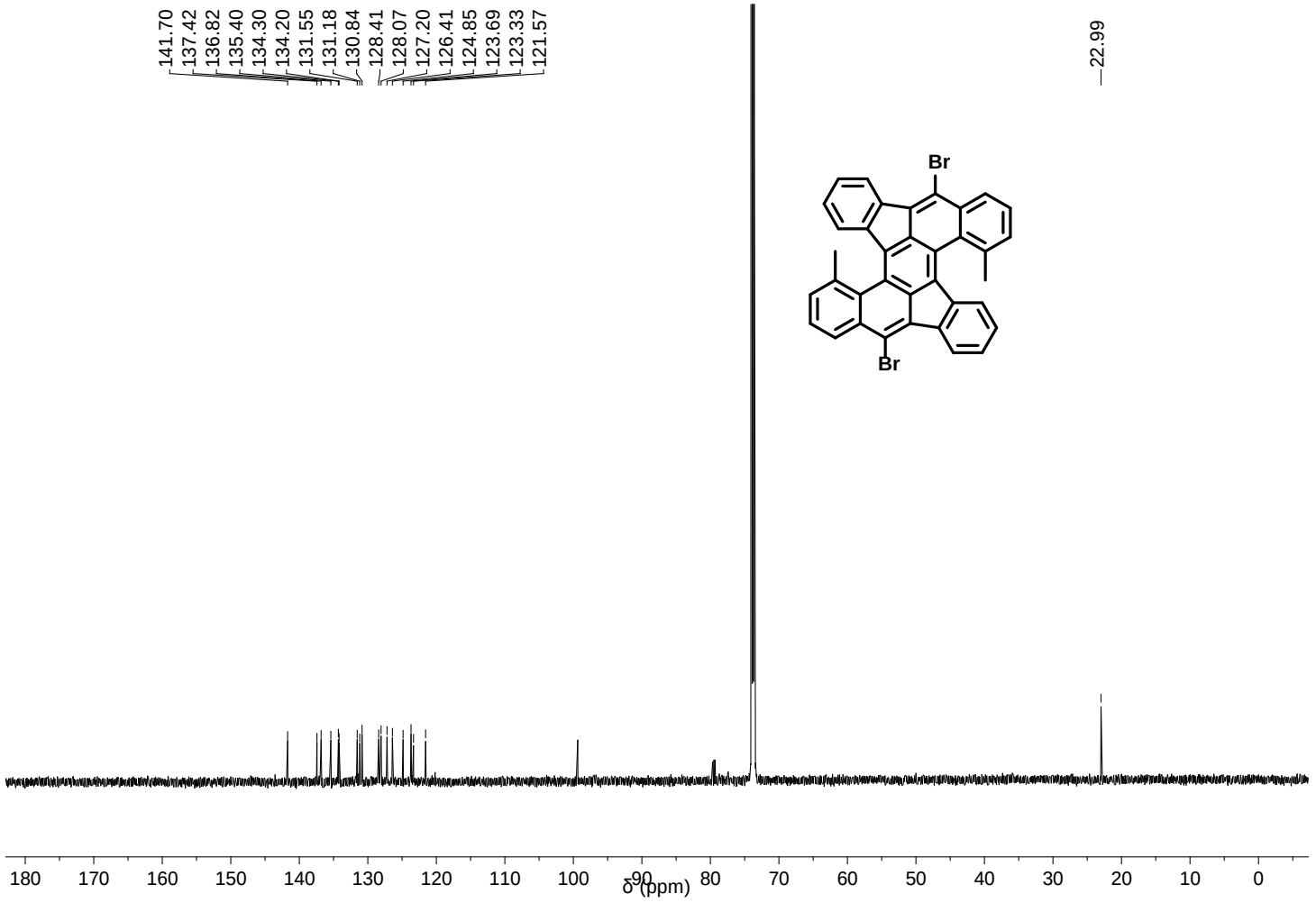

Figure S58: ^{13}C-NMR spectrum of **S8** dissolved in tetrachloroethane-d_2, 150 MHz, 296 K.

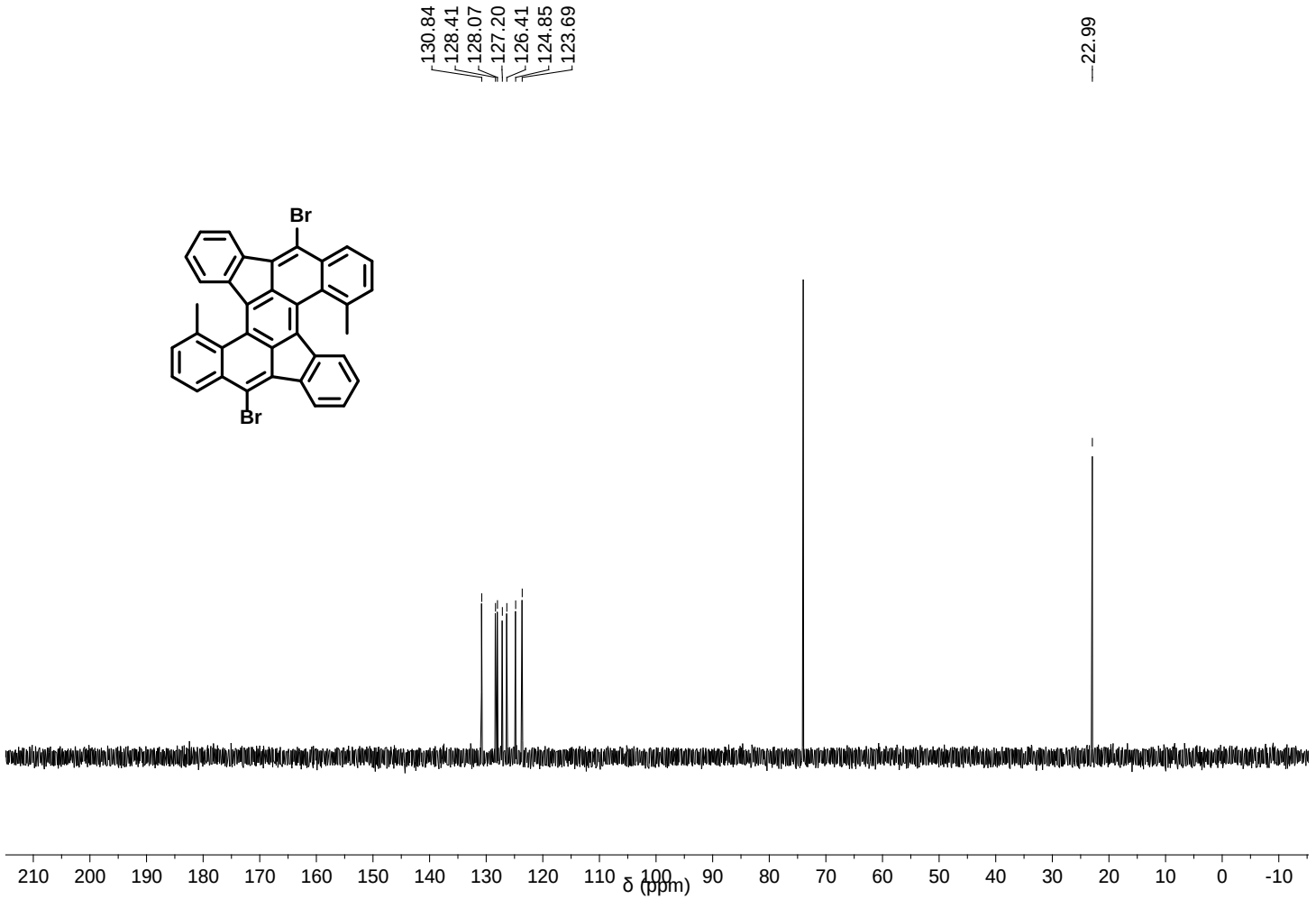

Figure S59: ^{13}C-DEPT135-NMR spectrum of **S8** dissolved in tetrachloroethane-d_2, 150 MHz, 296 K.

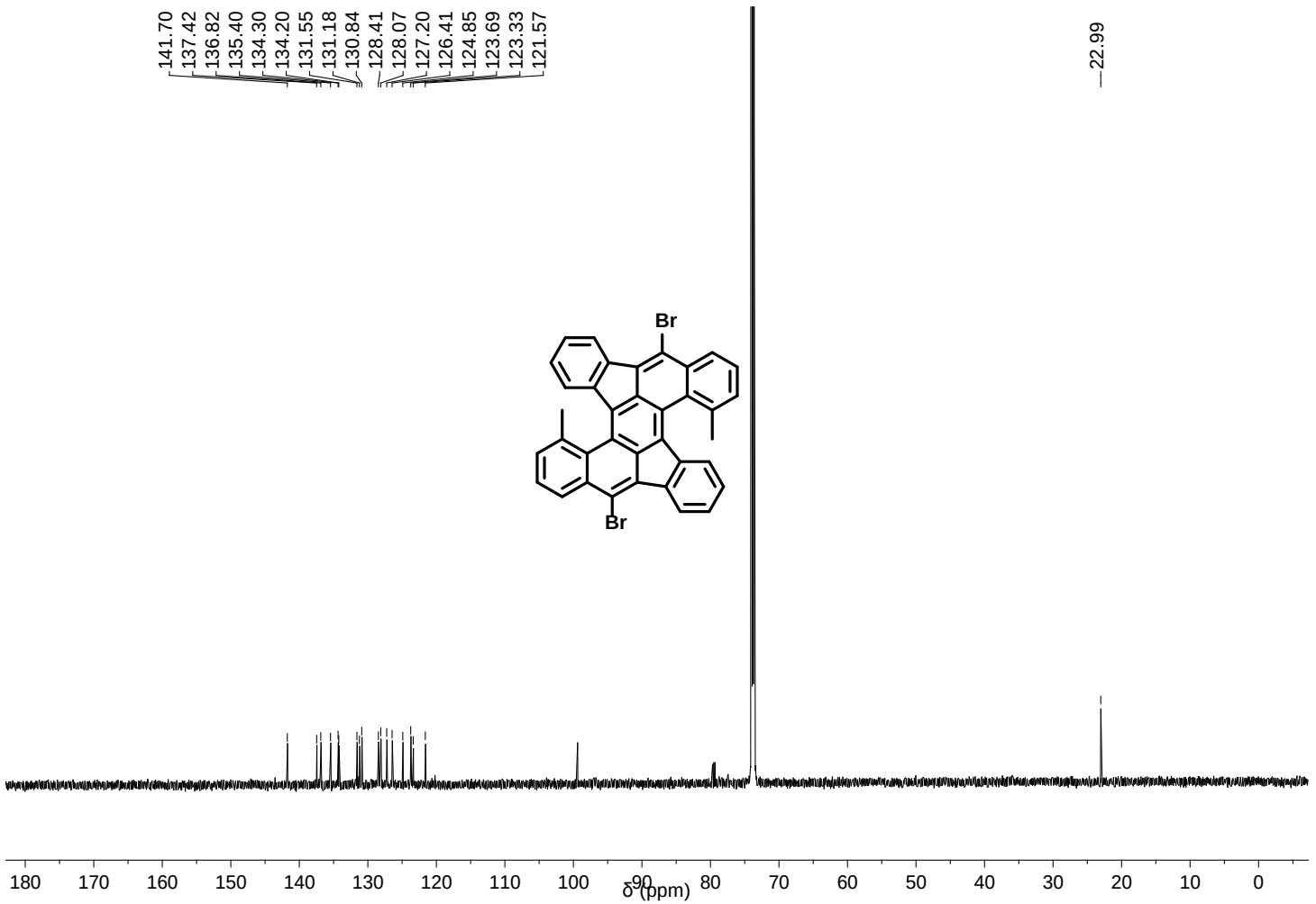

Figure S60: $^{1}H/^{1}H$-COSY-NMR spectrum of **S8** dissolved in tetrachloroethane-d_2, 600 MHz, 296 K.

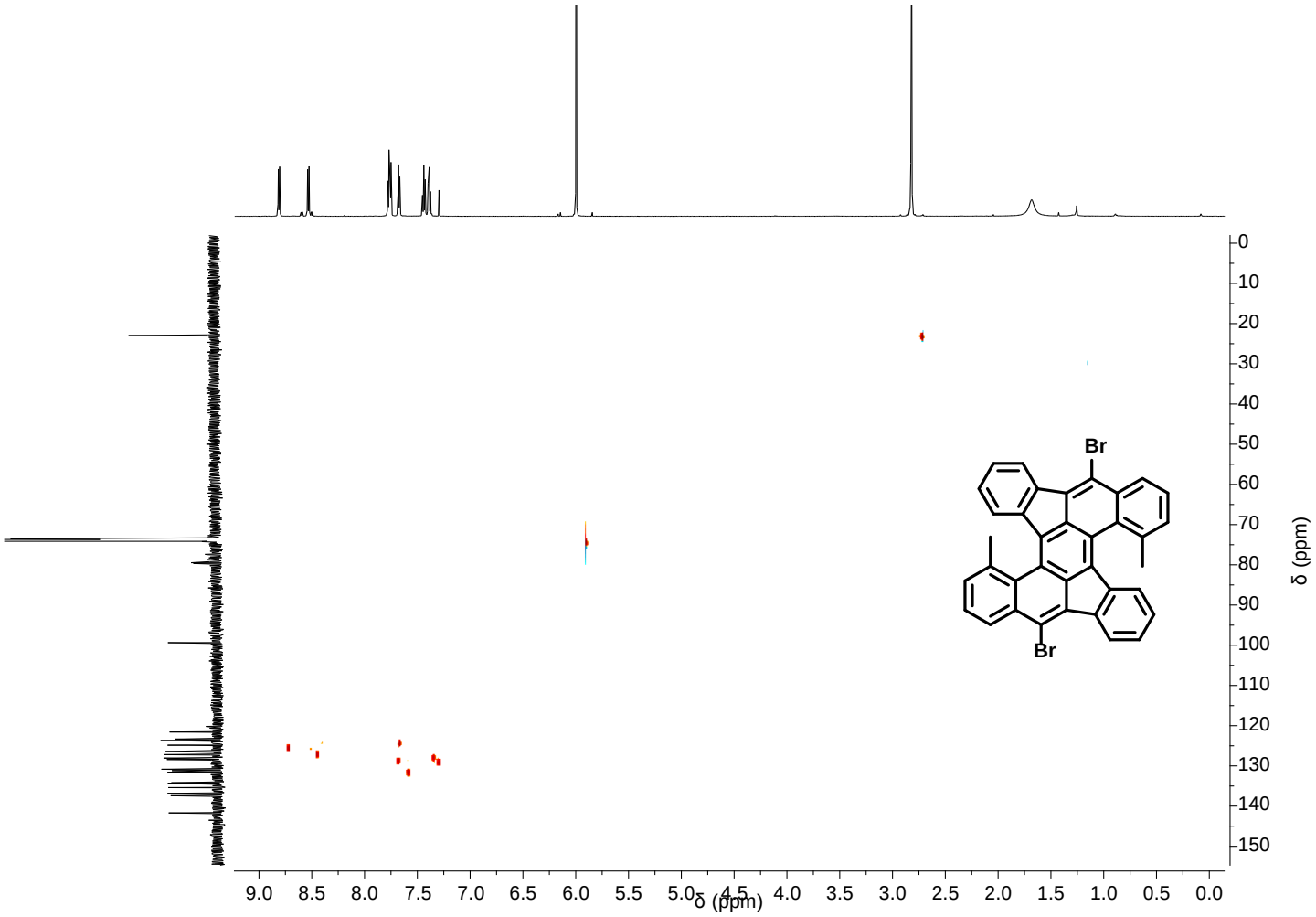

Figure S61: HSQC-NMR spectrum of **S8** dissolved in tetrachloroethane-d_2, 150 MHz, 296 K.

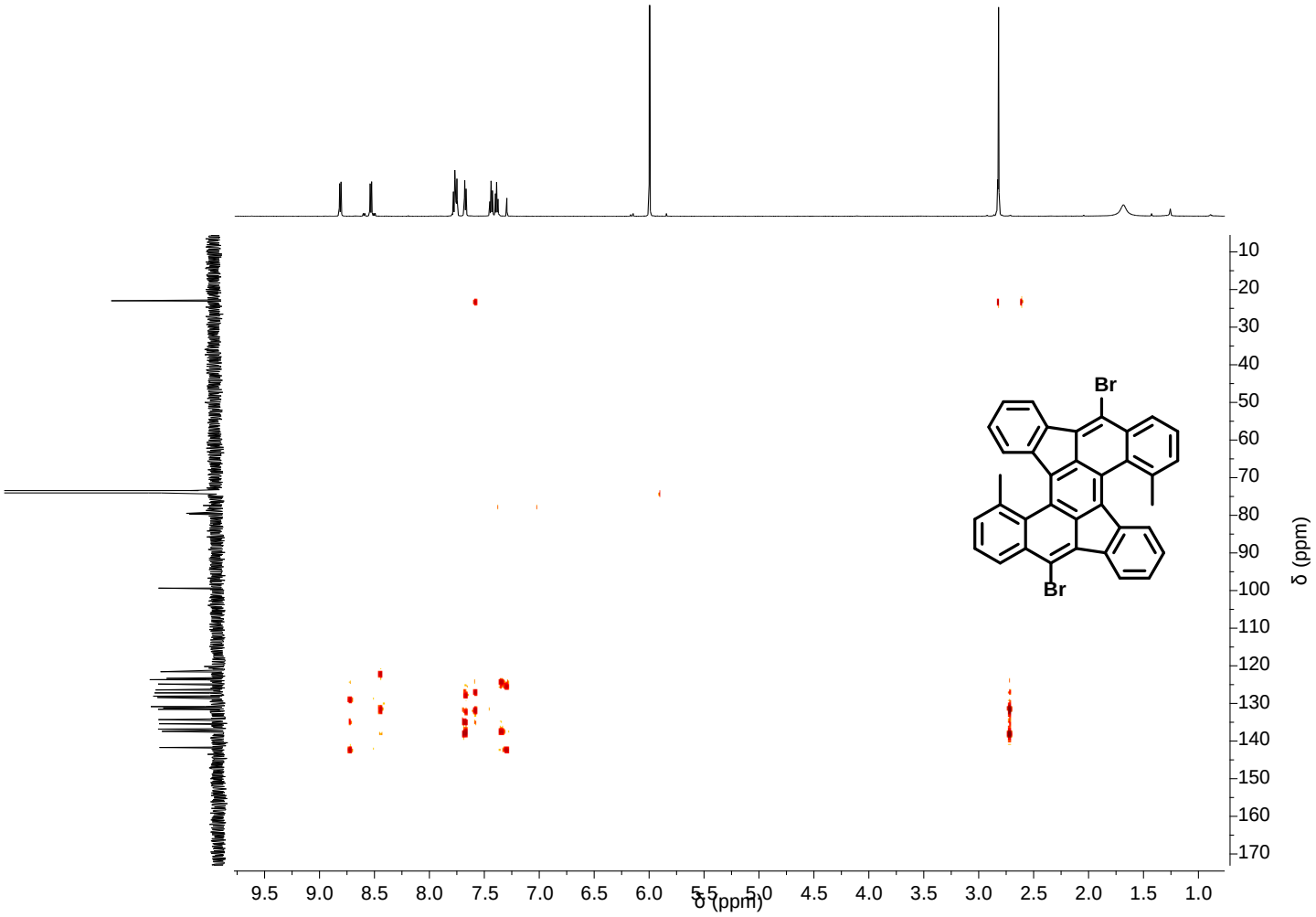

Figure S62: HMBC-NMR spectrum of **S8** dissolved in tetrachloroethane-d_2, 150 MHz, 296 K.

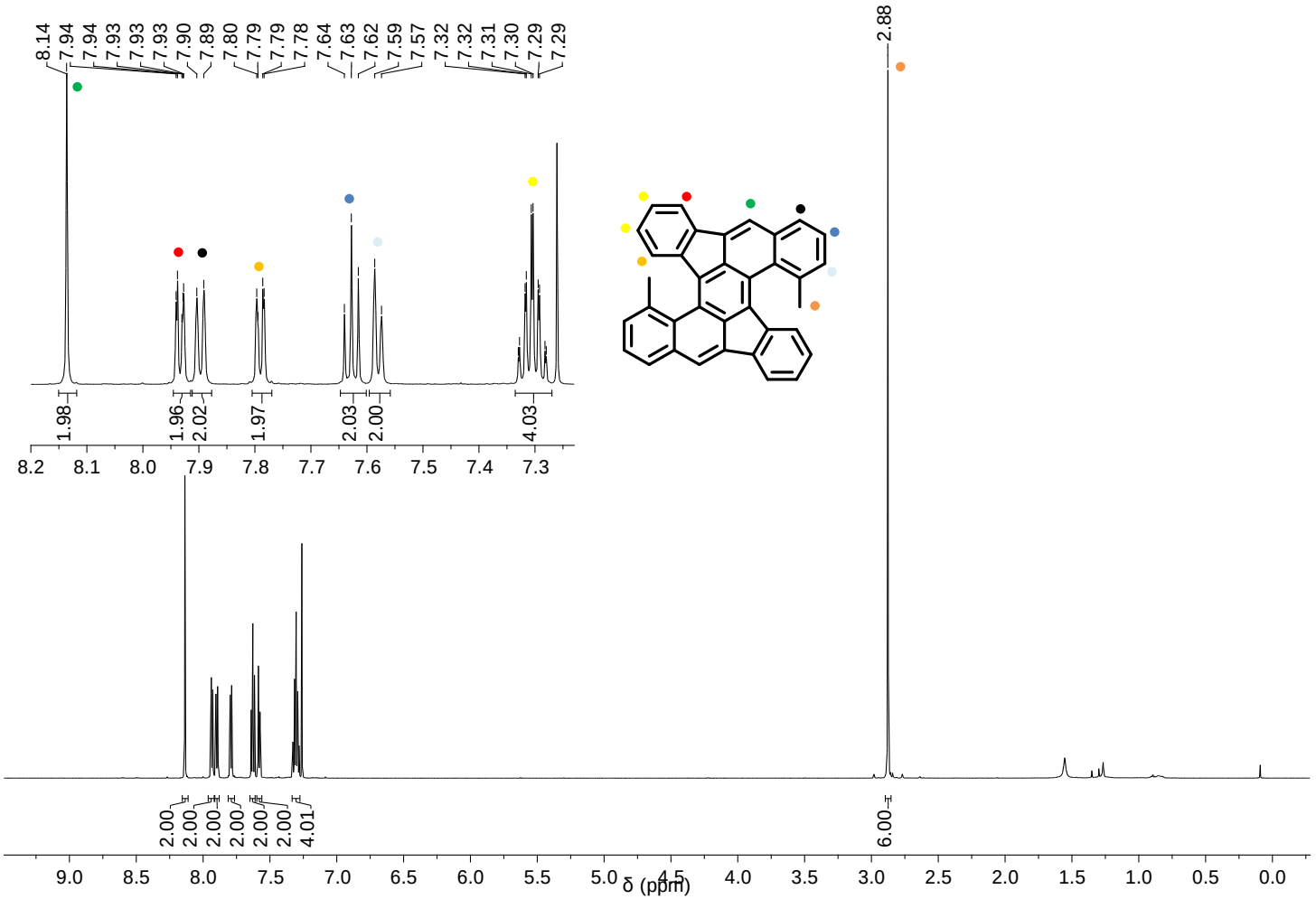

Figure S63: ^{1}H-NMR spectrum of **4** dissolved in chloroform-d_1, 600 MHz, 296 K.

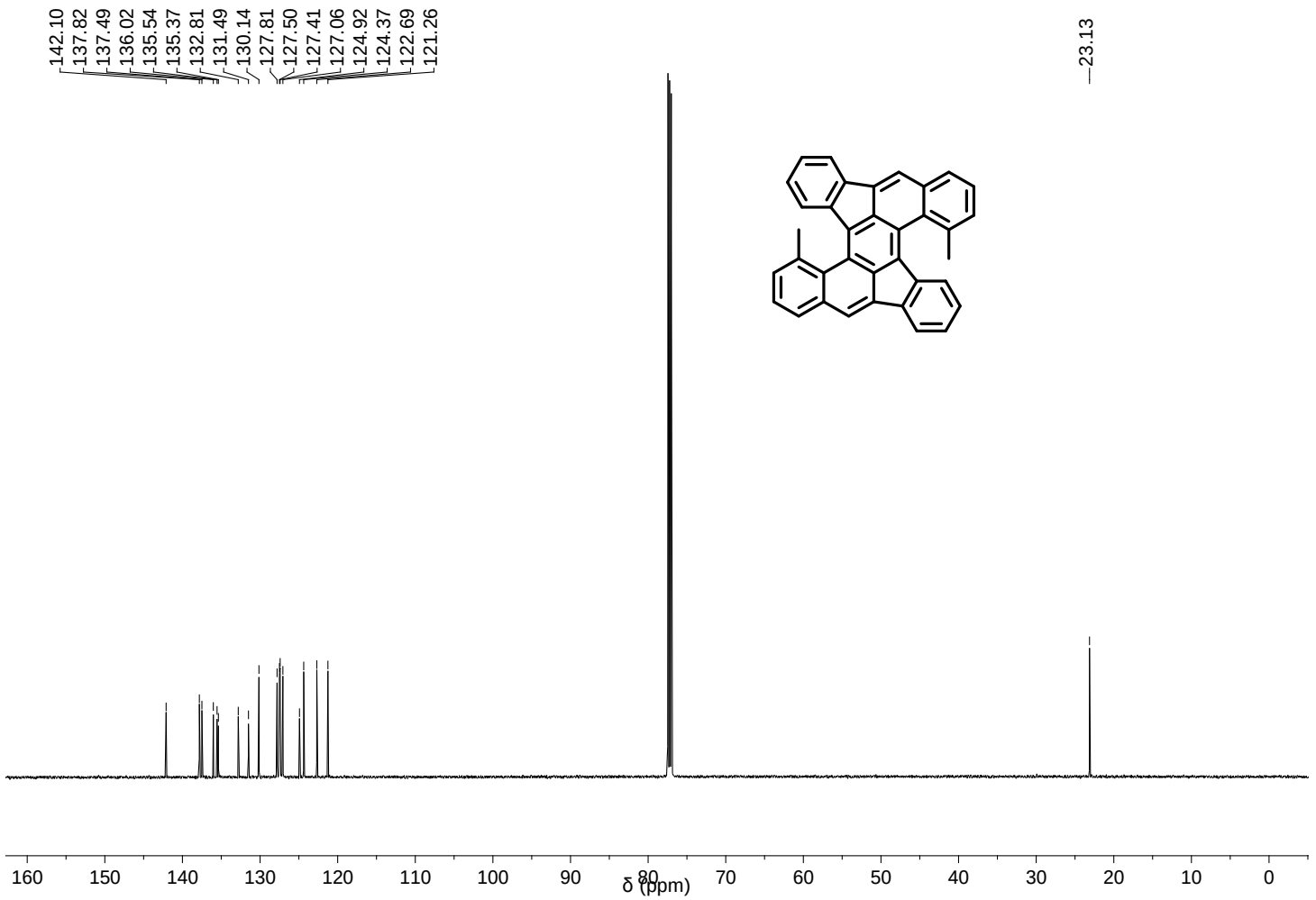

Figure S64: ^{13}C-NMR spectrum of **4** dissolved in chloroform-d_1, 150 MHz, 296 K.

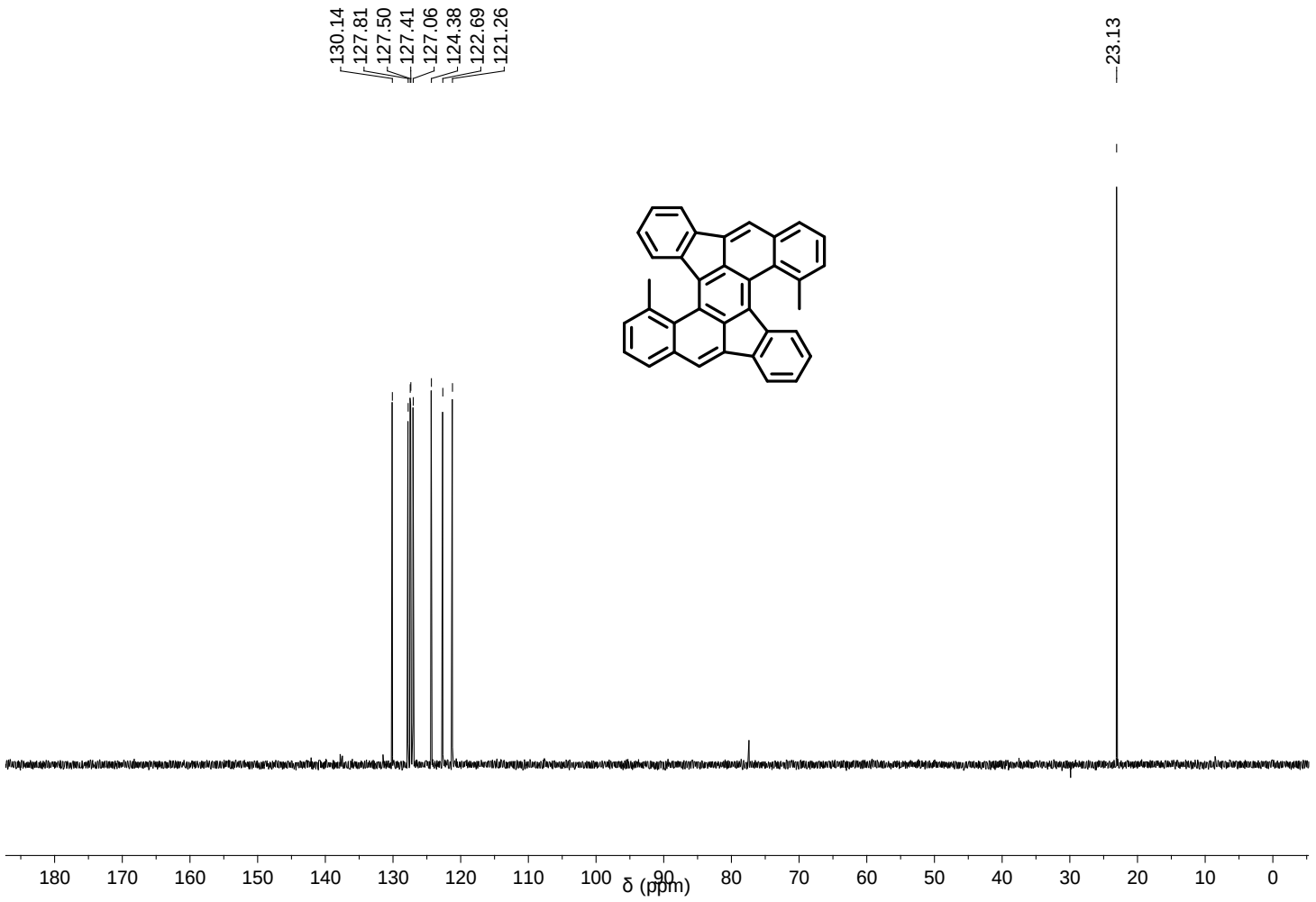

Figure S65: ^{13}C-DEPT135-NMR spectrum of **4** dissolved in chloroform-d_1, 150 MHz, 296 K.

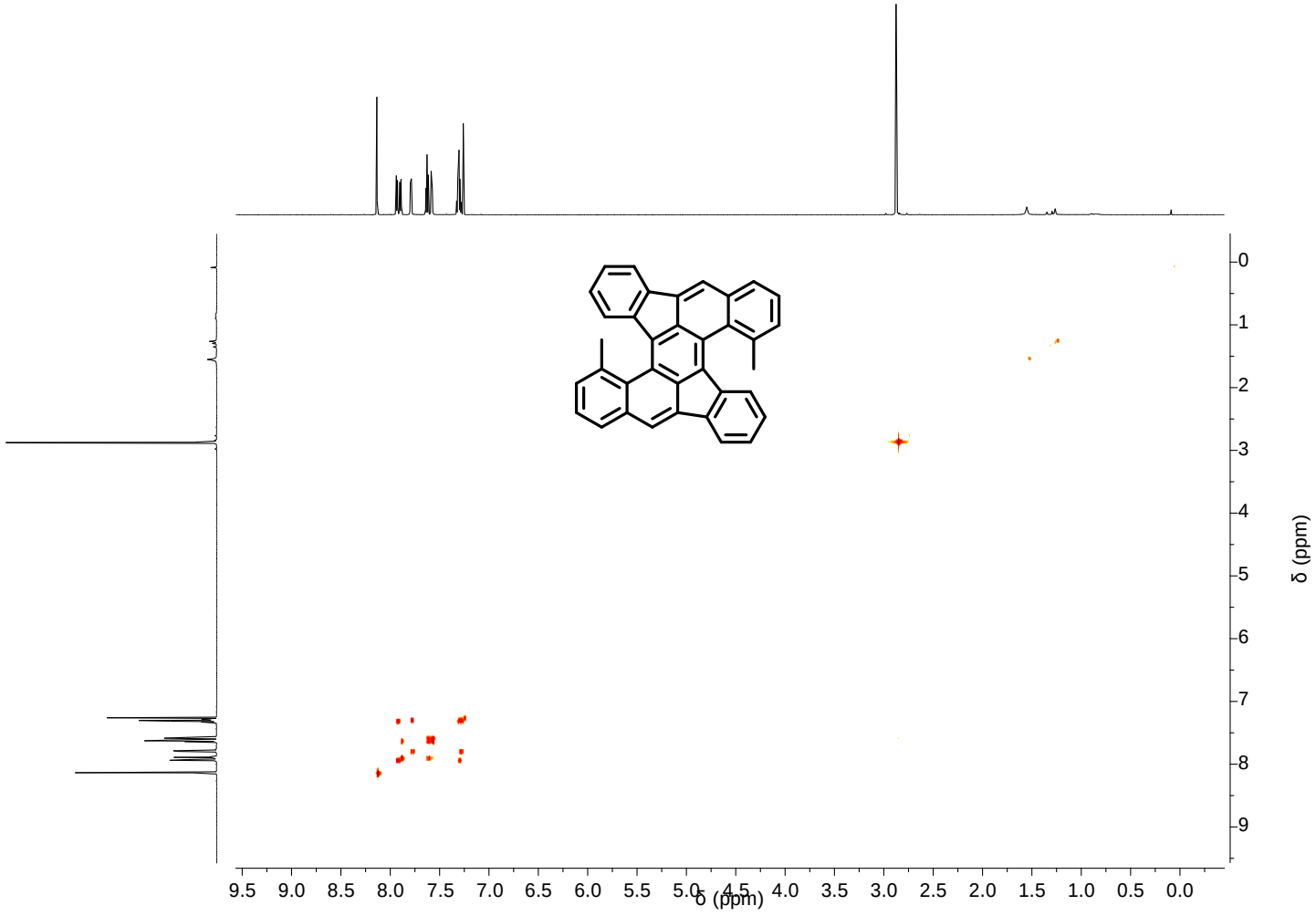

Figure S66: $^{1}H/^{1}H$-COSY-NMR spectrum of **4** dissolved in tetrachlorethane-d_2, 600 MHz, 296 K.

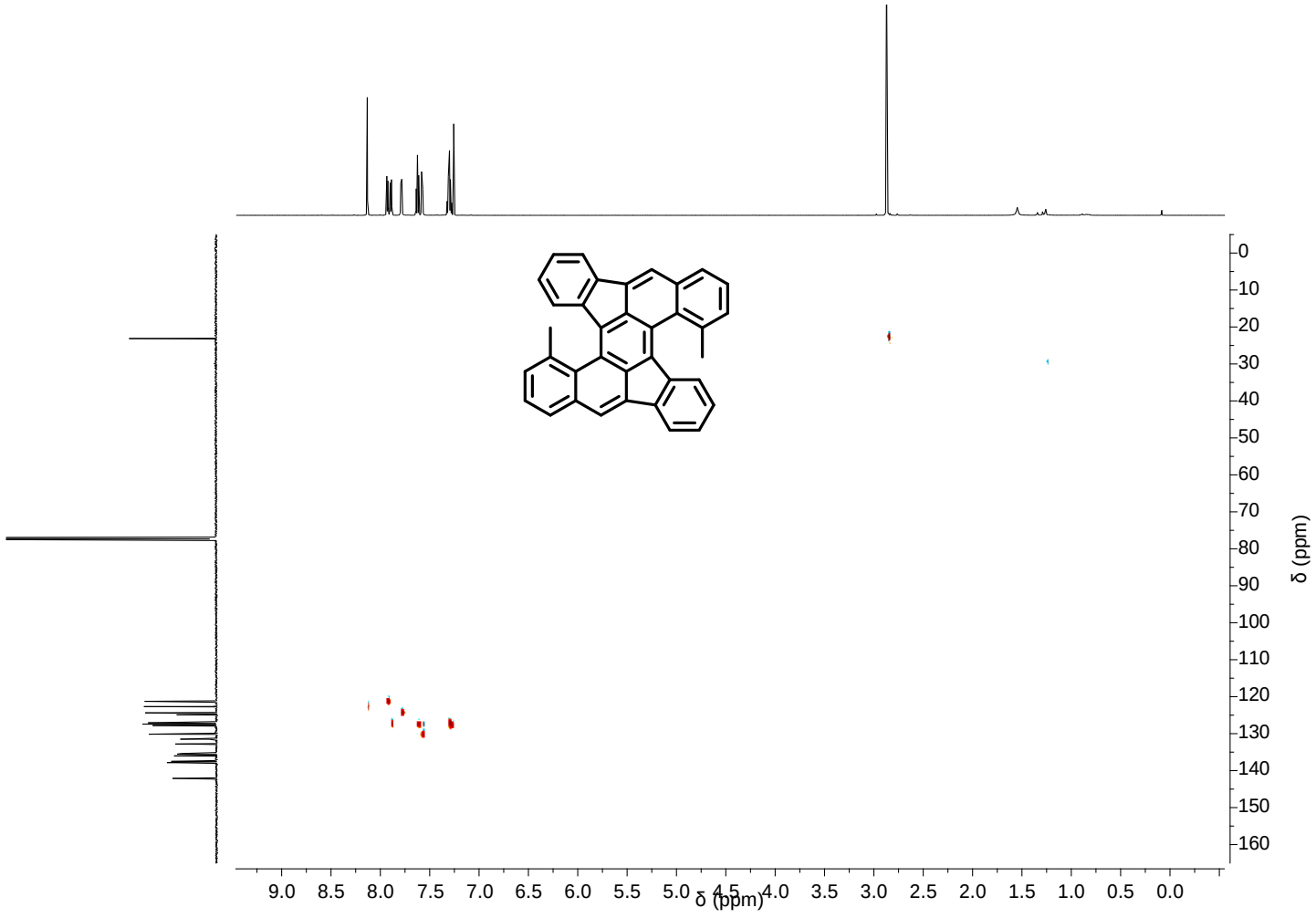

Figure S67: HSQC-NMR spectrum of **4** dissolved in chloroform-d_1, 150 MHz, 296 K.

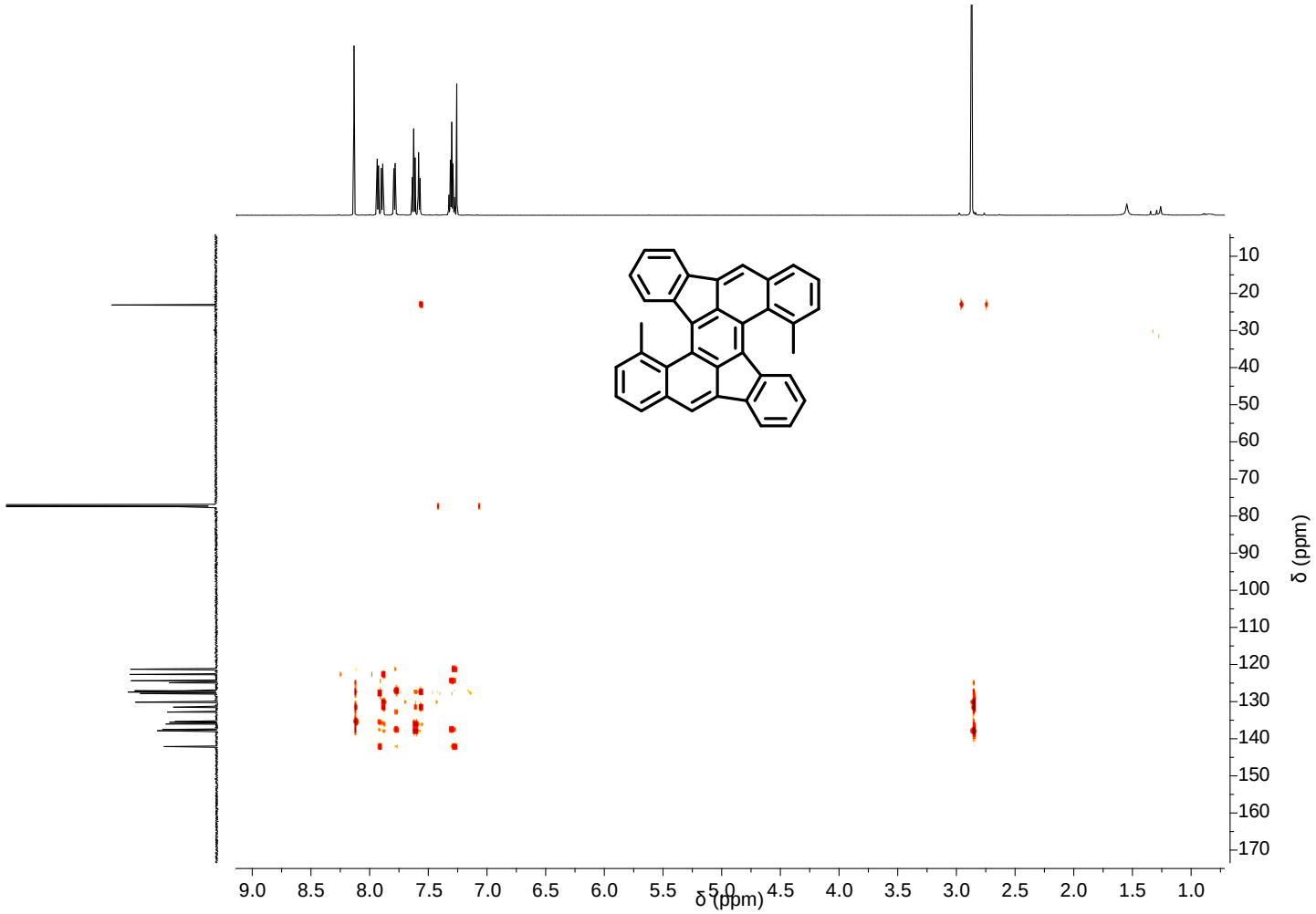

Figure S68: HMBC-NMR spectrum of **4** dissolved in chloroform-d_1, 150 MHz, 296 K.

18. Supplementary References

(1) van Scheppingen, W.; Dorrestijn, E.; Arends, I.; Mulder, P.; Korth, H.-G. Carbon−Oxygen Bond Strength in Diphenyl Ether and Phenyl Vinyl Ether: An Experimental and Computational Study. *J. Phys. Chem. A* **1997**, *101*, 5404–5411.

(2) Liu, J.; Ravat, P.; Wagner, M.; Baumgarten, M.; Feng, X.; Müllen, K. Tetrabenzo[a,f,j,o]Perylene: A Polycyclic Aromatic Hydrocarbon with An Open-Shell Singlet Biradical Ground State. *Angew. Chem. Int. Ed.* **2015**, *54*, 12442–12446.

(3) Ide, T.; Sakamoto, S.; Takeuchi, D.; Osakada, K.; Machida, S. Strained and Unstrained Macrocycles Composed of Carbazole and Butadiyne Units: Electronic State and Optical Properties. *J. Org. Chem.* **2012**, *77*, 4837–4841.

(4) Rose, B. D.; Santa Maria, P. J.; Fix, A. G.; Vonnegut, C. L.; Zakharov, L. N.; Parkin, S. R.; Haley, M. M. Scalable Synthesis of 5,11-Diethynylated Indeno[1,2-b]Fluorene-6,12-Diones and Exploration of Their Solid State Packing. *Beilstein J. Org. Chem.* **2014**, *10*, 2122–2130.